Two-dimensional electron gas in functional oxide interfaces

Caviglia, Andrea

UNIVERSITÉ DE GENÈVE
Dèpartement de physique de la matière condensée

FACULTÉ DES SCIENCES
Professeur J.-M. Triscone

Two-dimensional electron gas in functional oxide interfaces

THÈSE

présenté à la Faculté des Sciences de l'Université de Genève pour obtenir le grade de docteur ès Sciences, mention physique

par

Andrea Caviglia
de
Zena (Italie)

Thèse n° 4261

GENÈVE
Atelier de reproduction de la Section de Physique
2010

Contents

1 Functional interfaces **5**
- 1.1 Functional oxides . . . 5
  - 1.1.1 $SrTiO_3$ . . . 6
- 1.2 The conducting $LaAlO_3/SrTiO_3$ interface . . . 11
  - 1.2.1 Doping mechanisms . . . 11
  - 1.2.2 Electronic structure . . . 14
  - 1.2.3 Confinement . . . 15
- 1.3 Fabrication of $LaAlO_3/SrTiO_3$ heterostructures . . . 18
- 1.4 Influence of the growth conditions on the $LaAlO_3/SrTiO_3$ interface electronic properties . . . 21
  - 1.4.1 Thickness of the $LaAlO_3$ layer . . . 21
  - 1.4.2 Oxygen pressure and annealing procedure . . . 22
  - 1.4.3 Temperature . . . 25

2 Electric field control of interfacial superconductivity **27**
- 2.1 Quantum phase transitions . . . 27
  - 2.1.1 Central ideas on phase transitions . . . 27
  - 2.1.2 Quantum criticality . . . 28
  - 2.1.3 The role of quantum statistical mechanics . . . 29
- 2.2 The superconductor-insulator transition . . . 30
  - 2.2.1 The Berezinskii-Kosterlitz-Thouless transition . . . 30
  - 2.2.2 The fermionic model . . . 32
  - 2.2.3 The dirty boson model . . . 33
- 2.3 Electrostatic tuning of superconductivity in $LaAlO_3/SrTiO_3$ interfaces 36
  - 2.3.1 Two-dimensional superconductivity . . . 36
  - 2.3.2 Field effect experiments . . . 40

3 Localisation and spin-orbit interaction **49**
- 3.1 Measuring disorder . . . 49
- 3.2 Conductivity in the quantum many-body formalism . . . 50
  - 3.2.1 Kubo formula . . . 50
  - 3.2.2 Weak localisation . . . 53
  - 3.2.3 Experimental probes . . . 55
- 3.3 Spin-orbit interaction . . . 55
  - 3.3.1 Rashba hamiltonian . . . 56

3.4 Weak antilocalisation 59
3.5 Strong localisation and the scaling theory 60
3.6 Magnetotransport across the $LaAlO_3/SrTiO_3$ interface phase diagram 64

4 Two-dimensional quantum oscillations 73
4.1 Onsager relation 73
4.2 Shubnikov-de Haas oscillations in $LaAlO_3/SrTiO_3$ interfaces 74

5 Nanostructuring oxide interfaces 81
5.1 Photolithography 81
5.2 Electron-beam lithography 82
5.3 Field-effect devices 84

Résumé

Durant les dernières décennies, la possibilité de modifier les propriétés électroniques d'un matériau de façon contrôlée a créé une véritable révolution dans les technologies de l'information et de la communication. Le meilleur exemple en est le transistor à effet de champ, un dispositif étant capable de conduire un courant électrique ou de le bloquer à la simple application d'un champ électrique externe.

Cette fonctionnalité fut rendue possible par la création d'une interface entre deux matériaux, d'une part un isolant et d'autre part un semi-conducteur. Cette simple construction est en fait l'élément central de nos ordinateurs ou téléphones portables modernes, en effet rien que dans un seul de ces derniers plusieurs centaines de millions de transistors y sont rangés. Le point le plus intéressant est que chaque constituant de l'interface pris séparément n'exhibant pas de comportement électronique particulièrement remarquable, il s'agit bel et bien de l'interface qui crée la fonctionnalité. Dès lors, il est extrêmement intéressant de se poser la question de ce qu'il adviendrait des propriétés d'une structure composée de matériaux "de base" plus complexes (comme par exemple les oxydes de métaux de transition qui peuvent présenter des propriétés supraconductrices, magnétiques, ...); celles-ci pourraient bien être totalement inattendues ! Une communauté scientifique très active explore actuellement les propriétés de ces matériaux artificiels et l'intérêt pour les nouvelles propriétés électroniques trouvées à leurs interfaces se développe rapidement. Le point clé vient de la structure cristalline des oxydes qui pour une structure similaire offrent des propriétés physiques extrêmement variées, ce qui permet de les combiner dans un cristal artificiel, comme des bricks de Lego de couleurs différentes peuvent être assemblés dans une seule structure.

Dans cette thèse nous avons étudié l'interface entre un isolant, $LaAlO_3$, et un semi-conducteur, $SrTiO_3$, où un gaz électronique à été découvert. Cette combinaison de matériaux est parmi les plus intensément étudiées car elle permet d'établir le lien entre le monde des oxydes complexes et les hétérostructures de semi-conducteurs conventionnels basé sur les composés III-V. La majeure partie des échantillons étudiés dans cette thèse a été fabriquée dans notre laboratoire. Nous avons attentivement analysé le rôle des conditions de fabrications dans la détermination des propriétés électroniques de cette interface. Ces travaux ont permis d'optimiser les paramètres de croissance et nous ont permis d'éviter des pièges, tels que la délocalisation des porteurs de charge dans le substrat due à des lacunes d'oxygène.

Puisque le gaz électronique se trouve dans un matériau doté de riches propriétés électroniques, de nouveaux phénomènes intéressants sont attendus. Dans cette thèse nous avons montré que cette interface devient supraconductrice à des températures inférieures à 300 mK. La dépendance en température du champ magnétique critique in-

dique que le plan supraconducteur est bi-dimensionel (2D) avec une épaisseur d'environ 10 nm. Nous avons mis en évidence que la transition supraconductrice peut être interprétée en terme d'activation thermique de vortex libres, comme attendu dans la limite 2D. Une autre évidence de supraconductivité 2D est la transition de phase quantique vers un état isolant traditionnellement contrôlé soit par une augmentation du niveau de désordre soit par l'application d'un champ magnétique. Nous avons étudié ce phénomène sous l'effet de champs magnétiques et électriques. En effet l'application du principe du transistor à effet de champ à de nouveaux systèmes électroniques offre l'opportunité de contrôler leurs propriétés et en définitive leurs états fondamentaux. En utilisant cette approche, nous avons mis à jour un diagramme de phase caractérisé par un point critique quantique séparant une poche supraconductrice d'une phase localisée. La transition de phase quantique a lieu à une valeur de résistance proche de la résistance quantique des paires de Cooper. La tension de grille a été utilisée afin de contrôler la température critique et de mettre en évidence un régime sous-dopé et un régime sur-dopé.

La compréhension de la nature de la région isolante dans le diagramme de phase de ce système électronique est particulièrement importante. Nous avons mis en évidence une correction quantique à la conductivité, connue sous le nom de localisation faible qui résulte des effets d'interférences entre les électrons et produit un état fondamental isolant à partir d'un système 2D sans interaction ayant une concentration d'impuretés arbitrairement faible. Nous avons observé la dépendance de la conductivité en température et en champ magnétique caractéristique de ce mécanisme de localisation.

Nous avons également mis en évidence le rôle clé dans ce contexte de l'interaction spin-orbite, une manifestation remarquable de la relativité restreinte en mécanique quantique. À une interface, une rupture de symétrie d'inversion a lieu naturellement, entraînant la présence de forts champs électriques. En effet la grande distorsion polaire locale du $SrTiO_3$ à l'interface atteste de l'importance de ce phénomène. Nous avons montré que la correction quantique à la conductivité provenant de l'interférence des électrons peut promouvoir la délocalisation des charges dans le cas d'une interaction spin-orbite suffisamment forte. Cet effet est décisif dans les systèmes 2D, où une transition métal-isolant peut être induite. Nous avons évalué l'influence de cette interaction spin-orbite sur les propriétés électroniques du système en mesurant la magnétoconductance dans le régime à faible mobilité. Nous avons démontré que l'interaction spin-orbite peut être contrôlée par l'application d'une tension de grille. Nous avons également discuté la corrélation remarquable entre l'apparition d'une forte interaction spin-orbite et l'émergence de la supraconductivité. Le temps de relaxation de spin présente un comportement caractéristique associé à la brisure de symétrie d'inversion.

Nous avons aussi étudié des échantillons caractérisés par des mobilités suffisamment grande pour observer des niveaux de Landau bien définis dans des champs magnétiques de quelques Tesla. Nous avons observé des oscillations quantiques dans la résistance en fonction du champ magnétique. Ces oscillations dépendent uniquement de la composante perpendiculaire au plan de l'interface du champ magnétique. Ces résultats démontrent la présence d'états électroniques 2D provenant du confinement quantique. Une augmentation de la tension de grille entraine une augmentation de la mobilité, de la densité de charges et de la fréquence des oscillations. La fréquence de ces oscillations révèle une occupation multiple des sous-bandes du puits quantique ou une configuration à plusieurs vallées. Puisque la masse effective des porteurs

de charge obtenue de la dépendance en température de l'amplitude des oscillations est plus grande que la masse effective de l'électron libre, la séparation des niveaux d'énergie par effet Zeeman est plus grande que la séparation des niveaux de Landau. Ceci est un régime non-conventionnel, qui n'avait pas encore été exploré dans les hétérostructures de semi-conducteurs basé sur les composés III-V.

Finalement nous avons présenté une approche innovante, basée sur la lithographie à faisceau d'électrons, pour fabriquer des dispositifs dont les dimensions latérales sont de l'ordre du libre parcours moyen de l'électron et de la longueur de cohérence supraconductrice, typiquement 100 nm. Dans cette étude nous avons observé une grande modulation par effet de champ de l'état supraconducteur.

Introduction

Figure 1: Henri Matisse - La Leçon de piano, huile sur toile, 245x212, 1916, MoMA.

Je ne peins pas les choses, je ne peins que le rapport entre les choses.

Henri Matisse mastered the use of colour and form to convey emotions according to the principle outlined in this quote attributed to the great French artist. Rather than focusing on the minute details of his representations he believed that a powerful arrangement of different forms and colours is of paramount importance to communicate effectively through painting. His ideas are a source of inspiration for modern scientists, who have begun a quest for novel electronic properties in condensed matter by boldly associating materials of very different "colour".

A powerful driving force behind the information and communication technology revolution we have witnessed in the last decades is the ability to control on-demand the electronic properties of a material. The best example is the field effect transistor, a device whose ability to conduct an electrical current can be extensively controlled by applying an electric field. Several hundred million of these devices operate in one pocket, closely packed inside a smartphone. This functionality is made possible by the creation of an interface between two materials, a semiconductor and an insulator, that

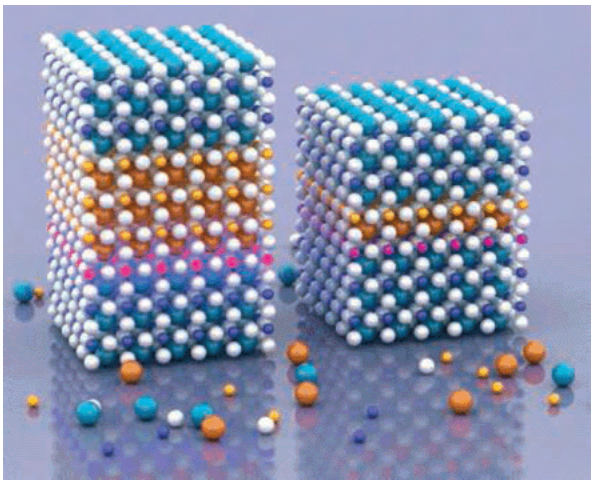

Figure 2: Models of heterostructures of lanthanum aluminate between strontium titanate layers. The atoms are represented by colored spheres (oxygen, white; lanthanum, orange; aluminum, yellow; strontium, large blue; and titanium, small dark blue). From Ref. [1] Credit: J. Huijben

in their bulk form do not offer useful properties. It is the interface which generates the functionality. An exciting opportunity, opened by recent advances in material science, is to study interfaces and surfaces of quantum materials that even in their bulk exhibit functional properties such as magnetism or superconductivity. Indeed, there is great potential for new electronic properties at their interfaces.

An important class of these novel materials is represented by the transition metal oxides where outstanding electronic properties such as ferroelectricity, superconductivity and colossal magnetoresistance are observed. This remarkable diversity is found in materials possessing a similar crystalline structure. This creates the opportunity to combine them in artificial crystals characterised by sharp interfaces, just like Lego bricks of different colours can be assembled in a single structure. A lively scientific community is currently exploring the properties of these artificial materials and the interest for the novel electronic properties found at their interfaces is increasing rapidly. These studies are fueling the growth of the semiconductors industry, as demonstrated by the recent integration of high-permittivity oxides in commercial transistors.

In this thesis we have studied the interface between an insulator, $LaAlO_3$, and a semiconductor, $SrTiO_3$, where a two-dimensional electron gas is found. This combination of materials is among the most intensely studied, as it establishes a connection between the world of complex oxides and conventional semiconducting heterostructures based on III-V compounds. As we will see in Chapter 1, $SrTiO_3$ is an outstanding semiconductor, that offers exciting functionalities such as superconductivity and a strong coupling between the electronic properties and the lattice. In this thesis we will consider how these phenomena emerge in the context of a two-dimensional electron gas. In Chapter 2 we will consider the superconducting properties of the $LaAlO_3/SrTiO_3$ interface and how these can be controlled using the field effect transistor approach. Since the electrostatic field effect is essentially an interface phenomenon,

we can anticipate particularly interesting results. Chapter 3 will be dedicated to the study of the carrier localisation and spin-orbit interaction in this system. In Chapter 4 we will demonstrate the presence of two-dimensional electronic states originating from quantum confinement. Finally, in Chapter 5 we will discuss an innovative approach, based on electron-beam lithography, to fabricate nanoscale devices.

Chapter 1

Functional interfaces

Interfaces between semiconductors have been extensively studied in the past. A new research direction that has emerged in recent years, thanks to extraordinary advances in fabrication techniques, is the study of the behaviour of interfaces between complex oxides. These materials, in contrast to semiconductors, exhibit a variety of physical phenomena originating from interactions among electrons. More importantly, there is potential for exciting new discoveries on their interfaces and surfaces. In this work we restrict our discussion to a narrow selection of materials characterised by a simple perovskite structure. We will begin by presenting the fascinating physics of these materials.

1.1 Functional oxides

A wide range of oxides of chemical formula $AB\,O_3$ (A and B are two cations) crystallizes at high temperatures in the cubic structure represented in Figure 1.1. This structure belongs to the space group $Pm\bar{3}m$ and, as highlighted in the same Figure, can be visualised along the 001 direction, as a stacking of AO and BO_2 planes. In these representations we can also appreciate that the B atom is surrounded by an oxygen octahedron. This atomic arrangement is found in the mineral perovskite ($CaTiO_3$), and for historical reasons this name was extended to the broad class of materials that share the same structure. However, this simple cubic arrangement is rarely their ground state. As the temperature is lowered these materials often undergo different structural transitions towards a lower-symmetry phase. These structural distortions can be classified in two groups, polar or non-polar, depending on whether or not the appearance of an electric dipole is associated with the transition. A typical non-polar instability, called antiferrodistortion (AFD), is an alternating rotation of the oxygen octahedra in opposite directions. On the other hand, these compounds can also develop a spontaneous polarization related to the displacement of the cations with respect to the oxygen, which is responsible for ferroelectricity (FE). The tolerance factor, defined as

$$f = \frac{r_A + r_O}{\sqrt{2}(r_B + r_O)} \tag{1.1}$$

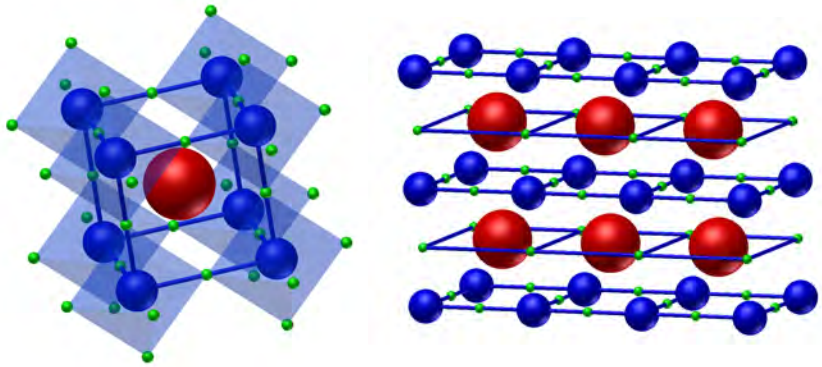

Figure 1.1: Left: perovskite structure $AB\,O_3$. The A atom is represented in red, the B atom in blue and the oxygen in green. Right: representation of the perovskite structure that highlights the stacking of AO and BO_2 planes.

where r_X is the ionic radius of the element X, helps us to predict which kind of distortion will occur. If $f > 1$ the material has a tendency towards polar FE distortions (in insulating compounds), while if $f < 1$ AFD instabilities dominate. Therefore, depending on the choice of cations, these oxides can display diverse physical properties. A cation with partially filled 3d shells, (among the most studied Ti, Mn, Ni and Cu) has proven to be a particularly interesting choice. Indeed, these orbitals give rise to narrow electronic bands, where the interactions between the electrons play an important role. Moreover the electrons delocalisation, being determined by the overlap between 3d orbitals and O 2p states, strongly depends on the nature of the structural distortion. Therefore a strong coupling between the lattice and charge, spin and orbital degrees of freedom is often observed. In these special conditions, the macroscopic behaviour of the solid is determined by a delicate balance between these different ingredients. A man-made perturbation of one of these elements can lead to large responses, that are potentially very interesting for applications. For example, in the manganese-based compounds, a magnetic field of a few teslas can induce a change of resistivity of several orders of magnitude, a phenomenon known as colossal magnetoresistance. Copper-based compounds, with a slightly more complex crystal structure, display superconductivity with the highest critical temperatures ever observed. These are examples of emergent phenomena, exotic new properties that cannot be anticipated using only a reductionist approach.

1.1.1 $SrTiO_3$

Let us consider a complex oxide that displays a particularly rich spectrum of physical properties: $SrTiO_3$. The lattice parameter of its cubic phase is 3.905 Å. This material is generally classified as a semiconductor, with a band gap of 3.2 eV that separates filled O 2p bands from Ti 3d bands [2]. Because the Ti atom is surrounded by an oxygen octahedron, the 3d levels are split by the crystal field into e_g and t_{2g} states (see Figure 1.9). $SrTiO_3$ can be electron doped by La substitutions on the Sr site, Nb substitutions

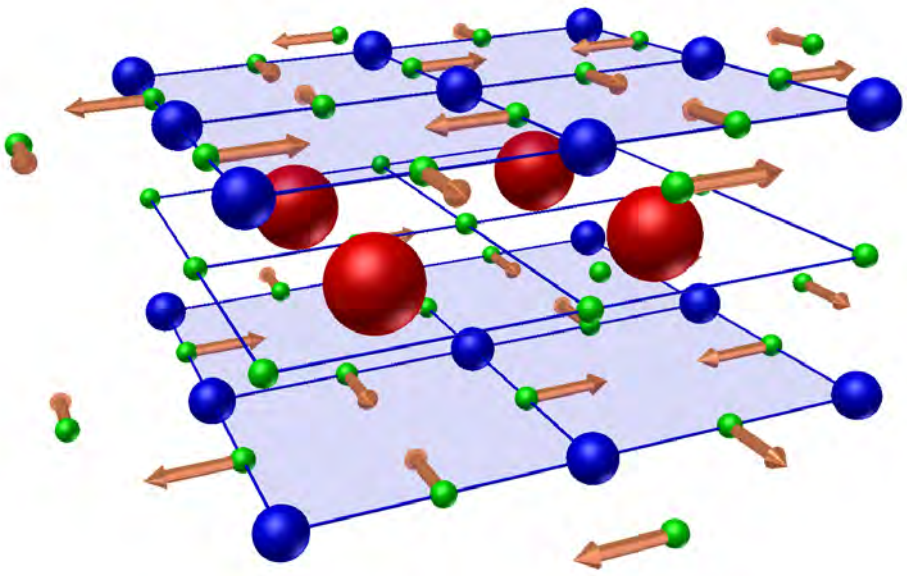

Figure 1.2: Antiferrodistortive displacement of the oxygen atoms (in green) of bulk $SrTiO_3$ in its low-temperature tetragonal phase.

on the Ti site or by creating oxygen vacancies. A transition towards a metallic state is observed at exceptionally low carrier concentrations ($\sim 10^{16}\,\mathrm{cm}^{-3}$) [3]. In the cubic phase three degenerate t_{2g} bands are partially occupied. At temperatures $<$ 1 K, a superconducting ground state is observed for electron concentrations between $8.5{\cdot}10^{18}\,\mathrm{cm}^{-3}$ and $3{\cdot}10^{20}\,\mathrm{cm}^{-3}$ [4]. The critical temperature goes through a maximum as a function of carrier density. The carrier mobility also depends on the carrier density and can be as high as $20000\,\mathrm{cm}^2/\mathrm{Vs}$.

The ionic radii of the elements present in the structure are Sr^{2+} ~132 pm, Ti^{4+} ~60.5 pm and O^{2-} ~140 pm. Since the tolerance factor is $f \simeq 0.96$, AFD instabilities dominate over FE distortions and drive a structural second order transition from a cubic to a tetragonal phase at ~105 K which doubles the unit cell. The oxygen atom displacement related to this AFD distortion is shown in Figure 1.2. The displacement occurs gradually as the temperature is lowered beneath the transition temperature. The maximum rotation of the oxygen octahedron is of the order of 2°. This phase transition not only brings about a domain structure in the crystal, but also significantly affects the electronic bands of the material, the most important effect being the lifting of the degeneracy of the t_{2g} levels [5]. Because this distorsion rotates the O atoms in the TiO_2 plane, the overlap of the Ti 3d orbitals with the O 2p orbitals decreases for the in-plane direction while it remains constant in the out-of-plane direction. Band structure calculations predict a pair of low-energy t_{2g} bands (d_{yz} and d_{zx}) and a third high-energy d_{xy} band [5]. The same analysis predicts that the spin-orbit interaction of the Ti ions causes a separation of the low-energy levels. Recent angle-resolved photoemission spectroscopy (ARPES) measurements provided a direct measurement of the Fermi surface in the tetragonal phase, shown in Figure 1.3 [6]. When the t_{2g}

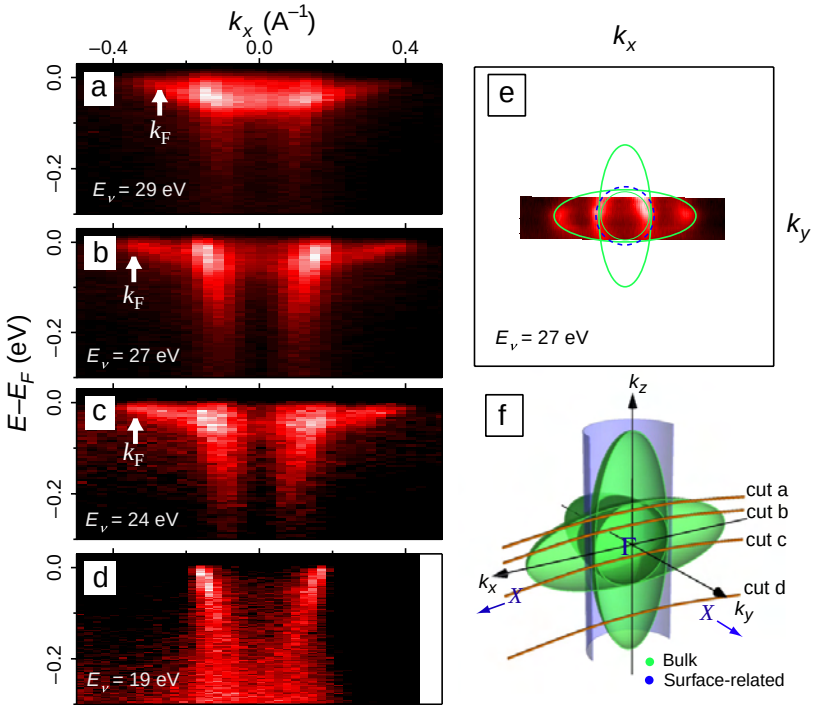

Figure 1.3: Fermi surface of $SrTiO_3$ measured by ARPES [6]. (a)-(d): Band dispersion along the (010) direction for different photon energies. (e) Fermi surface map. (f) Schematic Fermi surface.

levels are partially filled, it consists of an inner sphere and three ellipsoids along each axis. This particular shape arises from the strongly anisotropic dispersion of the 3d levels. Indeed each band is characterised by a strong curvature along two directions and one direction where the dispersion is nearly flat.

Some Authors claim that additional phase transitions are present in this material at 65 K (orthorhombic structure) and possibly at 10 K (rhombohedral structure) [7]. Analyses of the low temperature structural anomalies indicated that these are related to domain wall motion [8] and the only true structural phase transition occurs at 105 K.

Although FE instabilities were neglected so far in this discussion, they must be considered in order to form a complete picture. Detailed calculations of the phonon dispersion curves show that FE instabilities are in competition with the AFD distortions bringing about an extraordinary phenomenon. It was demonstrated that, although pure bulk $SrTiO_3$ remains paraelectric at any finite temperature, quantum fluctuations of an incipient ferroelectric phase are present and produce, at low temperatures, a large increase of the dielectric constant [9, 10, 11, 12]. This is illustrated in Figure 1.4, where a measurement of the dielectric constant of a single crystal of $SrTiO_3$ as a function of temperature is displayed. Since quantum fluctuations affect the dielectric properties of this material so dramatically, $SrTiO_3$ has been called a quantum paraelectric. This special property is also observed in a few other titanates ($EuTiO_3$ and $CaTiO_3$) and in $KTaO_3$. Because of the high lattice polarisability, a strong electron-phonon coupling is expected in this material. The optical conductivity of $SrTi_{1-x}Nb_xO_3$ shows an ef-

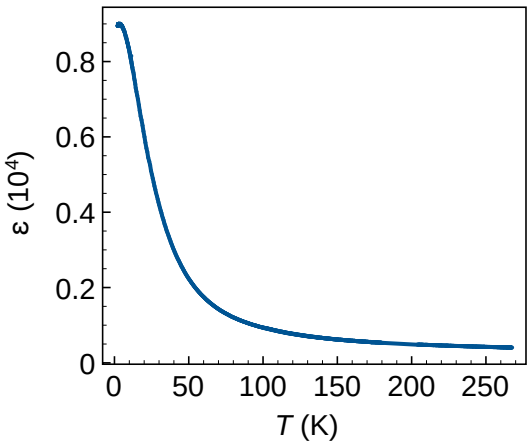

Figure 1.4: Dielectric constant ϵ as a function of temperature T of a a single crystal of $SrTiO_3$.

fective mass enhancement attributed to electron-phonon coupling and to the formation of large polarons [13] ($m^*/m_e = 1.9 \pm 0.3$), but not the gigantic renormalisation that one would naively expect in such a highly polarisable medium.

The high dielectric constant also explains the remarkably low carrier concentration at which a metallic state is observed. In fact, the donor binding energy is related to the dielectric constant ϵ_r by

$$E_D = -13.6\,\text{eV}\left(\frac{m_e^*}{m_e}\right)\epsilon_r^{-2} \tag{1.2}$$

which can be less than 1 μeV at low temperatures where $\epsilon_r \sim 10^4$ [3].

The ferroelectric state can be stabilised by chemical substitutions [14, 15, 16, 17], isotope exchange [18], electric fields [19], or by imposing a large strain to the structure [20, 21]. This can be accomplished by growing epitaxial thin films on different substrates.

Indeed, all these phenomena make $SrTiO_3$ an outstanding semiconductor. A two-dimensional electron gas hosted in this material can offer exciting functionalities such as superconductivity and a strong coupling between the electronic properties and the lattice. In this thesis we will explore both phenomena. In Chapter 2 we will consider the superconducting properties of a $SrTiO_3$-based two-dimensional electron gas. Chapter 3 will be dedicated to the study of the spin-orbit interaction in this system, which arguably is related to the unusual dielectric response of $SrTiO_3$. In Chapter 4 we demonstrate the presence of two-dimensional electronic states originating from quantum confinement in $SrTiO_3$. The rest of the present chapter is set aside to discuss the realisation of a two-dimensional electron gas in $SrTiO_3$-based heterostructures.

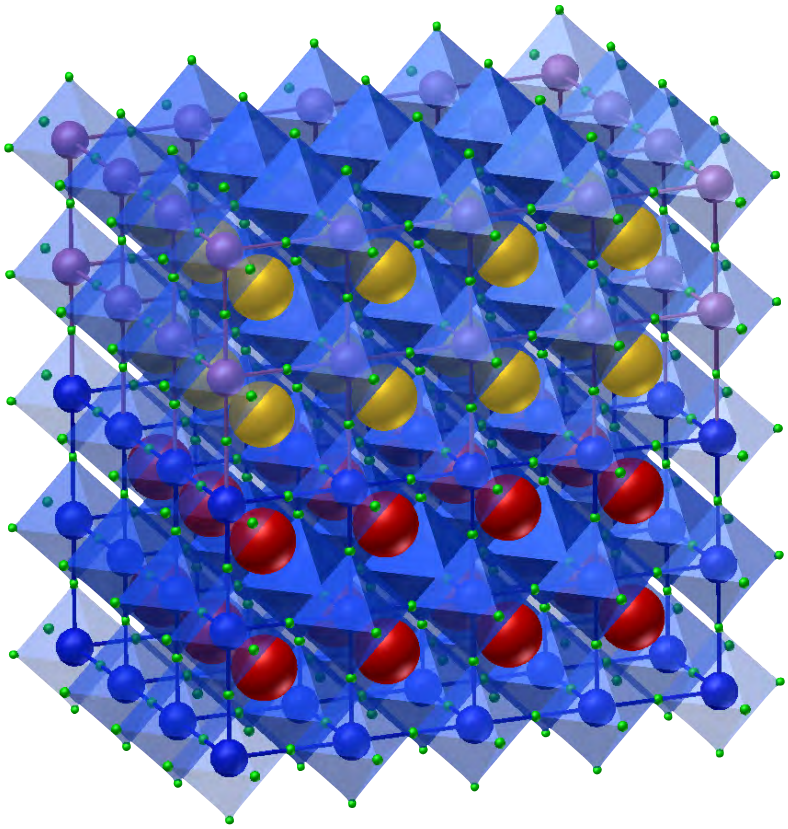

Figure 1.5: Model of heterostructure of lanthanum aluminate and strontium titanate. The atoms are represented by colored spheres (oxygen, green; lanthanum, yellow; aluminum, purple; strontium, red; and titanium, blue).

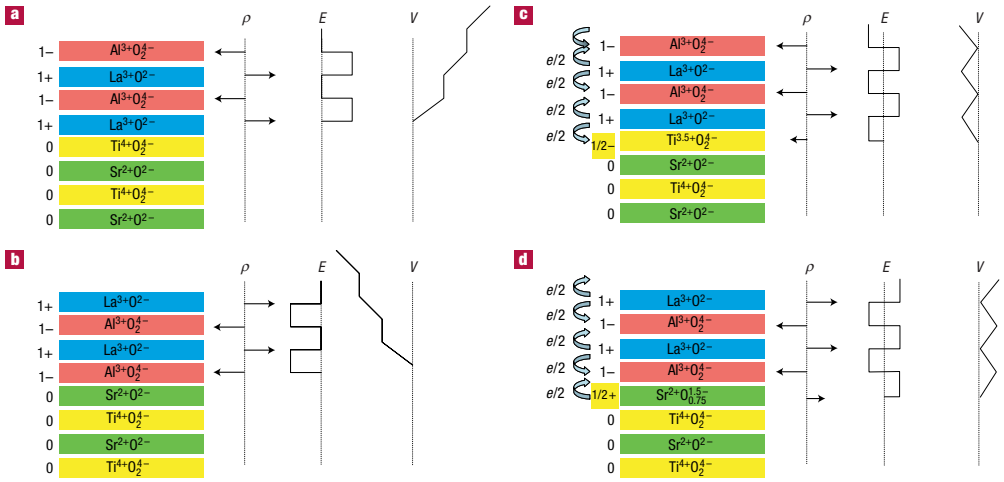

Figure 1.6: The polar discontinuity of the $LaAlO_3/SrTiO_3$ interface. a) Unreconstructed LaO/TiO_2 interface. b) Unreconstructed AlO_2/SrO interface. c) Reconstructed LaO/TiO_2 interface. d) Reconstructed AlO_2/SrO interface. From [24]

1.2 The conducting $LaAlO_3/SrTiO_3$ interface

In a landmark experiment performed in 2004 Ohtomo and Hwang considered the interface between $SrTiO_3$ and another insulating perovskite oxides, $LaAlO_3$ [22]. Using a chemical procedure previously developed [23] they prepared single crystals of (001)-$SrTiO_3$ characterised by a well defined TiO_2 termination, with atomically flat surfaces, with a step and terrace structure. On this substrate they deposited an epitaxial thin film of $LaAlO_3$ and they discovered that at the interface, a high mobility electron gas was present.

This result attracted enormous attention form the condensed-matter physics community since it heralded the birth of a new class of two-dimensional electron gases, hosted in exotic materials.

1.2.1 Doping mechanisms

The origin of the free carrier density found in $LaAlO_3/SrTiO_3$ interfaces is a controversial problem. In this section we will discuss the different doping mechanisms proposed in the literature and some experimental evidence favouring the different scenarios. A mechanism that is often discussed is related to the special charge distribution created in artificial $LaAlO_3/SrTiO_3$ heterostructures. Since, along the 001 crystallographic direction, $LaAlO_3$ is a polar material (that is, a stacking of charged $La^{3+}O^{2-}$ and $Al^{3+}O_2^{4-}$ planes), while $SrTiO_3$ is non-polar (that is, a stacking of neutral $Sr^{2+}O^{2-}$ and $Ti^{4+}O_2^{4-}$ planes), an atomically abrupt junction of these two oxides creates a polar discontinuity at the interface.

Two different atomic arrangements at the interface, illustrated in Figure 1.6, can be considered: LaO/TiO_2 or AlO_2/SrO. In both cases, an atomically abrupt interface between polar and non-polar layers generates an electrostatic potential which diverges

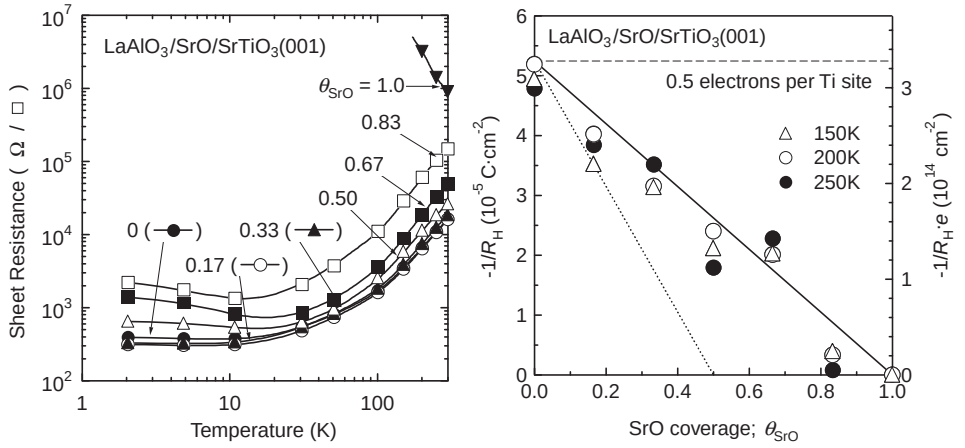

Figure 1.7: Left: SrO fractional coverage dependence of the sheet resistance. Right: SrO fractional coverage dependence of the inverse Hall coefficient. From Ref. [29]

with thickness of the polar layer (polar catastrophe). Indeed the charge dipole generated by this charge arrangement is not negligible. Even considering a bulk dielectric screening of the electric field ($\epsilon_r = 25$), which is certainly an overestimation, a shift in electrostatic potential of about 1 V is produced for each layer of $LaAlO_3$. Arguably, as the number of layers grows, the accumulated electrostatic energy becomes larger than the energy cost associated with a rearrangement of the atomic or electronic structure. At a thickness of 4-6 u.c. (depending on the dielectric screening) this electrostatic energy becomes of the order of the $LaAlO_3$ band gap (5.6 eV) and a transfer of charge from the valence band of $LaAlO_3$ to the conduction band of $SrTiO_3$ can take place [25].

A polar discontinuity is the driving force behind a number of interesting electronic, ionic and chemical reconstructions observed in polar surfaces and interfaces. For example the polar (111) surface of K_3C_{60}, a superconducting material, undergoes an electronic reconstruction that changes the valence of the C_{60} ions [26]. The surface of NiO (111) undergoes either a chemical reconstruction, by incorporating hydroxyl groups on the surface, or an ionic rearrangement [27]. Finally, a well known example from the semiconductors is the (001) heterojunction between Ge and GaAs, where a 50% intermixing of Ge and Ga atoms at the interface is driven by the polar discontinuity [28].

In $LaAlO_3/SrTiO_3$ heterostructures the polar discontinuity can cause the reconstruction of both the interface and the surface. In LaO/TiO_2 interfaces, a charge corresponding to -$|e|$/2 per unit cell missing from the surface and transferred to the interface, would result in a more favorable electrostatic configuration (see Figure 1.6). This can be accomplished by an electronic reconstruction involving a change of valence of titanium to $Ti^{3.5+}$, which corresponds to an electron density of $3.3{\cdot}10^{14}\,\mathrm{cm}^{-2}$, hosted in the Ti 3d bands at the interface [24]. In the case of the AlO_2/SrO interface, a more stable charge arrangement can be obtained by transferring +$|e|$/2 per unit cell from the surface to the interface. Since a $Ti^{4.5+}$ configuration is not accessible, in this case an ionic reconstruction seems inevitable.

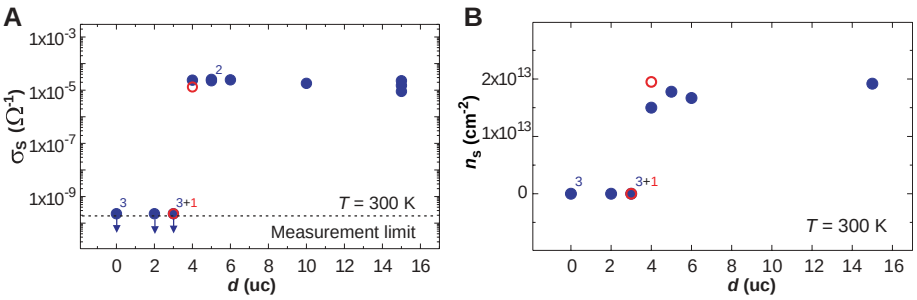

Figure 1.8: (A) Sheet conductance and (B) carrier density as a function of the number of their $LaAlO_3$ unit cells. From Ref. [30]

Experimentally it is observed that the LaO/TiO_2 interface is conducting while the AlO_2/SrO interface is insulating [22]. In Figure 1.7 the sheet resistance as a function of temperature of $LaAlO_3/SrTiO_3$ interfaces, characterised by a different coverage by SrO of a TiO_2 terminated $SrTiO_3$ substrate, is shown [29]. A transition towards a highly insulating state is observed as the coverage by SrO becomes complete, indicating that the atomic configuration of the interface defines the electronic properties of this system. This is a very important result that demonstrates that the conducting state observed in this system is an interface effect.

Another experimental evidence that supports this scenario is the observation of a remarkable dependence of the transport properties of this system on the thickness of the $LaAlO_3$ layer, which is shown in Fig. 1.8. Samples in which the thickness of $LaAlO_3$ is less than 4 u.c. don't display any conductivity. At 4 u.c. a sharp metal to insulator transition is observed. This striking result was first reported by the Augsburg group in 2006 [30], and it has since been reproduced in various laboratories around the world, including Geneva.

Some argue that these two experimental observations indicate that an intrinsic doping mechanism is at play. However, an interpretation of this conducting state based exclusively on the electrostatic picture we previously discussed is quite unsatisfying. This model suffers from three main problems: it predicts a large carrier density that is not experimentally observed, it neglects any other mechanism of compensation of the polar discontinuity such as polar distortions and atomic intermixing and it does not consider the role of defects.

Indeed, another possible doping mechanism is related to the creation of defects in $SrTiO_3$ during the growth of the $LaAlO_3$ layer, such as oxygen vacancies and atomic intermixing. $SrTiO_3$ is a material that is particularly sensitive to chemical doping, since it undergoes a metal to insulator transition at a low critical carrier density of $n_c \simeq 10^{16}\,\mathrm{cm}^{-3}$. As we will discuss later in detail (Section 1.4), the electronic properties of the system can be very sensitive to the preparation conditions. Several groups have investigated samples prepared in conditions favoring the creation of oxygen vacancies in $SrTiO_3$ [31, 32, 33]. Herranz et al. reported quantum oscillations of the electrical resistance as a function of magnetic field in heterostructures characterized by a large carrier density (of the order of 10^{16} cm^{-2}) [31]. The oscillations in such samples are independent of the direction of the applied magnetic field, pointing to a

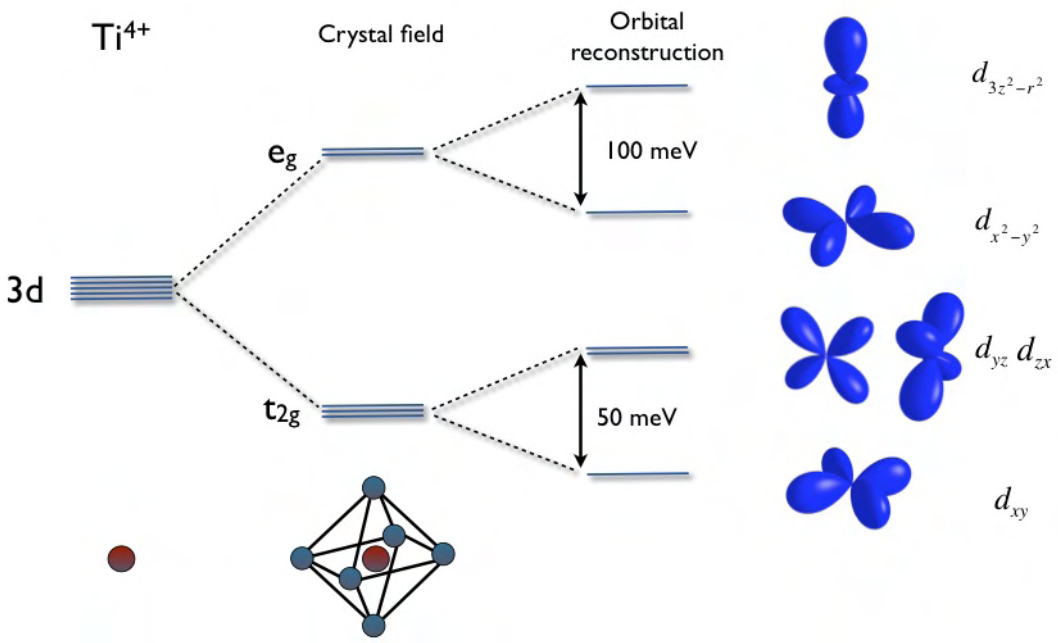

Figure 1.9: Electronic structure of the $LaAlO_3/SrTiO_3$ interface. Ti 3d energy levels deduced from room temperature x-ray absorption spectroscopy [35].

three dimensional Fermi surface and a thickness of the conducting layer corresponding to the whole $SrTiO_3$ crystal.

Other authors have focused their attention on the atomic intermixing at the interface. Nakagawa et al. [24] performed a electron energy loss spectroscopy study with atomic resolution across the AlO_2/SrO and LaO/TiO_2 interfaces. In both cases a significant intermixing of La, on the scale of a few u.c., was detected. At the AlO_2/SrO interface a higher concentration of oxygen vacancies with respect to the LaO/TiO_2 interface was measured. Willmott and collaborators used surface X-Ray diffraction to determine the atomic structure of a five-monolayer film of $LaAlO_3$ on $SrTiO_3$ [34]. They found cationic mixing at the interface together with large atomic distorsions. They inferred from their result that the conductivity in this system is related to the formation of a metallic $La_{1-x}Sr_xTiO_3$ layer.

This thesis will not tackle the doping problem in this system. We will rather focus our attention to its special electronic properties. Nevertheless, we will not neglect the material science issues related to this study. In Section 1.3 we describe in detail how the samples used in this study are prepared and in Section 1.4 we analyse the role of the fabrication conditions in determining the electronic properties of the interface.

1.2.2 Electronic structure

Several experimental and theoretical studies have uncovered a number of remarkable electronic properties of this novel two-dimensional electron gas. We already mentioned the crucial role of the substrate termination to obtain a conducting interface and

the striking metal to insulator transition as a function of thickness. For $LaAlO_3$ films that are up to 3 u.c. thick, insulating interfaces are obtained. In a field-effect transistor configuration that uses the $SrTiO_3$ substrate as gate dielectric, a phase transition to the conducting state can be driven by an electric field [30]. At low temperatures (around 200 mK), a transition towards a two-dimensional superconducting ground state is observed (see Chapter 2). Unusual magnetotransport properties are also observed in this temperature range, and have been attributed to magnetic effects [36]. In this work we will provide an alternative interpretation (see Chapter 3).

X-Ray absorption spectroscopy experiments indicate that an orbital reconstruction occurs at this interface [35]. The electronic configuration that emerges from these studies is illustrated in Figure 1.9. The most remarkable feature is that the degeneracy of the Ti 3d levels is removed and the first available states for the conducting electrons have a $3d_{xy}$ character. Since the next accessible levels are separated by an energy of about 50 meV the conduction should be dominated by $3d_{xy}$ bands, which are strongly two-dimensional and present a negligible inter-plane coupling. This band configuration is completely different from the one found in bulk $SrTiO_3$. As we previously pointed out, in the bulk compound the lowest available levels are the $3d_{yz}$ and $3d_{zx}$ states. At the $LaAlO_3/SrTiO_3$ interface the band's ordering is reversed. Arguably, this electronic configuration is hardly compatible with a AFD distorted material. In fact, it was demonstrated in a remarkable transmission electron microscopy experiment [37] that at this interface $SrTiO_3$ undergoes a polar distorsion [38]. As shown in Figure 1.10, the oxygen atoms are displaced towards $LaAlO_3$, as a result of a combination of octahedra rotations and atomic relaxations. In this thesis we will consider the impact of this phenomenon in the low-energy electronic structure of the electron gas in the form of a strong spin-orbit coupling (see Chapter 3). Another interesting ingredient is the sub-bands fine structure brought about by the momentum quantization in the potential well. This was calculated using density functional theory [39, 40] (see Figure 1.11) and the results are in agreement with the orbital reconstruction observed in X-Ray absorption spectroscopy. In this thesis we will discuss the presence of two-dimensional electronic states originating from quantum confinement using the Shubnikov-de Haas effect (see Chapter 4).

1.2.3 Confinement

Several experiments have studied the confinement depth of the electrons from the interface. A direct visualisation of the extention of the confinement was provided by the experiment of Basletic and collaborators [41]. In this work the spatial distribution of charge carriers was mapped by conducting tip atomic force microscopy. It was demonstrated that using appropriate fabrication conditions, a localisation within 7 nm from the interface can be obtained (see Fig. 1.12). The problem of the influence of the preparation conditions on the electronic properties of this system is discussed in details in Section 1.4.

The confinement depth was also determined using infrared ellipsometry [42] and hard X-Ray photoelectron spectroscopy [43]. These experiments are in agreement with the picture of a localisation within a few nanometers from the interface. In this work we will discuss the anisotropy of the critical magnetic fields in the superconducting state to set an upper limit to the thickness of the conducting layer (see Chapter 2).

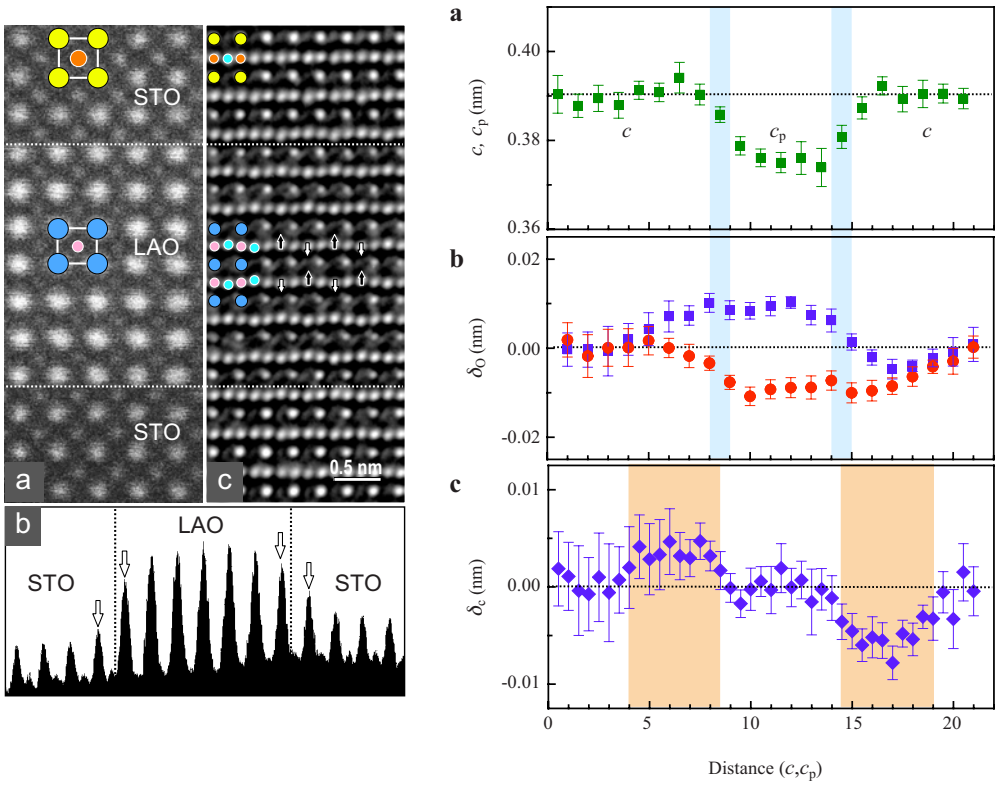

Figure 1.10: Adapted from Ref [38]. Left-hand side: (a) Scanning transmission electron microscopy high-angle annular dark field image of a 2.5 nm $LaAlO_3$ layer sandwiched between two $SrTiO_3$ layers taken along the crystallographic (100) direction. The two dotted lines indicate the interfaces. Sr and La atoms are given by large circles and Ti atoms and Al atoms by small circles. (b) Intensity profile of the image averaged over an area along the interfaces. (c) Image taken in a transmission electron microscope under negative spherical aberration conditions. An oxygen octahedra rotation is clearly visible in both materials. Right-hand side: (a) c-lattice parameter in $SrTiO_3$ and c_p-lattice parameter in $LaAlO_3$ as functions of distance in units of c and c_p, respectively from a reference plane in the lower $SrTiO_3$ layer. The vertical shade lines mark the interfaces. (b) Shift of the oxygen atoms δ_O as a function of distance from the reference plane. Squares denote upward shifts and circles denote downward shifts. (c) Shift δ_c of the center of the oxygen octahedra with respect to the cation.

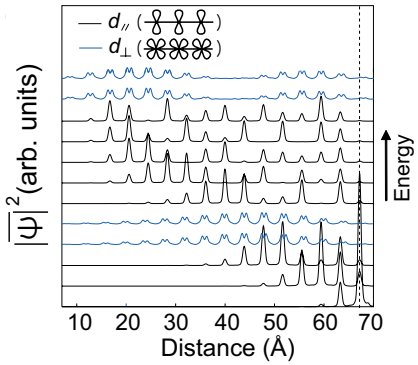

Figure 1.11: xy average of squared wave functions for low-lying energy states at the Γ point. $d_{||}$ indicates orbitals that are parallel to the interface (d_{xy}) and $d_{\perp}$ that are perpendicular to the interface (d_{yz} and d_{zx}). The vertical dashed line shows the position of interfacial Ti site. From [39].

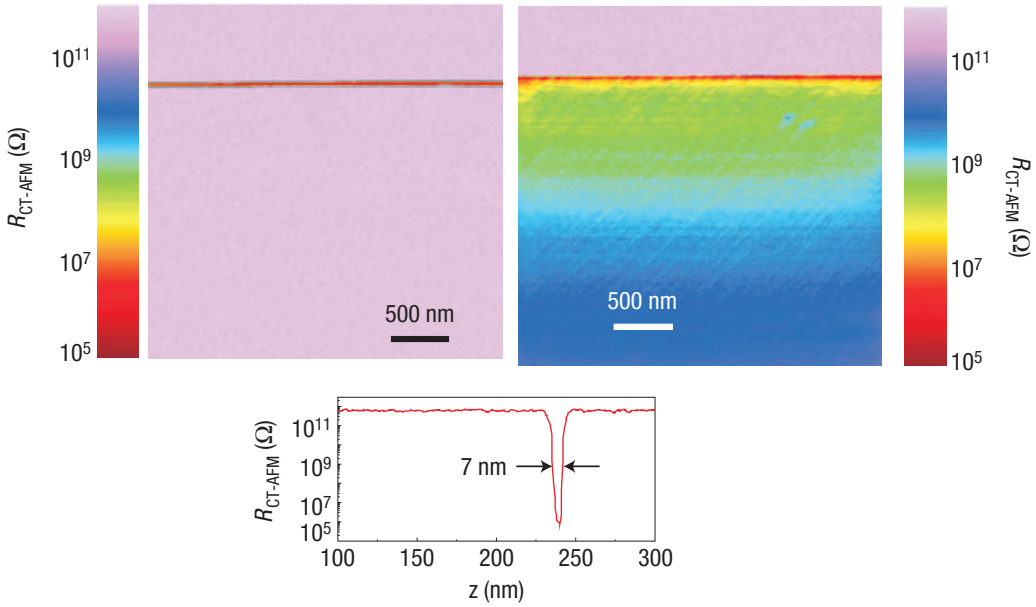

Figure 1.12: Top: Conducting tip AFM mapping around the interface for a sample fabricated using oxygen-rich (left-hand side) and oxygen-poor conditions (right-hand side). Bottom: resistance profile across the interface for the left-hand side sample. From [41]

1.3 Fabrication of $LaAlO_3/SrTiO_3$ heterostructures

In this section we will discuss the growth and characterisation of $LaAlO_3/SrTiO_3$ heterostructures. The samples used in this work were prepared in Geneva by depositing a $LaAlO_3$ thin film on top of a TiO_2-terminated $SrTiO_3$ single crystal. The growth technique we utilised is pulsed laser deposition (PLD), performed using a KrF excimer laser delivering pulses of 25 ns at 248 nm. When these energy pulses hit a target located inside a deposition chamber in a controlled oxygen atmosphere, an ablation process occurs. The ionised particles emitted from the the target strongly interact with the gas present in the chamber and a plasma plume is generated, which is directed towards a heated substrate. This technique allows the growth of complex materials and is widely used in research laboratories. Unfortunately, the slow deposition rates and the small surface coatings that can be obtained hinder today its use in an industrial setting. The main parameters we can control during a PLD growth are the laser fluence and repetition rate, the temperature of the substrate, the oxygen pressure, the distance plume-substrate and its orientation, the thickness of the film (deposition time) and the annealing procedure.

The deposition procedure is the following: a $SrTiO_3$ crystal, supplied by CrysTec GmbH (volume $5 \times 5 \times 0.5\,\mathrm{mm}^3$), is chemically treated to obtain a single TiO_2 termination. The substrate is pasted on a thin nickel oxide plate (surface $10 \times 10\,\mathrm{mm}^2$) using silver epoxy and heated for 1 hour at 120 °C in air to ensure a good adhesion. The plate is then clamped to a sample holder from which it is thermally decoupled by a sapphire crystal. Before being transferred into the deposition chamber the sample holder sits for 30 minutes at 290 °C in vacuum (10^{-6} mbar) in a load-lock compartment. The base pressure of the deposition chamber is typically 10^{-9} mbar. Once the sample is introduced into the chamber the pressure is increased to a desired value (discussed below) and the substrate is heated by an infrared laser focused on the backside of the nickel plate. The infrared power is delivered progressively and the sample is heated to the deposition temperature (discussed below) in about 1 hour. The temperature of the substrate is measured by a laser pyrometer set to the emissivity of the epoxy paint (0.85). Once the appropriate temperature is reached, the film's growth takes place, when energy pulses coming from the excimer laser hit a rotating target (either a polycrystalline pellet or a single crystal of $LaAlO_3$). The laser beam is focused on an area of $5 \pm 0.3\,\mathrm{mm}^2$ and carries an energy of 50 mJ (fluence $1\,\mathrm{J/cm}^2$). The repetition rate is 1 Hz, the plume is oriented perpendicular to the substrate and the distance between the target and the sample is 7 cm. The size and colour of the plasma plume strongly depend on the oxygen pressure. A photograph of the deposition chamber taken during the growth is shown in Fig. 1.13.

During the deposition we can monitor the film's growth using reflection high energy electron diffraction (RHEED). This technique consists of directing a high energy electron beam (21 keV) in grazing incidence on the surface of the sample. The electrons are diffracted and hit the surface of a fluorescent screen where a diffraction pattern appears. This pattern contains information regarding the surface of the sample. Typically one distinguishes between the pattern produced by a rough surface (three-dimensional transmission pattern) or by an atomically flat surface (two-dimensional diffraction). Moreover, if the conditions to obtain a layer-by-layer growth of the film are fulfilled, the intensity of a diffraction spot oscillates as a function of time during

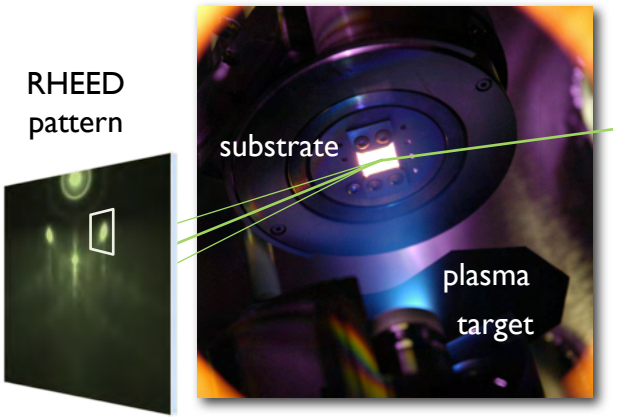

Figure 1.13: Right: picture of the pulsed laser deposition chamber taken during growth. Left: reflection high energy electron diffraction pattern of a $SrTiO_3$ surface.

the deposition. The minimum of the oscillation corresponds to a half-covered surface, while the maximum indicates a complete covering. The RHEED oscillations observed during the growth of a particularly thick sample (110 u.c.) are shown in Fig. 1.14. The persistence of a layer-by-layer growth mode even for such a large thickness is indicative of the high crystalline quality of the films. In the same figure, the electron diffraction pattern observed for a 6 u.c. film is displayed. This pattern is indicative of an atomically flat film with a step and terrace structure.

After deposition the oxygen pressure is increased to 0.2 bar, while the infrared laser power is kept constant. The introduction of the oxygen lowers the sample temperature. These conditions are kept constant for 1 hour after which the sample is cooled down to room temperature in the same oxygen pressure by gradually decreasing the laser power. The role of this annealing is discussed below.

The samples fabricated following this procedure are systematically characterised by atomic force microscopy (AFM) and X-Ray diffraction (Fig. 1.15). The pseudo-cubic bulk lattice parameter of $LaAlO_3$ is 3.79 Å, therefore the films grown on $SrTiO_3$ (cubic structure with lattice parameter 3.905 Å) are under tensile strain. We remark that the misfit strain (3%) is particularly large. For very thin films, finite size effects produce a widening of the diffraction peak, which makes it difficult to distinguish it from the substrate contribution. Reciprocal space maps reveal that films up to 20 u.c. are tetragonal and fully strained. Thicker films display a relaxation of both c and a-axis toward the bulk value. AFM topography of films thinner than 20 u.c. reveal an atomically flat surface with a step and terrace structure that reproduces the one observed in the $SrTiO_3$ substrate before deposition. Films thicker than 20 u.c. exhibit cracks in the AFM topography, concomitantly with the structural relaxation.

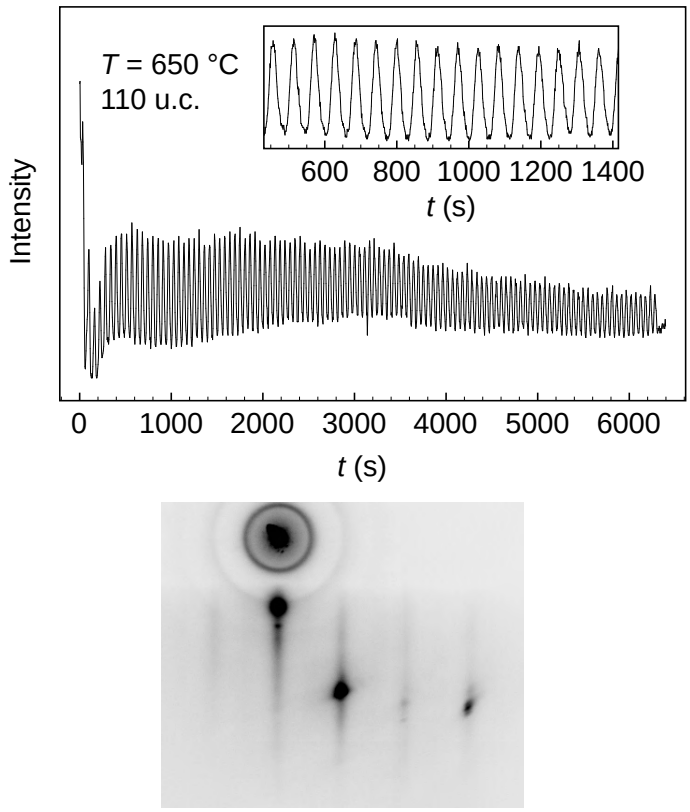

Figure 1.14: Up: intensity of the diffracted electron beam as a function of time during the deposition of 110 u.c. of $LaAlO_3$ at 650 °C. Inset: detail of the same data. Down: reflection high energy electron diffraction pattern of a $LaAlO_3$ thin film 6 u.c. thick.

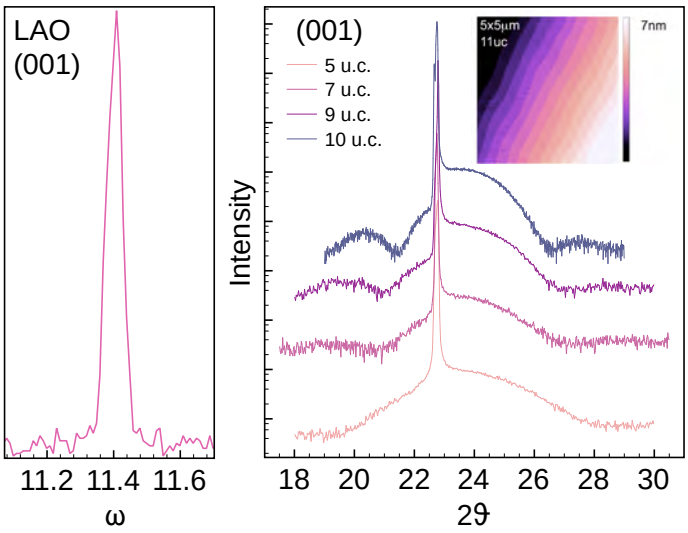

Figure 1.15: Right: $\theta - 2\theta$ diffractograms around the 001 reflection of a series of $LaAlO_3$ thin films of different thickness deposited on $SrTiO_3$. Inset: atomic force microscopy topography of a 11 u.c. thick sample. The steps height is 1u.c. This structure reproduces the one observed in the $SrTiO_3$ substrate before deposition. Left: ω scan of a 7 u.c. thick sample. The width of the peak corresponds to the one observed in the $SrTiO_3$ substrate.

1.4 Influence of the growth conditions on the $LaAlO_3/SrTiO_3$ interface electronic properties

When preparing oxide heterostructures by PLD, several parameters can be experimentally controlled. We will show that, in order to study the intrinsic electronic properties of the novel two-dimensional electron gas found at the interface between $LaAlO_3$ and $SrTiO_3$, a well defined window of growth parameters must be used. We will discuss the role of the thickness of the $LaAlO_3$ layer, of the oxygen pressure and of the substrate temperature in determining the structural and electronic properties of $LaAlO_3/SrTiO_3$ heterostructures.

1.4.1 Thickness of the $LaAlO_3$ layer

$LaAlO_3/SrTiO_3$ heterostructures present a remarkable dependence of their transport properties on the thickness of the $LaAlO_3$ layer, which are summarised in Fig. 1.16. Samples in which the thickness of $LaAlO_3$ is less than 4 u.c. do not display any conductivity (if any conductivity is present, it is smaller than the measurement limit). At 4 u.c. a sharp metal to insulator transition is observed towards a finite conductivity. The corresponding sheet resistance is of the order of $100\,\Omega/\square$ at 4 K. We remark though, that in order to observe this transition an annealing step must be performed after deposition. A 2 u.c. sample which is not annealed is metallic. This shows that defects, notably oxygen vacancies, can be created during growth, as highlighted by several

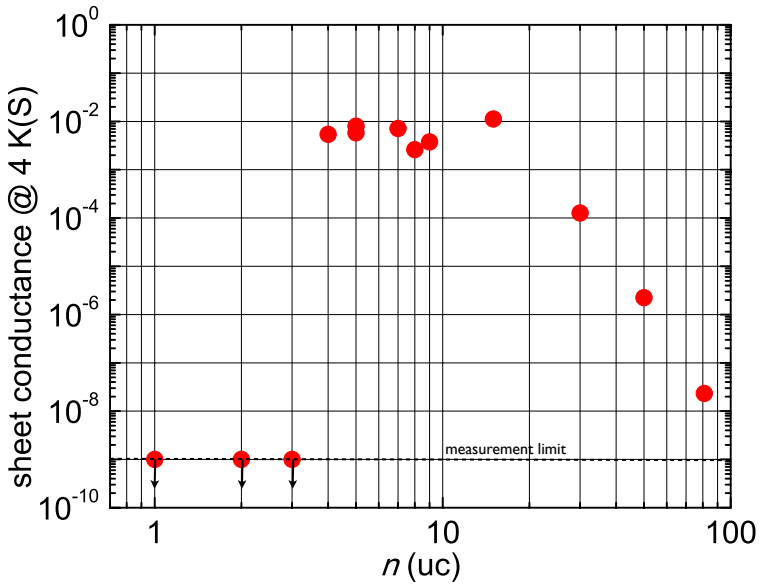

Figure 1.16: Sheet conductance of $LaAlO_3/SrTiO_3$ interfaces measured at $T = 4\,\mathrm{K}$ as a function of the thickness of the $LaAlO_3$ layer.

authors [31, 32, 33]. Up to around 20 u.c. the conductivity does not show a clear dependence on thickness. Rather, a scattering of the data in the region 10^2-$10^3\,\Omega/\square$ (measured at low temperature) is observed. This is consistent with sample-to-sample variations of the level of disorder and of the carrier density. Thicker samples, in which the $LaAlO_3$ layer undergoes a structural relaxation, show a remarkable decreased conductivity and mobility [44]. The metallic state sharply decays with increasing thickness and the system displays a crossover towards a strongly localised regime.

According to these results, we restrict our study of the electronic properties of the $LaAlO_3/SrTiO_3$ interface to samples between 4 and 20 u.c. thick, since thicker samples are highly disordered and not representative of the ideal system.

1.4.2 Oxygen pressure and annealing procedure

In this section we will discuss the role of the oxygen pressure used during deposition. In this study the temperature of the substrate during growth is 800 °C. Two series of three samples were prepared in 10^{-2} mbar, 10^{-4} mbar $1.3 \cdot 10^{-6}$ mbar. In one series of samples the annealing step previously described has been carried out. During the annealing step, the substrate temperature decreases to about 530 °C. To identify the role of the oxygen annealing procedure, this step has not been carrier out for the second series of samples. Structural characterizations do not reveal any influence of the oxygen pressure used during the deposition or of the annealing process on the crystalline quality of the structures.

First we analyze the results obtained on samples with an oxygen post-annealing. As can be seen from Fig. 1.17 a, the values and temperature evolution of the sheet resistances for samples grown at different pressures are very similar. The Hall resis-

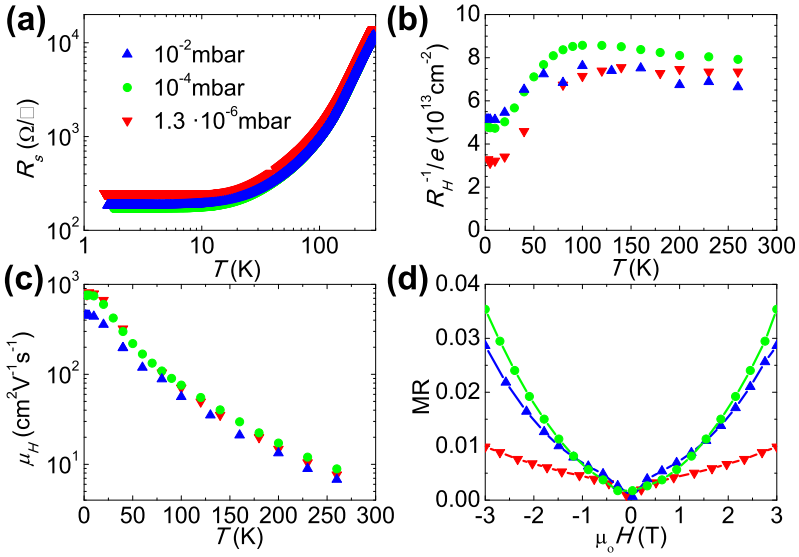

Figure 1.17: Transport properties of annealed (0.2 bar oxygen pressure) samples with a 5 u.c. $LaAlO_3$ thickness and grown at different oxygen pressures (blue up triangles 10^{-2} mbar, green circles 10^{-4} mbar and red down triangles $1.3 \cdot 10^{-6}$ mbar). (a) Sheet resistance, (b) inverse Hall constant and (c) Hall mobility as a function of temperature and (d) magnetoresistance at 1.5 K.

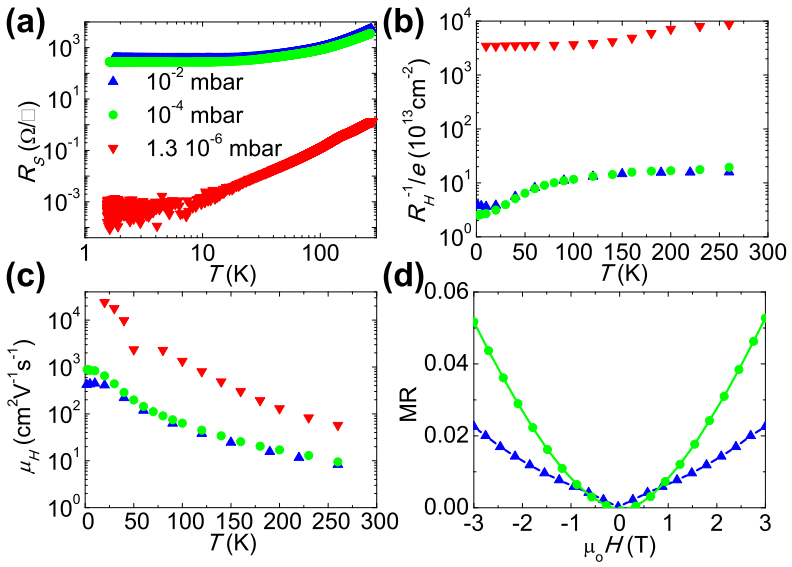

Figure 1.18: Transport properties of samples with a 5 u.c. $LaAlO_3$ thickness and grown at different oxygen pressures (blue up triangles 10^{-2} mbar, green circles 10^{-4} mbar and red down triangles $1.3 \cdot 10^{-6}$ mbar) without in-situ annealing. (a) Sheet resistance, (b) Hall mobility and (c) inverse Hall constant as a function of temperature and (d) magnetoresistance at 1.5 K.

tance, measured between -3 and +3 T, has a linear dependence on magnetic field. The inverse Hall constant, shown in Fig. 1.17 b as a function of temperature, shows little variation among the samples investigated. We note that the temperature dependence observed for the Hall resistance is also observed for Nb-doped $SrTiO_3$ thin films. Consequently, the Hall mobility displayed in Fig. 1.17 c is essentially not affected by the oxygen deposition pressure. Finally, a positive magnetoresistance of similar magnitude is observed for all the samples (Fig. 1.17 d). We can conclude, according to the results shown in Fig. 1.17, that the transport properties of samples grown at different oxygen pressures are essentially the same if oxygen annealing follows the growth.

Let us now turn to the relevance of the annealing process to the electronic properties. Previous studies on non-annealed samples describe a strong dependence of the transport properties on the growth oxygen pressure [36, 32]. The room temperature sheet resistance was observed to vary over 5 orders of magnitude as the oxygen pressure was changed from 10^{-6} to $2.5 \cdot 10^{-3}$ mbar. Here, we focus on samples with a 5-10 u.c. $LaAlO_3$ layer thickness, for the reasons previously indicated. As shown in Fig. 1.18, for $LaAlO_3/SrTiO_3$ interfaces grown at 10^{-6} mbar, the effect of the annealing is most evident. It is well known that oxygen vacancies, induced by high temperature annealing in low oxygen pressures, provide electron carriers to $SrTiO_3$ crystals [45, 46]. The unannealed samples grown at 10^{-6} mbar display a room temperature sheet resistance and carrier density of $1\,\Omega/\square$ and 10^{17} cm^{-2} respectively (Fig. 1.18 a, b), suggesting a conduction dominated by oxygen vacancies induced in the bulk of the $SrTiO_3$ substrate. This result is consisted with several previous reports, including the

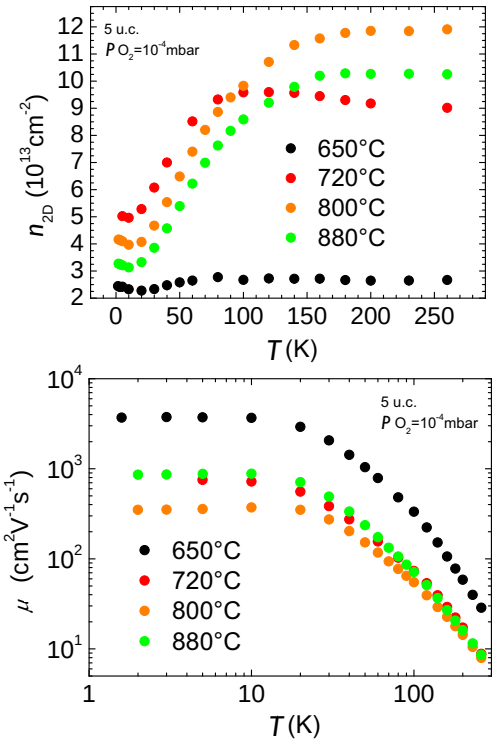

Figure 1.19: Influence of the deposition temperature on the electronic properties of $LaAlO_3/SrTiO_3$ interfaces. Top: Hall carrier density n_{2D} as a function of temperature T for 5 u.c. samples grown at different temperatures. Bottom: Hall mobility μ as a function of temperature T for 5 u.c. samples grown at different temperatures.

one from the Paris group, reproduced in Fig. 1.12.

Higher oxygen pressures during the growth substantially reduce the presence of oxygen vacancies even if the annealing step is not performed, as shown in Fig. 1.18. The carrier densities of samples grown at 10^{-4} and 10^{-2} mbar are very similar and estimated to be 10^{14} electrons/cm^2 at 100 K, a value three orders of magnitude smaller than the one of samples grown at a 10^{-6} mbar oxygen pressure. The mobility, similar for the 10^{-4} and 10^{-2} mbar samples, is one order of magnitude smaller for low oxygen pressure samples (see Fig. 1.18 c). One thus concludes that the transport properties of samples (5-10 u.c. thick) grown at 10^{-4} and 10^{-2} mbar are only slightly affected by the oxygen annealing.

1.4.3 Temperature

The last deposition parameter to be analysed is the temperature of the substrate. This parameter has a strong bearing on the structural properties of the $LaAlO_3$ film that we grow, and this in turn is reflected on the electronic properties of the interface. The optimal deposition temperature is 650 °C, where the RHEED pattern has the highest quality and the intensity oscillations are more persistent (see Figure 1.14). As we

increase the temperature a damping of the RHEED oscillations is observed and the structural relaxation of the film takes place more rapidly. Samples grown at 650 °C exhibit the highest mobilities (up to 6000 cm^2/Vs) and lowest carrier densities. In Figure 1.19 the mobilities and carrier densities of samples of the same thickness (5 u.c.) grown at different temperatures are shown. Samples grown at temperature higher than 700 °C present similar carrier densities and lower mobilities (of the order 500 cm^2/Vs). We will exploit this dependence of the mobility on the preparation conditions to study samples characterised by different levels of disorder.

In summary, in this thesis we will focus our discussion on $LaAlO_3/SrTiO_3$ interfaces prepared by PLD using the following conditions: substrate temperature either 650 °C or 800 °C, pressure $\sim 1 \times 10^{-4}$ mbar of O_2 and a repetition rate of 1 Hz. The fluence of the laser pulses is 1 J/cm^2. After growth, each sample is annealed in 200 mbar of O_2 at about 530 °C for one hour and cooled to room temperature in the same oxygen pressure. The thickness of the $LaAlO_3$ layer is always between 4 and 15 u.c..

Chapter 2

Electric field control of interfacial superconductivity

2.1 Quantum phase transitions

2.1.1 Central ideas on phase transitions

Phase transitions play an important role in our everyday life. Most of us regularly boil a kettle to make a nice cup of tea or check for ice on the road before driving a car. The phase transitions we normally witness occur at finite temperatures T: upon heating, a microscopic order such as the crystal structure of the ice is destroyed and, at the transition temperature, a new phase, characterised by a higher symmetry, emerges. In an important class of phase transitions, called *continuous*, the two phases do not coexist at the transition temperature and the state of the system can be characterised by a thermodynamic quantity, the *order parameter* $\Psi(\mathbf{r}, t)$, whose thermodynamic average is zero in the high symmetry (disordered) phase and non-zero in the low symmetry (ordered) phase [47]. In this context the transition temperature $T_{\rm c}$ is called *critical point*. To quantify the distance from the critical point it is convenient to define a dimensionless parameter t, which in the case of thermal phase transitions is given by $t = (T - T_{\rm c})/T_{\rm c}$. Although the thermodynamic average of the order parameter vanishes in the disordered phase, its fluctuations remain finite. As the critical point is approached ($t \to 0$) a remarkable behaviour is observed: the spatial and temporal correlations of the order parameter fluctuations become long-ranged and their typical length and time scales, called respectively correlation length ξ and correlation (or relaxation) time τ, diverge. The correlation length diverges usually according to a power law characterised by a *critical exponent* ν

$$\xi \propto |t|^{-\nu} \tag{2.1}$$

The relaxation time diverges as a power of the correlation length and this is described by the *dynamic critical exponent* z

$$\tau \propto \xi^z \propto |t|^{-z\nu} \tag{2.2}$$

In this picture, as we approach the critical point, the order parameter fluctuates coherently over increasing distances and ever more slowly. As a result, a series of *critical phenomena* occur. Since, at the critical point, fluctuations are present at all length and time scales, the system exhibits similar physical phenomena independently of the size or energy scale of the probe used to observe it (*scale invariance*). A classical example is the phenomenon of critical opalescence caused by the strong density fluctuations at the liquid/gas transition: at the critical point, monochromatic light of any wave length is strongly diffused [48]. Another remarkable property of continuous phase transitions, called *universality*, is the fact that the same critical exponents can characterise broad classes of phase transitions occurring in diverse physical system. The universality classes are defined only by the dimensionality of the physical system and by the symmetry of the order parameter.

2.1.2 Quantum criticality

An important consequence of the divergence of the correlation time is the following: the fluctuations of the order parameter of any finite-temperature phase transition are essentially classical and do not require a quantum statistical analysis. Since the correlation time diverges, the energy scale $\hbar/\tau$ associated with the fluctuations of the order parameter vanishes at the critical point. Therefore, for any non-zero T_c we will have $k_\mathrm{B}T_\mathrm{c} \gg \hbar/\tau$ sufficiently close to the critical point and the system will behave classically. These considerations also show that there is only one class of phase transitions in which quantum statistical mechanics will have an impact on the critical behaviour: the ones occuring at absolute zero temperature, called quantum phase transitions [49, 50, 51]. These are a special class of phase transitions in which a physical system undergoes a change in ground state by changing not the temperature, but some fundamental parameter d of its hamiltonian, such as doping, pressure, magnetic or electric field. In this scenario, the distance from the quantum critical point d_c is measured by a dimensionless parameter $\delta = (d - d_\mathrm{c})/d_\mathrm{c}$ and the divergent behaviour of the spatial and temportal correlations are described by the familiar forms

$$\xi \propto |\delta|^{-\nu} \tag{2.3}$$

$$\tau \propto \xi^z \propto |\delta|^{-z\nu} \tag{2.4}$$

Let us now consider the case of a physical system which is endowed with an order existing at finite temperatures that can also be destroyed by the variation of a non-thermal parameter. Since in the vicinity of a quantum critical point, at finite temperatures, thermal and quantum fluctuations can coexist, the system will exhibit a rich phase diagram in the (d, T) plane. Namely, we can distinguish 4 regimes (also represented in Figure 2.1):

1. Ordered: long range order is well established ($T < T_\mathrm{c}$, $d > d_\mathrm{c}$).

2. Thermally disordered: long range order is destroyed by thermal fluctuations ($T > T_\mathrm{c}$, $d > d_\mathrm{c}$). Classical criticality is observed around T_c.

3. Quantum disordered: long range order is destroyed by quantum fluctuations ($d < d_\mathrm{c}$).

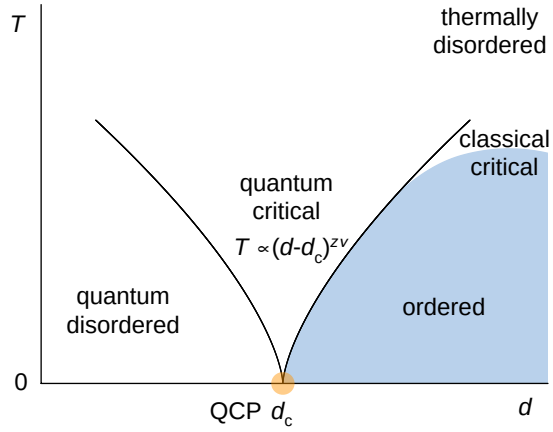

Figure 2.1: Phase diagram in the (d, T) plane in the vicinity of a quantum critical point (QCP).

4. Quantum criticality: thermal and quantum fluctuations dominate (finite temperatures, $d \simeq d_{\mathrm{c}}$).

In the quantum critical region exciting and unusual physical behaviour is often observed at finite temperatures, since both thermal and quantum fluctuations are at play. The boundaries of the quantum critical region of the phase diagram are determined by the condition

$$k_{\mathrm{B}}T > \hbar/\tau \propto |\delta|^{z\nu} \tag{2.5}$$

In this scenario, the quantum critical point can be regarded as the endpoint of a critical line $T_{\mathrm{c}}(d)$, that, in the regime of coexisting thermal and quantum fluctuations, scales as [52]

$$T_{\mathrm{c}}(d) \propto |\delta|^{z\nu} \tag{2.6}$$

2.1.3 The role of quantum statistical mechanics

So far we sketched a plausible phase diagram of a physical system whose ground state can be tuned by a non-thermal parameter. As we previously mentioned, these phase transitions are governed by quantum statistical mechanics. In this context, the thermodynamic properties of a physical system described by an Hamiltonian H, can be calculated from the partition function Z defined as ($\beta = 1/k_{\mathrm{B}}T$)

$$Z = \mathrm{Tr}\, e^{-\beta H} \tag{2.7}$$

Much insight can be gained by noting that the density matrix $e^{-\beta H}$ has the same form as the time evolution operator $e^{-iHt/\hbar}$ on condition that an imaginary value is assigned to the interval of the time evolution [50]. The trace of the density matrix calculated over a complete basis set $|n\rangle$ is given by

$$Z = \sum_n \langle n|e^{-\beta H}|n\rangle \tag{2.8}$$

This is the sum of transition amplitudes of a system that lies in a state n at time $t = 0$ and returns to the same state after an imaginary time interval $-i\hbar\beta$. According to the Feynman's formulation of quantum theory [53], each of these amplitudes can be calculated by summing the amplitudes of all possible loops in the configuration space connecting the state $|n\rangle$ with itself. The time available to a quantum state for the exploration of its neighborhood in configuration space, before coming back to its original configuration, is given by the inverse of the temperature. In other words, the statistical weight of a D dimensional quantum state is determined by the overlap of this state with its neighbors in the configuration space and by the extent $\hbar\beta$ of the time evolution. At absolute zero temperature, where the temporal dimension diverges, we can identify the statistical weight of a space time path with the Boltzmann weight of a $D + 1$ classical system.

This mapping between quantum and classical statistical mechanics is an essential tool for the understanding of quantum phase transitions. It allow us to express the partition function of a D-dimensional quantum system as the partition function of a $(D + 1)$-dimensional classical system and to apply results of classical statistical mechanics, such as calculations of the previously introduced critical exponents, to quantum systems.

2.2 The superconductor-insulator transition

We will focus our attention on a specific example of a quantum phase transition: the two-dimensional superconductor to insulator transition. The occurrence in Nature of this transition is related to some special properties of the superconducting transition in two dimensions.

2.2.1 The Berezinskii-Kosterlitz-Thouless transition

The order parameter that represents the superconducting phase is a complex quantity, characterised by an amplitude and a phase: $\Psi = |\Psi|e^{i\varphi}$. In two dimensions, a very useful representation of the properties of this order parameter is the XY model on a lattice [54]. In this model, a spin $\mathbf{s}(\mathbf{r}) = s(\cos\theta(\mathbf{r}), \sin\theta(\mathbf{r}))$ is assigned to each site $\mathbf{r}$ of a lattice and these interact with their nearest neighbors via an exchange interaction. In the ground state of this model, the spins can point uniformly anywhere in a two-dimensional plane, since spatially uniform rotations of θ do not change the energy. On the other hand, any spatial variation of θ will increase the free energy. This is described by an elastic energy F_{el}, which in the context of superfluids takes the form

$$F_{el} = \frac{1}{2} m^* n_s \int d\mathbf{r} v_s^2 \tag{2.9}$$

where m^* is the electron's effective mass; $n_s = |\Psi|^2$ and $v_s = \hbar\nabla\theta(\mathbf{r})/2m^*$ are the superfluid densitiy and velocity respectively.

It is important to immediately draw our attention to a central property of this model: the energy associated with elastic phase excitations can be arbitrarily small. The low energy excitations correspond to long wave-length modes and their presence has a profound impact on the thermodynamic properties of this model, in particular

on the mean value of the order parameter $\langle\Psi(\mathbf{r})\rangle$. Indeed it can be shown that in two dimensions, the average of the order parameter is zero at any temperature. This destruction of long-range order is caused by the thermal excitation of long wave-length modes. The absence of long-range order in two-dimensional systems with a continuous symmetry is known as the Mermin-Wagner theorem [55, 56].

At this point, the hasty reader would conclude that a superconducting state in two dimensions cannot occur and abruptly end the discussion. Fortunately, Nature is more subtle, and finds a way around this problem, making it possible to observe a wealth of fascinating phenomena in two-dimensional superconductors. We can deepen our insight on this issue by looking at the behaviour of the spatial correlation function $G(\mathbf{r}) = \langle\Psi^*(\mathbf{r})\Psi(\mathbf{0})\rangle$. It is found that in two dimensions the correlation function of the order parameter decays as a power law [54]

$$G(r) = |\Psi|^2 \left(\frac{r}{\xi}\right)^{-\eta(T)} \tag{2.10}$$

where the temperature dependent exponent is given by

$$\eta(T) = \frac{m^*}{2\pi\hbar^2 n_s} T \tag{2.11}$$

Systems with power law decay of the order parameter correlation function are called quasi-long-range-ordered, in contrast with disordered systems, where an exponential decay is observed. This phase corresponds to a situation where vortex-antivortex pairs, thermal excitations of the ground state of the XY model, are bound by a logarithmic attractive interaction. An important question is whether one can describe, using this model, a transition from a disordered high temperature phase to a quasi-long-range-ordered phase.

Berezinskii [57, 58], Kosterlitz and Thouless [59] (BKT) have investigated the possibility that thermally excited vortices can lead to a continuous phase transition in the XY model. We will sketch briefly their argument. It can be shown that the energy associated with a single free vortex in a sample of size R is given by $U = \pi n_s \hbar^2 \ln(R/\xi)/m^*$, where ξ is the vortex core radius. To compute the free energy we also nee to consider the entropy $S = k_\mathrm{B} \ln(R^2/\xi^2) = 2k_\mathrm{B} \ln(R/\xi)$ which corresponds to the number of accessible configurations for a vortex of surface $\pi\xi^2$ on a sample of size πR^2. The free energy of an XY system with a single free vortex is thus

$$F = U - TS = \left[\frac{\pi n_s \hbar^2}{m^*} - 2k_\mathrm{B}T\right] \ln(R/\xi) \tag{2.12}$$

For temperatures $T < \pi n_s \hbar^2/2m^* k_\mathrm{B}$ the free energy is minimal in the absence of free vortices. For $T > \pi n_s \hbar^2/2m^* k_\mathrm{B}$ the free energy is minimized by the generation of vortices. Therefore we can identify a critical temperature, defined as

$$T_\mathrm{BKT} = \frac{\pi\hbar^2 n_s}{2m^* k_\mathrm{B}} \tag{2.13}$$

at which the spontaneous generation of free vortices destroys the quasi long range order. This transition is accompanied by a characteristic divergence of the correlation length

$$\xi = \xi_0 \exp[2\pi/(bt^{1/2})] \tag{2.14}$$

and a universal jump in the superfluid density [60].

In principle this discussion is valid for any neutral superfluid, where vortices interact logarithmically at any distance. The first experiments reporting the observation of a BKT transition were, in fact, performed on superfluid-helium films [61, 62]. The application of these ideas to charged superfluids, such as thin superconducting films, has been debated for some time. Pearl [63] has shown that vortex pairs in superconducting films have a logarithmic interaction energy up to a characteristic distance $\lambda_\perp$, calculated in terms of the London penetration depth λ and the film thickness t

$$\lambda_\perp = \frac{\lambda^2}{t} \tag{2.15}$$

Beasley, Mooij and Orlando [64] have used this argument to show that, in two-dimensional superconductors, at the transition temperature, $\lambda_\perp$ can be of the order of centimeters and this quantity is related to T_{BKT} by the relation

$$k_{\mathrm{B}} T_{\mathrm{BKT}} = \frac{\phi_0^2}{32\pi^2}\frac{1}{\lambda_\perp} \tag{2.16}$$

They also derived a very useful expression to estimate the distance between the mean field critical temperature T_{c} and T_{BKT} (R_{S} is the sheet resistance of the sample)

$$\frac{T_{\mathrm{BKT}}}{T_{\mathrm{c}}} \simeq \left(1 + 0.173\frac{R_{\mathrm{S}}}{\hbar/e^2}\right)^{-1} \tag{2.17}$$

Signatures of BKT behaviour in superconductors are often discussed in transport experiments by looking at two distinct characteristic behaviours:

- The exponential divergence of the correlation length causes a characteristic temperature dependence of the resistance R around T_{BKT}
- The Lorentz force acting on vortices and antivortices generates a regime of nonlinear current-voltage characteristics

  $$V \propto I^{a(T)} \tag{2.18}$$

  where a is related to the superfluid density by $a(T) = 1 + bn_s(T)$ where b is a constant. The exponent is predicted to exhibit a discontinuity at T_{BKT}, jumping from 1 to 3.

2.2.2 The fermionic model

So far we have only discussed fluctuations of the phase of the superconducting order parameter. Another very important fluctuations regime, pertaining to the amplitude of the order parameter, is related to the condensation of the electrons in Cooper pairs at the critical temperature. An interesting discussion of this problem has been proposed by Finkel'stein [65, 66], who considered the enhancement of the repulsive Coulomb interaction generated by disorder using a renormalization group approach. Since this phenomenon enters naturally in competition with the electron pairing, this mechanism can explain the weakening of superconductivity with increasing resistance. In this

framework, the amplitude of the order parameter vanishes at the transition and the conduction in the non-superconducting state is fermionic. Finkel'stein obtained an expression for the renormalized critical temperature which, remarkably, is solely a function of the elastic scattering time τ_{e}

$$\frac{T_{\mathrm{c}}}{T_{\mathrm{c\,max}}} = e^{\gamma}\left(\frac{1/\gamma - \sqrt{r/2} + r/4}{1/\gamma + \sqrt{r/2} + r/4}\right)^{1/\sqrt{2r}} \tag{2.19}$$

with $r = R_{\mathrm{S}}e^2/2\pi^2\hbar$ and $\gamma = \ln \hbar/k_{\mathrm{B}}T_{\mathrm{c}}\tau_{\mathrm{e}}$.

Since T_{c} and T_{BKT} can be a priori different, a very interesting scenario opens up: the amplitude of the order parameter can remain finite, while the quasi long range order can be destroyed by the proliferation of free vortices driven by a non-thermal parameter such as disorder or magnetic fields.

2.2.3 The dirty boson model

In a series of seminal papers in 1990, M.P.A. Fisher and collaborators considered a two-dimensional superconductor in the presence of disorder [67, 68]. They observed that, in a system undergoing a BKT transition, a very special scenario can come about. As the disorder is increased, both T_{c} and T_{BKT} are typically suppressed by a gradual enhancement of the Coulomb interaction. It is then possible that, at a critical level of disorder d_c, T_{BKT} vanishes while T_{c} remains finite: the ground state of the system is not superconducting, even if the electrons are still condensed in Cooper pairs. This quantum phase transition can still be described in terms of vortex unbinding, as in the BKT transition, with one important difference: the creation of free vortices cannot be described as a thermal excitation but require a full quantum mechanical analysis. In this framework vortices are bosonic particles just like Cooper pairs. The authors highlighted a fascinating duality of these particles at the superconductor-insulator transition: in the superconducting phase, vortices are localized bosons while Cooper pairs form a condensate. In the insulating phase, Cooper pairs are localized and unbound vortex-antivortex pairs form a Bose condensate. At the heart of this transition lies one of the most fundamental properties of quantum mechanics: since the phase and particles number are conjugate operators, their fluctuations are limited by the Heisenberg uncertainty principle. Consequently, bosons can either be in an eigenstate of particles number (a localized insulator) or phase (a condensate). Near the critical disorder there is a direct competition between the condensation of Cooper pairs and vortices. In the presence of a perpendicular magnetic field a similar quantum phase transition is predicted, between a superconducting vortex glass state and an insulating Bose condensate of vortices. The resulting phase diagram is shown in Figure 2.2.

A remarkable prediction of this theory is that, at the critical point, a two dimensional disordered film has a *universal* metallic sheet resistance given by the quantum of resistance for Cooper pairs

$$R_{\mathrm{Q}} = \frac{h}{4e^2} \simeq 6.45\,\mathrm{k}\Omega/\square \tag{2.20}$$

The authors of this work emphasized this result as an exception to the general statement of Abrahams, Anderson, Licciardello and Ramakrishnan ("Absence of Quantum

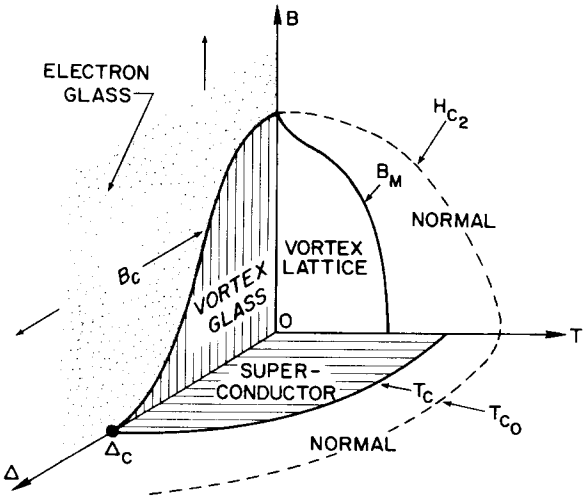

Figure 2.2: Electronic phase diagram of a two-dimensional disordered superconductor. Distinct superconductor-insulator quantum phase transitions can occur at a critical disorder and at a critical magnetic field. From [68]

Diffusion in Two Dimensions" [69], discussed in Chapter 3), by calling their paper "Presence of Quantum Diffusion in Two Dimensions....". This model sets also a lower limit for the value of the critical exponent which describes the divergence of the correlation length at the critical point. The prediction is $\nu \geqslant 2/d = 1$ [68]. The authors also argued that the dynamic exponent z is exactly 1 [67].

Evidence in favor of the universality of the resistance at the critical point came from a famous experiment performed by A. M. Goldman and collaborators who studied the superconductor-insulator transition in bismuth thin films. In this experiment, the strength of the disorder was controlled by varying the thickness of the films [70]. As we can appreciate from Fig. 2.3, the samples they studied were either superconducting or insulating, depending on the thickness and, at the transition between the two ground states, the resistance falls exactly were the theory predicts. The large body of experimental work that followed did not fully confirm the predictions of the bosonic model [71]. The superconductor-insulator transition has been studied in ultrathin films of different superconducting materials, using as control parameters magnetic and electric fields, thickness and carrier concentration. After twenty years of research there is a wide consensus among the community that the critical resistance is not universal. Diverse critical exponents have also been observed. This should not come as a surprise since this universality rests upon an exact duality between vortices and Cooper pairs. This in turn requires a logarithmic interaction between Cooper pairs, which is difficult to justify. Another limitation of this model is that it completely neglects amplitude fluctuations, that is the disappearance of Cooper pairs at the transition.

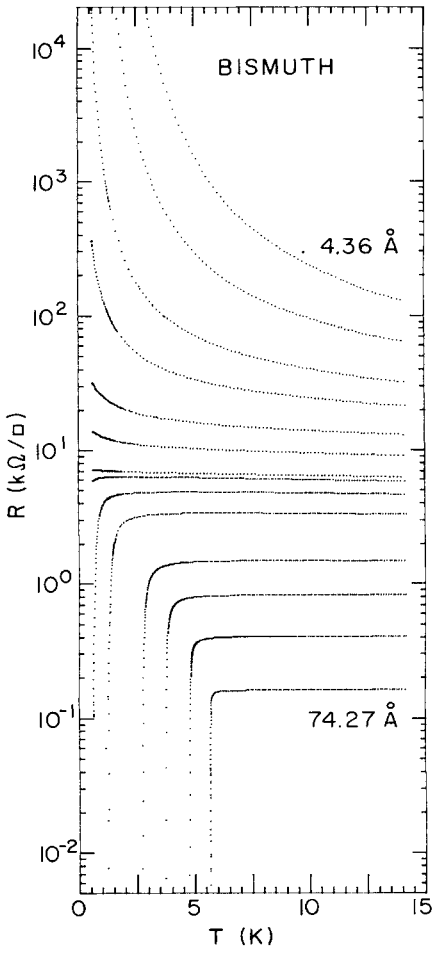

Figure 2.3: Sheet resistance as a function of temperature of thin films of bismuth characterised by a different thickness. From [70]

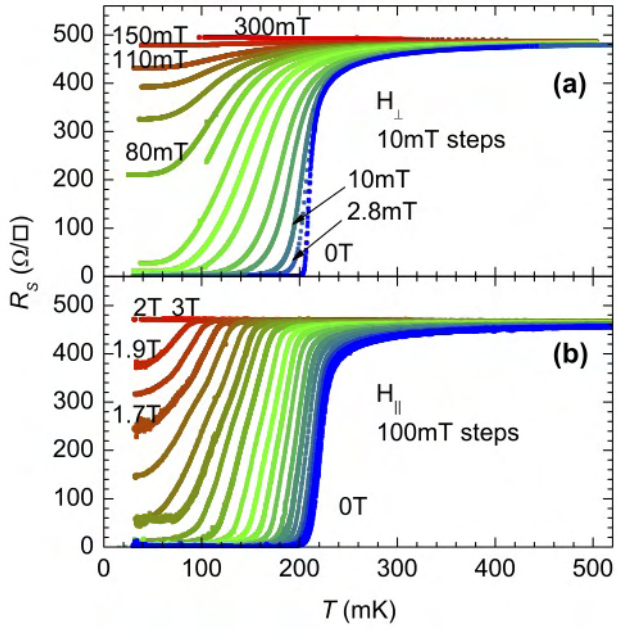

Figure 2.4: Sheet resistance vs temperature for different magnetic fields applied perpendicular and parallel to the $LaAlO_3/SrTiO_3$ interface.

2.3 Electrostatic tuning of superconductivity in $LaAlO_3/SrTiO_3$ interfaces

We will now discuss a series of transport experiments performed on $LaAlO_3/SrTiO_3$ heterostructures. First we will discuss the two-dimensional character of superconductivity in these structures and, consequently, we will consider their superconducting transitions in the BKT framework. Having established this, we will present evidence of a superconductor-insulator quantum phase transition guided by the electrostatic field effect.

2.3.1 Two-dimensional superconductivity

The dimensionality of the superconducting state in $LaAlO_3/SrTiO_3$ heterostructures can be assessed by investigating their transport properties under applied magnetic fields. Figure 2.4 shows sheet resistance R_S vs temperature measurements for magnetic fields applied perpendicular ($H_\perp$) and parallel ($H_{||}$) to the interface. The sample shown here has a $LaAlO_3$ thickness of 4 uc. The resistance was measured by a dc four-point method, in a dilution cryostat, along a transport path that was 100 μm wide and 200 μm long. In the parallel configuration, the current direction is collinear with the magnetic field and the alignment between the interface and the field is adjusted with a precision of about 0.15 deg using a piezoelectric goniometer. The measurement current has been kept below the critical current determined from voltage versus current characteristics recorded at different temperatures and magnetic fields.

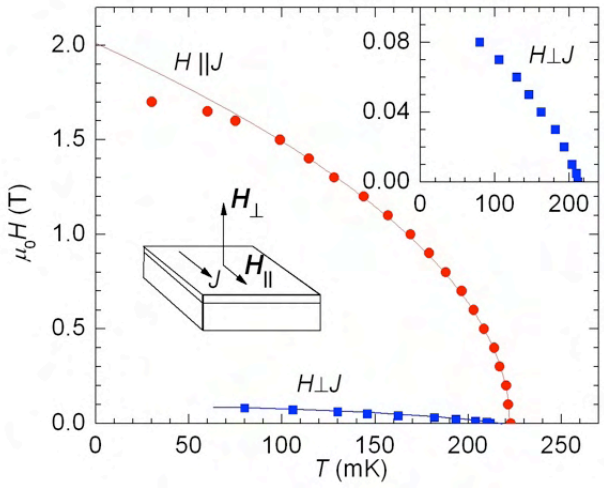

Figure 2.5: Characteristic magnetic fields as a function of the temperature for H applied parallel (dots) and perpendicular (squares) to the $LaAlO_3/SrTiO_3$ interface, exhibiting a large anisotropy. The inset shows the same data on an enlarged field scale for the perpendicular field configuration. The solid line is a fit of the data for the parallel fields.

To determine the dimensionality of the superconducting layer we define T^* as the temperature at which the sheet resistance is 50% of $R_S(T = 400\,\text{mK})$. Figure 2.5 shows the characteristic fields $\mu_0 H^*(T)$ for the parallel and perpendicular field directions. The analysis of the perpendicular field data lead to an in-plane coherence length

$$\xi_\parallel = \left[\frac{\phi_0}{2\pi\mu_0 H_\perp^*}\right]^{1/2} \tag{2.21}$$

of about 70 nm at $T = 0$. According to the Ginzburg-Landau theory, a superconducting film in the two-dimensional limit, that is thinner than the in-plane coherence length, presents a square-root dependence of the characteristic parallel field as a function of temperature

$$H_\parallel^* \propto \left[1 - \frac{T}{T^*(H=0)}\right]^{1/2} \tag{2.22}$$

We note from Figure 2.5 that the behaviour observed in $LaAlO_3/SrTiO_3$ interfaces is in remarkable agreement with this prediction, suggesting a two-dimensional superconducting state. In the same framework, the thickness t of the superconducting layer can be estimated using the relation

$$t = \frac{\sqrt{3}\phi_0}{\pi\xi_\parallel(T)\mu_0 H_\parallel^*(T)} \tag{2.23}$$

which leads to a T-independent estimate $t = 12 \pm 2\,\text{nm}$. This value is much smaller than the in-plane coherence length, verifying the internal consistency of our analysis. This estimate of the thickness of the electron gas is also consistent with other experimental results reported in the literature and discussed in Chapter 1.

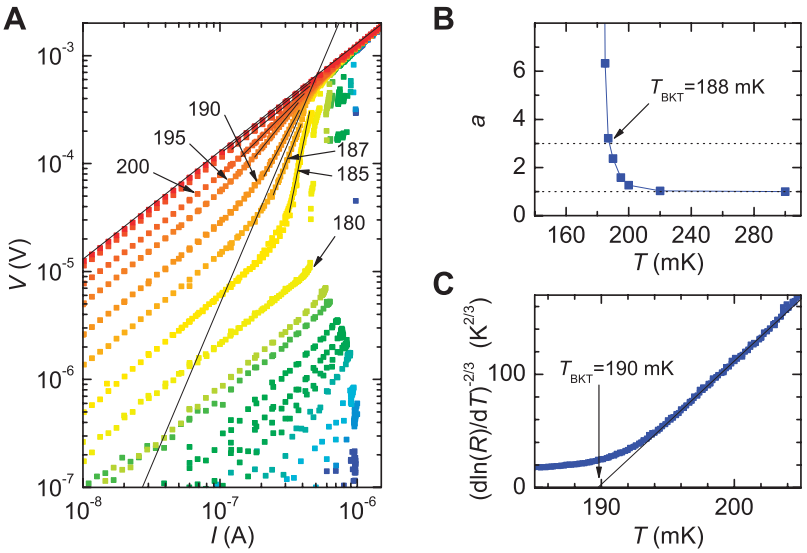

Figure 2.6: Low-temperature transport properties of the 8 u.c. $LaAlO_3/SrTiO_3$ heterostructure. (A) $V(I)$ curves on a logarithmic scale. The numbers provide the value of T, measured in mK, at which the curves were taken. The short black lines are fits of the data in the transition. The two long black lines correspond to $V = RI$ and $V \sim I^3$ dependencies and show that 187 mK$< T_{\mathrm{BKT}} <$190 mK. (B) Temperature dependence of the power-law exponent a, as deduced from the fits shown in (A). (C) $R(T)$ dependence of the 8 u.c. sample ($I = 100$ nA), plotted on a $[d\ln(R)/dT]^{2/3}$ scale. The solid line is the behavior expected for a BKT transition with $T_{\mathrm{BKT}} = 190$ mK.

Since this system is two-dimensional we can analyse its superconducting transition using the BKT approach. A simple estimate using the Beasley formula (equation 2.17) would suggest that in $LaAlO_3/SrTiO_3$ interfaces, the BKT and mean field temperatures almost coincide. However, in the case of large vortex fugacity, a high density of vortex-antivortex pairs is thermally generated and the formation of an ionic-like vortex-antivortex crystal is predicted [72]. For such a system, the melting of this lattice represents the BKT transition, which then occurs at lower temperatures. At the BKT transition, the current-induced Lorentz force causes dislocation-antidislocation pairs to unbind, resulting in the $V \propto I^{a(T)}$ behavior, with $a(T_{\mathrm{BKT}}) = 3$, introduced in section 2.2.1. Figure 2.6A,B shows the $V(I)$ characteristics of a 8 u.c. $LaAlO_3$ sample, recorded at different temperatures. The interface exhibits a clear $V \propto I^{a(T)}$ dependence, providing evidence of BKT behaviour and an estimate $T_{\mathrm{BKT}} \simeq 188\,\mathrm{mK}$.

A piece of experimental evidence that particularly favors the model of the vortex-antivortex crystal is the excellent estimate that this provides of the critical current. Further evidence for dissociation of vortices at the superconducting transition can be obtained from the analysis of the $R(T)$ measurements, since the exponential divergence of the correlation length causes a characteristic temperature dependence of the resistance. The best way to proceed with this analysis is still debated and we will discuss two different approaches presented in the literature. The first, proposed by T. Schneider [73], is based on the behaviour of the correlation length near T_{BKT} outlined in equation 2.14. Since the resistance is proportional to the density of unbound vortices we expect to observe $R \propto \xi^{-2}$. Therefore the resistance as a function of temperature should obey the law

$$R = R_0 \exp\left(-\frac{b_R}{(T - T_{\mathrm{BKT}})^{1/2}}\right) \tag{2.24}$$

where b_R is a parameter related to the vortex properties. We can rewrite this expression as

$$\left(\frac{d \ln R}{dT}\right)^{-2/3} = \left(\frac{2}{b_R}\right)^{2/3} (T - T_{\mathrm{BKT}}) \tag{2.25}$$

This form has the advantage that b_R and T_{BKT} can be estimated from a characteristic linear behaviour above T_{BKT}, while R_0 is eliminated. The result of this analysis is depicted in Figure 2.6C where the linear region enables an estimate $T_{\mathrm{BKT}} \simeq 190\,\mathrm{mK}$ which is in good agreement with the value extracted from the I, V characteristics. This analysis relies on the assumption that T_{c} is far larger than T_{BKT} and the region of linear behaviour can be described solely by the BKT theory. Benfatto and collaborators have challenged this point of view, and have proposed an interesting alternative approach [74]. They suggested that the superconducting transition should cross over from a regime of Ginzburg-Landau fluctuations, characterised by a power law divergence of the correlation length, to a BKT regime where the divergence acquires an exponential form. Accordingly they analysed the experimental data with a formula interpolating the two regimes obtaining a very good fit over a wide temperature range (see Figure 2.7). It is interesting to remark that both analyses are unable to capture the behaviour of the resistance at the lowest temperatures. In the case of the first approach, a clear deviation from the linear behaviour is observed. In the second analysis the resistive tail of the transition could not be fitted without including a gaussian distribution of the superfluid density. Both authors pointed to inhomogeneities and finite size effects as

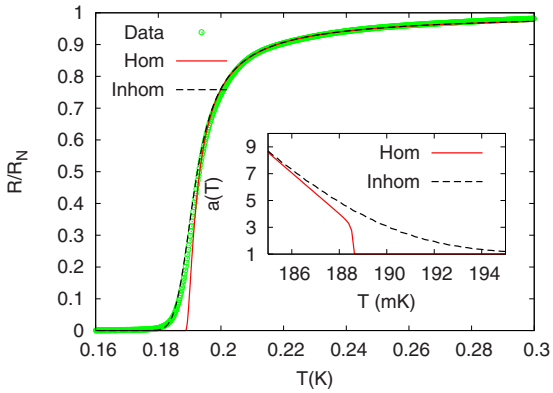

Figure 2.7: Fit of the normalised resistivity as a function of temperature using the approach proposed by Benfatto and collaborators. The curve labeled Hom refers to the case of a single value of superfluid density while the curve Inhom refers to the resistivity obtained by sample average over a distribution of superfluid density. Inset: coefficient a of the I-V characteristic in the two cases. From [74]

responsible for this behaviour. The most notable difference between the two methods is related to the values of the b_R parameter of equation 2.14 that are extracted. The first procedure leads to b_R values which are one order of magnitude smaller than the second. This could be interpreted as another signature of the vortex crystal, which could renormalise the parameter b_R or could signal an inconsistency in the analysis. Since a theoretical calculation of this parameter in the context of the fusion of a vortex crystal is lacking, this issue cannot be resolved at the moment. Despite their differences, both analyses point to a BKT behaviour of the superconducting transition of the $LaAlO_3/SrTiO_3$ interface, which is the main point of our discussion.

2.3.2 Field effect experiments

After having demonstrated the important role played by phase fluctuations in the temperature driven superconducting transition at the $LaAlO_3/SrTiO_3$ interface, we are prepared to discuss the tuning of the ground state of this system by an external parameter. We will mainly discuss quantum phase transitions driven by the electric field effect but we will also present data related to the suppression of superconductivity by a magnetic field.

The application of the field-effect transistor principle to novel electronic systems provides a fascinating opportunity to control their properties and ultimately their ground state [75, 76]. This technique has been applied with success to a variety of exotic materials, such as high-temperature superconductors [77, 78, 79, 80], amorphous superconductors [81], ferromagnetic manganites [82, 83] and organic materials [84]. Since the electrostatic field effect is essentially an interface phenomenon, we can expect particularly interesting results in the $LaAlO_3/SrTiO_3$ system.

In a standard field effect device, an electric field is applied between a metallic gate and a conducting channel across a dielectric. The 0.5 mm thick $SrTiO_3$ substrate was

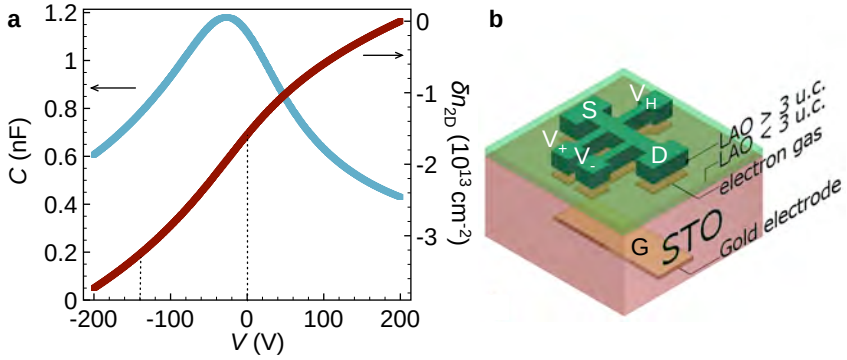

Figure 2.8: Dielectric characterisation of the field effect device. (a) Dielectric tunability of the differential capacitance (C versus V) measured on a device at 1.5 K (blue). $C(V)$ is measured with an ac technique applying a dV = 1 V. Change in the 2D carrier concentration as a function of gate voltage calculated using eq. 2.26 with $V_1 = 200$ V and $V_2 = V$ (red). The dashed lines indicate the region where the quantum critical behaviour is observed. Note that in this region $\delta n_{2D} \sim \delta V$. (b) Schematic view of a field effect device, showing the source (S), drain (D), longitudinal voltage (V_+ and V_-), Hall voltage (V_H) and gate voltage (G) contacts.

used as the dielectric since it is characterised at low temperatures by a large dielectric constant. The metallic gate is a gold film sputtered opposite to the channel area onto the backside of the substrate. In this configuration the electric field modulates the concentration of carriers in the interface conducting channel. A sketch of the field effect device is shown in Figure 2.8b.

To quantify the carrier density modulation resulting from the field effect, the electric field dependence of the $SrTiO_3$ permeability needs to be taken into account [85]. We therefore measured the differential capacitance $C(V) = \mathrm{d}Q(V)/\mathrm{d}V$ of the device as a function of the applied gate voltage V, $Q(V)$ being the induced charge. It is known that charge trapping in $SrTiO_3$ can occur and may cause the appearance of hysteresis in the $C(V)$ measurements [86]. Indeed the capacitance was found to depend on the voltage sweep history. However, the devices present reversible and reproducible $C(V)$ characteristics when the field is first ramped to the highest positive voltage. Following this experimental procedure, the field induced modulation of charge density δn_{2D} between gate voltages V_1 and V_2 can be evaluated using the relation

$$\delta n_{2\mathrm{D}} = \frac{1}{Se} \int_{V_1}^{V_2} C(V)\mathrm{d}V \tag{2.26}$$

where S is the area of the gate electrode and e is the elementary charge. The $C(V)$ characteristic of a 9 u.c. device and the corresponding modulation of carrier density are presented in Figure 2.8a. The carrier concentration of the as-grown sample has been measured using the Hall effect ($n_{2\mathrm{D}} \simeq 4.5 \cdot 10^{13}\,\mathrm{cm}^{-2}$ at 100 K). The maximum modulation of the carrier density that was achieved is remarkably close to the total number of free carriers present in the system, indicating that the electric field effect is an excellent tool to probe its phase diagram.

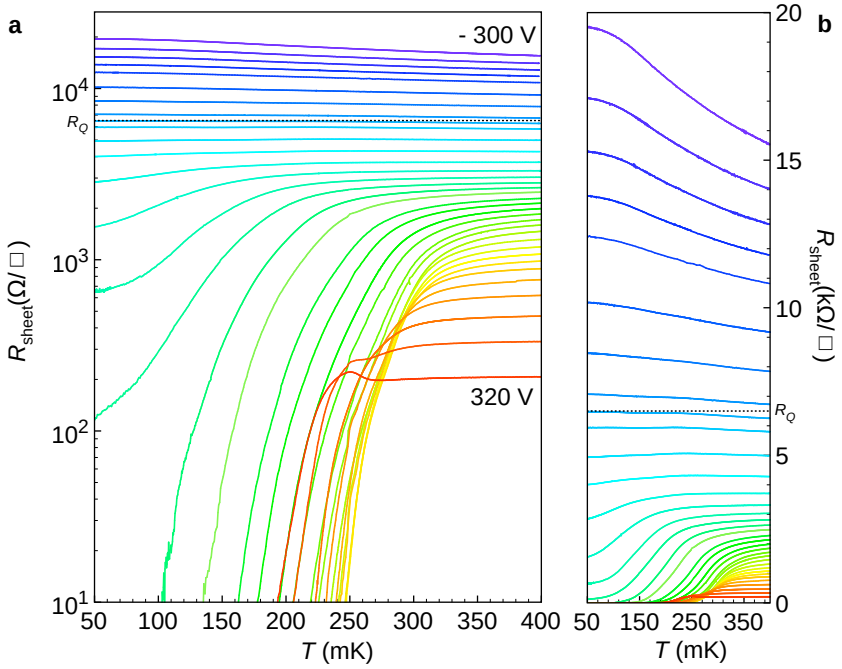

Figure 2.9: Field effect modulation of the transport properties. (a) Measured sheet resistance as a function of temperature for gate voltages varying in 10 V steps between -300 V and -260 V, 20 V steps between -260 V and 320 V and for -190 V, plotted on a semi-logarithmic scale. (b) The same data plotted on a linear resistance scale.

On the same sample the temperature dependence of the sheet resistance R_{sheet} has been measured for various gate voltages V. Figure 2.9a shows the sheet resistance versus temperature for applied gate voltages between -300 V and 320 V; Figure 2.9b displays the same data on a linear sheet resistance scale. This behaviour has been observed in several samples. A variation of the gate voltage induces a large modulation of the normal state resistance, which changes by two orders of magnitude, and a remarkable tuning of the superconducting critical temperature. For large negative voltages, corresponding to the smallest accessible electron densities, the sheet resistance increases as the temperature is decreased, suggesting an insulating (conductance $G \to 0$ as $T \to 0$) ground state. As the electron density is increased the system becomes a superconductor. The superconducting to insulating ground state transition occurs at a critical sheet resistance $R_c \approx 4.5\,\text{k}\Omega/\square$, close to the quantum of resistance for charge $2e$ bosons predicted by Fisher's theory. A further increase in the electron density produces first a rise of the critical temperature to a maximum of $\sim 310\,\text{mK}$. For larger voltages, the critical temperature decreases again, providing evidence for an overdoped regime. These measurements thus reveal the existence of a quantum phase transition between a superconducting and an insulating phase at the $LaAlO_3/SrTiO_3$ interface and demonstrate that the ground state of the system depends on its carrier density. The interpretation of this phenomenon in term of quantum phase transition is further substantiate by the observation of a well defined crossing point in the isotherms $R(V)$ presented in Figure 2.10 which enables us to identify a critical voltage and re-

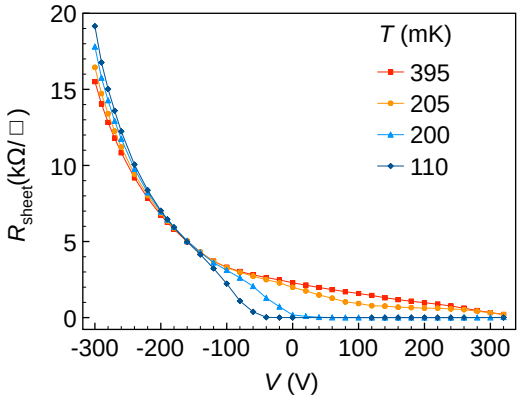

Figure 2.10: Sheet resistance as a function of gate voltage V measured at different temperatures. The curves exhibit a well defined crossing point, characteristic of a superconductor-insulator transition.

sistance.

Close to the critical point, the sheet resistance measured at 400 mK shows a remarkable phenomenon. As can be seen in Figure 2.11, approaching the critical point from the superconducting region of the phase diagram, a linear dependence of the sheet resistance as a function of the applied voltage is observed. Once the critical point has been crossed, however, a further reduction of carrier concentration produces a much steeper variation of resistance.

In order to establish the critical temperature versus carrier density phase diagram, a criterion to define the critical temperature for each gate voltage is needed. We used the first method described in section 2.3.1 to extract T_{BKT} for each applied gate voltage and to map out the phase diagram. The result is shown in Figure 2.11. Reducing the carrier concentration from the largest doping level ($V = 320$ V), T_{BKT} first increases, reaches a maximum at around 310 mK and then decreases to zero. This critical line ends at $V_{\mathrm{c}} \simeq -140$ V, where the system undergoes a QPT.

To investigate the quantum critical region in detail we consider a continuous QPT separating a superconducting ground state and an insulating ground state. The control parameter of the phase transition is the variation of the carrier concentration $\delta n_{\mathrm{2D}} = n_{\mathrm{2D}} - n_{\mathrm{2Dc}}$, where n_{2Dc} is the sheet carrier density at the critical point. Figure 2.8a shows a quasi-linear relationship between the applied gate voltage and the variation of carrier concentration $\delta n_{\mathrm{2D}} \propto \delta V = V - V_{\mathrm{c}}$ in the vicinity of the critical point. Hence we can use the gate voltage as the tuning parameter for the analysis of the QPT. For a continuous QPT, the quantum critical region is characterised by a spatial and a temporal correlation length that diverge respectively as $\xi \propto (\delta n_{\mathrm{2D}})^{-\nu}$, and $\xi_\tau \propto (\delta n_{\mathrm{2D}})^{-z\nu}$. As previously discussed, according to the scaling theory of quantum critical phenomena [52, 87, 88] the phase transition line $T_{\mathrm{BKT}}(\delta V)$ presented in Fig. 2.11 is expected to scale (see equation 2.6), in the vicinity of the quantum critical point (QCP), as

$$T_{\mathrm{BKT}} \propto (\delta n_{\mathrm{2D}})^{z\nu} \propto (\delta V)^{z\nu} \tag{2.27}$$

In Fig. 2.11 we observe that the approach to quantum criticality is well described by

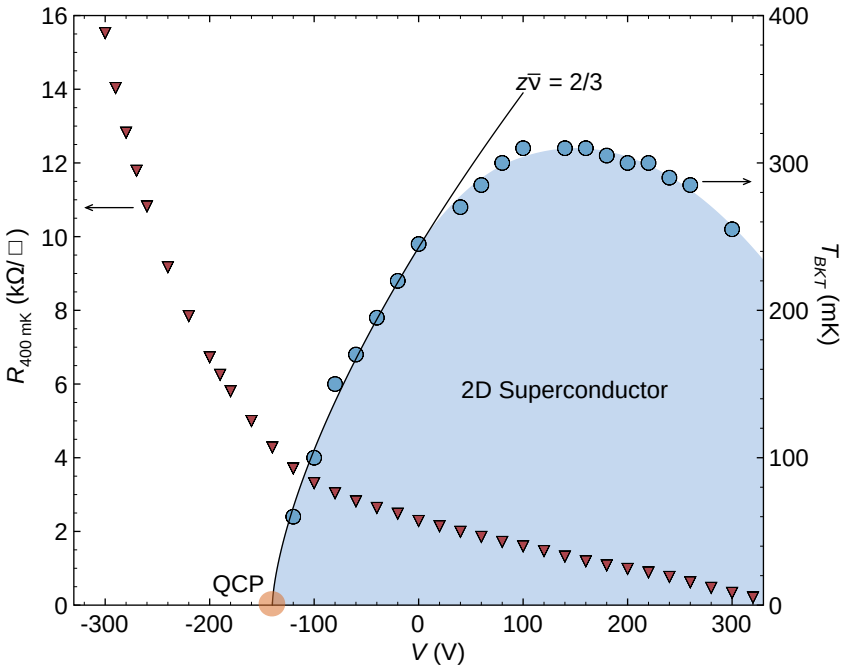

Figure 2.11: Electronic phase diagram of the $LaAlO_3/SrTiO_3$ interface. Critical temperature T_{BKT} (right axis, blue dots) versus gate voltage, revealing the superconducting region of the phase diagram. The solid line describes the approach to the quantum critical point using the scaling relation $T_{\mathrm{BKT}} \propto (V - V_c)^{z\nu}$, with $z\nu = 2/3$. Normal state resistance, measured at 400 mK (left axis, red triangles) as a function of gate voltage.

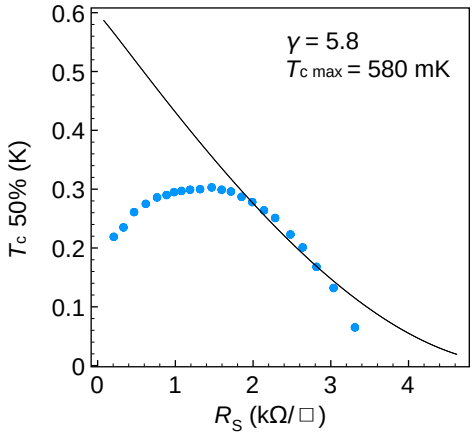

Figure 2.12: Critical temperature T_c of the $LaAlO_3/SrTiO_3$ interface as a function of the sheet resistance R_S. The solid line is the best fit to Finkel'stein theory.

$z\nu = 2/3$. We note that the product $z\nu = 2/3$ agrees with the results obtained in previous experiments of electric and magnetic field tuned 2D-QSI transition in amorphous bismuth films [81] and $Nb_{0.15}Si_{0.85}$ films [89]. The value $z\nu = 2/3$ is compatible with the 3D-XY model possibly indicative of a clean (or weakly disordered) system in which quantum fluctuations dominate ((2+1)D-XY). The voltage range over which quantum critical fluctuations can be observed has however to be determined. The product $z\nu = 2/3$ is not compatible with the dirty boson model, which predicts $z\nu \geqslant 1$.

It is interesting also to look at the data in a purely fermionic perspective, using the approach of Finkel'stein described in Section 2.2.2. Using this model we can interpret the dependence of the critical temperature on the sheet resistance in term of reinforcement of the repulsive Coulomb interaction caused by the disorder. The best fit of equation 2.19 to our experimental data is presented in Figure 2.12. In this analysis we estimated T_c as the temperature at which the sheet resistance is 50% of $R_S(T = 400\,\text{mK})$. To obtain a fit of the theory to our data we had to take the maximum mean field critical temperature $T_{c\,\max}$, as a free parameter larger than the observed maximum critical temperature. We obtain $T_{c\,\max} = 580\,\text{mK}$ which is of the same order of the largest critical temperatures observed in bulk $SrTiO_3$. From the parameter γ we can estimate an elastic scattering time, at $T_{c\,\max}$, $\tau \simeq 37\,\text{fs}$ which is in line with the observed resistivity. Overall, a fully fermionic model appears to deliver an inadequate interpretation of our experimental results. It not only completely misses the behaviour at low resistivity, where an overdoped regime is observed, but it also fails to appropriately describe the high resistance regime, where a much faster weakening of superconductivity than the one predicted is present. On the basis of this finding and on the consistency observed with the XY model we can conclude that phase fluctuations play an important role in this system.

The transition from a superconducting to an insulating state can also be driven by a magnetic field. Indeed this control parameter is the most widely used to drive superconductor to insulator transitions in thin films such as α-InO_x [90], MoGe [91, 92] and TiN [93]. In this case the hallmark of this transition is the crossing at a well defined

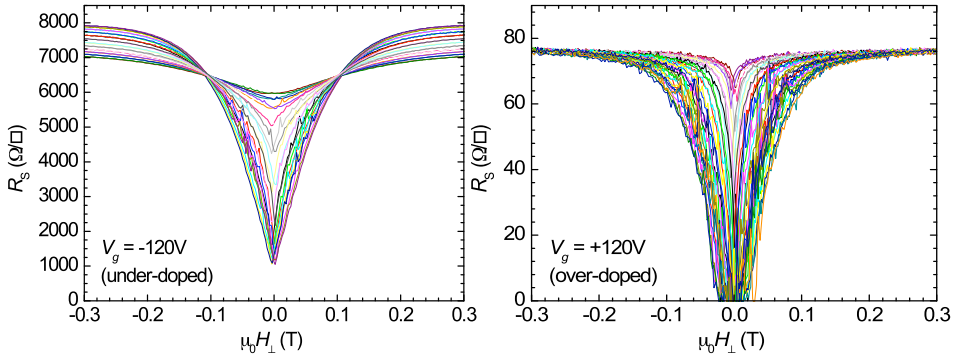

Figure 2.13: Sheet resistance R_S of the $LaAlO_3/SrTiO_3$ interface as a function of magnetic field, -120 V (left panel) and 120 V (right panel), for different temperatures (50 to 800 mK).

point of the resistance versus magnetic field curves recorded at different temperatures. As shown in Figure 2.13, in $LaAlO_3/SrTiO_3$ interfaces for gate voltages close to the quantum critical point, we observe a crossing point situated around 100 mT. We remark that the critical sheet resistance at the crossing point ($R_c \approx 6.5\,\mathrm{k}\Omega/\square$) is exactly the one predicted by the bosonic theory. On the same sample in the overdoped regime no crossing point is observed in the resistance versus magnetic field measurements, which indicates that on this side of the dome a superconductor to metal transition is present.

Of particular relevance for the understanding of the nature of this electronic system is the insulating region of the phase diagram. In the accessible temperature range the variation of the conductance can be explained by weak localisation [94]. The nature of the phenomenon will be discussed extensively in the next Chapter. Fig. 2.14a depicts the dependence of the sheet resistance in a perpendicular magnetic field measured at 30 mK. As expected if weak localisation is governing the magnetotransport properties, we observe a large negative magnetoresistance that increases as we move more deeply into the insulating phase, reaching more than -40% at 8 T for the lowest measured carrier concentration. Above $\sim$1 T the resistance decreases logarithmically with increasing magnetic field.

Is the observation of weak localisation consistent with the presence of bosonic excitations in the insulating regime? This is a relevant question, since weak localisation corrections normally arise in the context of fermions. Das and Doniach considered the problem of weakly localised bosons [94], stimulated by the experimental findings of Yazdani and Kapitulnik, that showed weak localisation occurring on the insulating side of the superconductor-insulator transition in Mo-Ge thin films [92]. They argued that the weak localization of bosons is characterized by $R_s \sim \ln(1/T)$, as compared to $\sigma \sim \ln T$ for fermions. These two theoretical prediction are compared with the same experimental data ($LaAlO_3/SrTiO_3$ interface at -240 V) in Figure 2.15. As the reader can appreciate, it is hard to discriminate between the two scenarios based on the available experimental evidence. In both cases the logarithmic behaviour is limited to the same temperature range and a deviation is observed at the

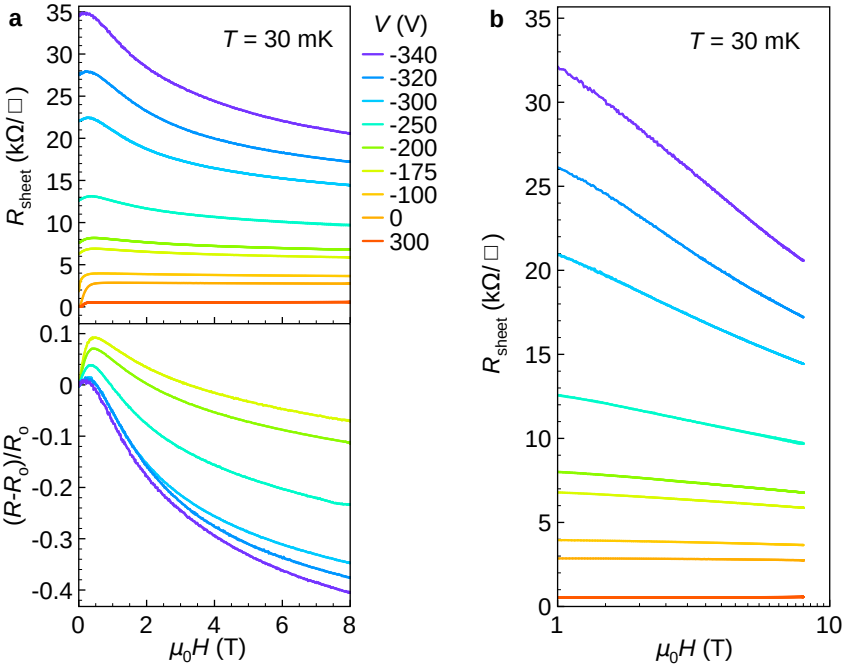

Figure 2.14: Field effect modulation of the magnetotransport properties. (a) Sheet resistance (top panel) and magnetoresistance (bottom panel), as a function of magnetic field, measured for different gate voltages at 30 mK. Note the large negative magnetoresistance for the lowest carrier densities.(b) Sheet resistance as a function of magnetic field, measured for different gate voltages at 30 mK and plotted on a logarithmic magnetic field scale.

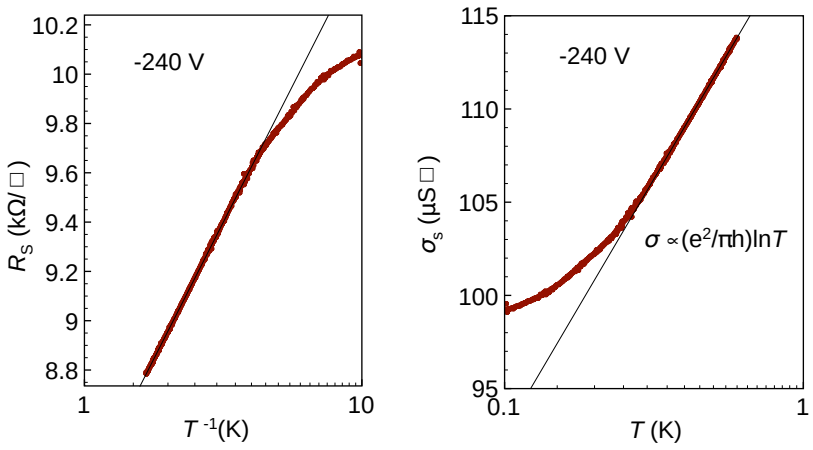

Figure 2.15: Comparison of the predictions for the weak localisation of bosons (left panel) and fermions (right panel), on the same experimental data.

lowest temperatures. We remark that the theoretical prediction for the weak localisation of fermions is much stronger, since a universal prefactor of the $R_s \sim \ln(1/T)$ law, given by $e^2/\pi h \simeq 1.2 \cdot 10^{-5}$ S, is expected. This universal behaviour is observed in our experiments, and the same prefactor describes the logarithmic decrease of the conductance in magnetic field as well.

The picture that emerges from this study of the superconductor-insulator transition in $LaAlO_3/SrTiO_3$ interfaces is not conclusive. On one hand we find some experimental evidence in favor of the bosonic scenario, such as the value of the resistance at the quantum critical point and the observation of well defined crossing points of the isothermal resistance curves as a function of both gate voltage and magnetic field. Moreover, the weakening of the critical temperature cannot solely be explained by a reinforcement of the Coulomb interaction. All these elements point to the important role played by phase fluctuations in this quantum phase transition. On the other hand the product of critical exponents $z\nu = 2/3$, characteristic of a clean XY model, is not compatible with the dirty boson model, which predicts $z\nu \geqslant 1$. We remark that the same apparent inconsistency has emerged in studies of the superconductor-insulator transition in amorphous bismuth [95]. Further experimental work will help us to shed light on the issue.

Chapter 3

Localisation and spin-orbit interaction

In the preceding chapter we have discussed a series of experiments where the phase diagram of the $LaAlO_3/SrTiO_3$ interface has been explored. We have uncovered a quantum phase transition that drives this system from being a superconductor to having its carriers localised. In this chapter we will attempt to describe the physical mechanisms leading to carrier localisation, and the important role that the spin-orbit interaction plays in this context. In our analysis, magnetic scattering will be neglected. We will then apply these ideas to the study of magnetotransport across the phase diagram of the $LaAlO_3/SrTiO_3$ interface. As a first step, it is best to put our discussion on solid ground by defining what we mean by "strong" or "weak" disorder.

3.1 Measuring disorder

Let us consider the ground state of a disordered quantum system of finite size L and dimensionality d, characterised by a density of state per unit volume ν and a diffusion coefficient D. This system has two natural energy scales: one is the Thouless energy, which is the energy scale $E_{\mathrm{T}} = h/\tau_L$ associated with the diffusion time of an electron along the finite size of the system $\tau_L = L^2/D$. The second is the mean spacing between its energy levels $\delta = 1/\nu L^d$. Thouless has shown that the ratio of these two energy scales

$$g = E_{\mathrm{T}}/\delta \tag{3.1}$$

determines if the electronic states of this system are localised or extended. Whenever $g \ll 1$ the energy scale associated with the finite size of the system is larger than the energy spacing and the electrons are localised. In the limit $g \gg 1$ the energy levels of the system are strongly coupled and the electrons delocalise. This parameter, known as the Thouless number, has the outstanding property of being directly related to the conductance. Indeed, if we consider Ohm's law, which states that the conductance G of a sample of side L scales as

$$G = \sigma L^{d-2} \tag{3.2}$$

and the Einstein relation for the Drude conductivity

$$\sigma = e^2 D\nu \tag{3.3}$$

we immediately see that

$$G = \frac{e^2}{h}\nu L^d \frac{hD}{L^2} = \frac{e^2}{h}g(L) \tag{3.4}$$

Therefore the *conductance* (expressed in units of e^2/h) is a direct measurement of the parameter relevant to localisation and defines the limits of weak ($g \gg 1$) and strong ($g \ll 1$) disorder. In $d = 2$, where we have $G = \frac{e^2}{h}k_{\mathrm{F}}l$, l elastic mean free path, these two limits have a very direct interpretation: they indicate whether or not the electronic wave function can oscillate between collisions.

3.2 Conductivity in the quantum many-body formalism

We will begin by considering the limit of weak disorder, where a perturbative analysis gives meaningful information. The surprising result that awaits us is that, even in the limit $g \gg 1$, quantum corrections to the conductivity generated by the disorder (called weak localisation and weak antilocalisation) play an important role, especially in $d = 2$, where they can drive a metal to insulator transition. The most appropriate way to tackle this problem is to use the language of many-body physics, which is quite abstract and difficult to digest, but is able to capture the most subtle effects related to the wave nature of the electrons. We will begin by briefly illustrating how we can calculate the conductivity in this framework. Without dwelling on the details, this introduction is intended to provide an overview of the physical processes responsible for these quantum corrections. The discussion is based on Ref. [96], where the details of the calculations can be found.

3.2.1 Kubo formula

The conductivity tensor $\sigma_{\mu\nu}$ characterises the linear response of a physical system to the application of an electric field E_ν, in the form of a generated current j_ν. This is expressed in a general non-local form

$$e\langle j_\mu(\mathbf{r},t)\rangle_V = \sum_\nu \int d\mathbf{r}'dt'\sigma_{\mu\nu}(\mathbf{r},\mathbf{r}',t-t')E_\nu(\mathbf{r}',t') \tag{3.5}$$

The symbol $\langle ...\rangle_V$ indicates a thermodynamic average in the presence of the perturbation $V = \int j(\mathbf{r})\cdot(-e)\mathbf{A}(\mathbf{r})d\mathbf{r}$, which describes the coupling of the electromagnetic field (represented by the vector potential $\mathbf{A}$) with a current. In quantum mechanics the current operator is defined as

$$\mathbf{j}(\mathbf{r}) = \mathbf{j}^{\mathbf{p}}(\mathbf{r}) + \mathbf{j}^{\mathbf{d}}(\mathbf{r}) \tag{3.6}$$

$$\mathbf{j}^{\mathbf{p}}(\mathbf{r}) = \frac{i\hbar}{2m}\sum_\sigma [(\nabla_{\mathbf{r}} a^\dagger_{\mathbf{r}\sigma})a_{\mathbf{r}\sigma} - a^\dagger_{\mathbf{r}\sigma}(\nabla_{\mathbf{r}} a_{\mathbf{r}\sigma})] \tag{3.7}$$

$$\mathbf{j}^{\mathbf{d}}(\mathbf{r}) = -\frac{e}{m}\sum_{\sigma}\mathbf{A}(\mathbf{r})a^{\dagger}_{\mathbf{r}\sigma}a_{\mathbf{r}\sigma} \tag{3.8}$$

The two currents are called paramagnetic and diamagnetic. a and $a^{\dagger}$ are the annihilation and creation operators and σ is the spin index. The paramagnetic term, in momentum space $\mathbf{q}$, has the form

$$\mathbf{j}^{\mathbf{p}}(\mathbf{q}) = \frac{\hbar}{m}\sum_{\mathbf{k}\sigma}\left(\mathbf{k}+\frac{\mathbf{q}}{2}\right)a^{\dagger}_{\mathbf{k}\sigma}a_{\mathbf{k}+\mathbf{q}\sigma} \tag{3.9}$$

Using these definitions and linear response theory, a relationship for the conductivity in terms of correlation functions can be derived. This is known as the Kubo formula. This is given in frequency ω and momentum space by

$$\sigma_{\mu\nu}(\mathbf{q},\omega) = \frac{ie^2\hbar}{\omega}\left[\frac{1}{\mathcal{V}}\chi^{\mu\nu}_{jj}(\mathbf{q}, i\Omega_n \to \omega + i0^{+}) + \delta_{\mu\nu}\frac{\langle n\rangle}{m}\right] \tag{3.10}$$

where we have indicated by the symbol $\chi^{\mu\nu}_{jj}$ the paramagnetic current-current correlation function. This can be obtained in frequency space by performing the analytic continuation of the imaginary time current-current correlation function

$$\chi^{\mu\nu}_{jj}(\mathbf{q},\tau) = -\langle T_\tau j^p_\mu(\mathbf{q},\tau)j^p_\nu(-\mathbf{q},0)\rangle \tag{3.11}$$

$$= -\left(\frac{\hbar}{m}\right)^2\sum_{\mathbf{k}\sigma}\sum_{\mathbf{k}'\sigma'}\left(k_\mu+\frac{q_\mu}{2}\right)\left(k'_\nu-\frac{q_\nu}{2}\right)\langle T_\tau a^{\dagger}_{\mathbf{k}\sigma}(\tau)a_{\mathbf{k}+\mathbf{q}\sigma}(\tau)a^{\dagger}_{\mathbf{k}'\sigma'}(0)a_{\mathbf{k}'-\mathbf{q}\sigma'}(0)\rangle \tag{3.12}$$

where T_τ is the imaginary time ordering operator. The other elements of the Kubo formula are the volume $\mathcal{V}$, the average of the density operator $\langle n\rangle$ and the electron mass m. From this expression we can proceed to compute the conductivity from first principles. Since we have applied the linear response theory, the thermodynamic average entering the current-current correlation function is computed using an hamiltonian without the current-vector potential coupling. But the hamiltonian can contain other interactions, such as a one-body potential describing scattering from impurities.

Since we are considering the limit of weak disorder, this calculation can be performed using a perturbative diagrammatic approach. At order zero we have

$$\begin{aligned}&\langle T_\tau a^{\dagger}_{\mathbf{k}\sigma}(\tau)a_{\mathbf{k}+\mathbf{q}\sigma}(\tau)a^{\dagger}_{\mathbf{k}'\sigma'}(0)a_{\mathbf{k}'-\mathbf{q}\sigma'}(0)\rangle_0\\ &= \langle T_\tau a^{\dagger}_{\mathbf{k}\sigma}(\tau)a_{\mathbf{k}'-\mathbf{q}\sigma'}(0)\rangle_0\langle T_\tau a_{\mathbf{k}+\mathbf{q}\sigma}(\tau))a^{\dagger}_{\mathbf{k}'\sigma'}(0)\rangle_0\\ &= -\mathcal{G}^0_{\mathbf{k}'-\mathbf{q}\sigma'\,\mathbf{k}\sigma}(-\tau)\mathcal{G}^0_{\mathbf{k}+\mathbf{q}\sigma\,\mathbf{k}'\sigma'}(\tau)\end{aligned} \tag{3.13}$$

where $\mathcal{G}^0$ is the free propagator. Therefore the zero order contribution can be regarded as the free propagation of an electron hole pair and it is represented by the diagram in Figure 3.1.

By considering higher order terms we can classify all possible diagrams into the two groups presented in Figure 3.2: the one on the left represents all the diagrams leading to the renormalisation of the propagators while the one on the right represents all diagrams in which interaction lines connect the electron and hole lines. The members of the latter class are also called *vertex corrections*.

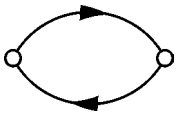

Figure 3.1: Zero order conductivity diagram. From [97]

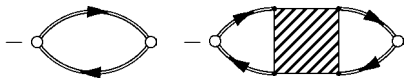

Figure 3.2: Conductivity diagrams. On the left: diagrams leading to the renormalisation of the propagators. On the right: vertex corrections. From [96]

In this framework the current-current correlation function is given, in terms of the one-electron spectral function A and Fermi distribution f, by the expression

$$\chi_{jj}^{\mu\nu}(\mathbf{q}, i\Omega_n) = \left(\frac{\hbar}{m}\right)^2 \sum_{\mathbf{k}\sigma} \left(k_\mu + \frac{q_\mu}{2}\right)\left(k_\nu - \frac{q_\nu}{2}\right) \int d\epsilon_1 d\epsilon_2 A(\mathbf{k}, \epsilon_1) A(\mathbf{k}+\mathbf{q}, \epsilon_2)$$

$$\times \frac{f(\epsilon_1) - f(\epsilon_2)}{i\Omega_n + \epsilon_1 - \epsilon_2} + \text{ vertex corrections} \tag{3.14}$$

We can take into account the effect of disorder by calculating the self-energy Σ for impurity scattered electrons and use the resulting propagators $\mathcal{G}(\mathbf{k}, i\nu_n) = [i\nu_n - \xi_{\mathbf{k}} - \Sigma(\mathbf{k}, i\nu_n)]^{-1}$ in the calculation of the one-electron spectral function. The simplest low-order approximation that introduces damping in the self-energy (a non-zero imaginary part) is the first order Born approximation, represented in Figure 3.3. Using this approach, all possible processes in which an electron is scattered twice by the same impurity are considered. In this approximation, the self-energy is given by

$$\Sigma^{\text{1BA}}(\mathbf{k}, i\nu_n) = n_i \frac{1}{\mathcal{V}} \sum_{\mathbf{q}} \frac{|v(\mathbf{q})|^2}{i\nu_n - \xi_{\mathbf{k}-\mathbf{q}}}. \tag{3.15}$$

$i\nu_n$ are the Matsubara frequencies, n_i is the impurity density, $v(\mathbf{q})$ the Fourier transform of the impurity potential and $\xi_{\mathbf{k}}$ the electrons dispersion. By using this form of the self-energy in equation 3.14 and neglecting vertex corrections, we are able to describe the Drude conductivity $\sigma = ne^2\tau/m$ in terms of quasi-particle scattering. To describe electron localisation though, which is the focus of our discussion, we need to consider the vertex corrections.

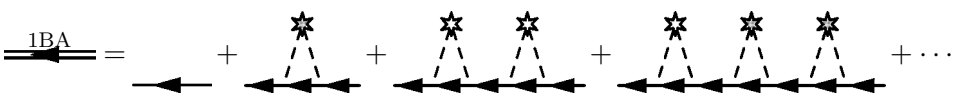

Figure 3.3: First Born approximation. From [97]

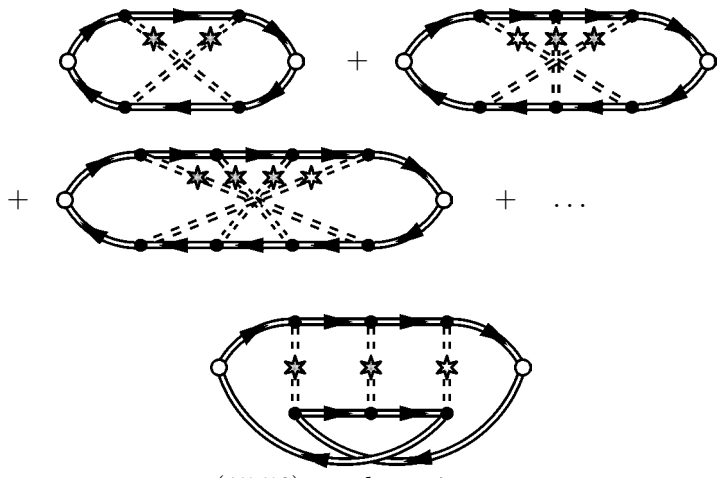

Figure 3.4: Maximally crossed diagrams. From [97]

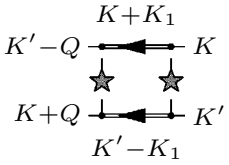

Figure 3.5: Ladder sum in the particle-particle channel. From [96]

3.2.2 Weak localisation

An important class of vertex corrections is illustrated in Figure 3.4. In literature these diagrams are called *maximally crossed* and they seem, at first sight, to describe very complicated scattering processes of dubious interest. It is only by twisting the bottom half of the diagram that we come to realise their importance: this series gives rise to a ladder summation in the particle-particle channel that describes the propagation of electrons repeatedly interacting with each other. This series of diagrams is also known as the *cooperon*. In the case of scattering from impurities that we are considering, these diagrams describe electrons following the same diffusion path around impurities in opposite (time reversed) directions. If these loops are shorter than the inelastic scattering length then pairs of waves following the same path in opposite directions will keep a constant phase relation and will interfere. As we will see shortly, this leads to an enhancement of backscattering, and therefore to a decrease in conductance.

The basic element of the cooperon Λ^{C} is illustrated in detail in Figure 3.5. Translating the diagram into mathematical symbols and considering the case of point-like impurities ($v(\mathbf{q}) = v_0$) and the limit $Q \to 0$, we find a geometric series

$$\Lambda^{\mathrm{C}} = (n_i v_0^2)^2 \sum_{K_1} \mathcal{G}(K + K_1)\mathcal{G}(K' - K_1)$$

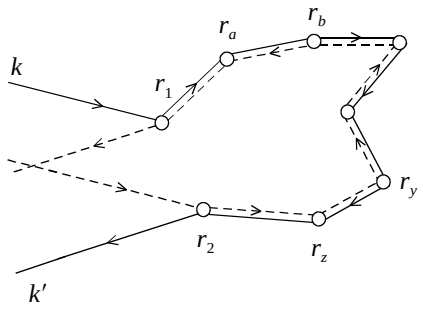

Figure 3.6: A sequence of multiple scattering events giving rise to coherent backscattering. From [98]

$$+(n_i v_0^2)^3 \sum_{K_1} \mathcal{G}(K+K_1)\mathcal{G}(K'-K_1) \sum_{K_2} \mathcal{G}(K+K_2)\mathcal{G}(K'-K_2) + ...$$

$$= (n_i v_0^2)^2 \zeta(K+K')\{1 + n_i v_0^2 \zeta(K+K') + [n_i v_0^2 \zeta(K+K')]^2 + ...\}$$

$$= \frac{(n_i v_0^2)^2 \zeta(K+K')}{1 - n_i v_0^2 \zeta(K+K')} \tag{3.16}$$

$$\zeta(K+K') = \sum_{K_1} \mathcal{G}(K+K_1)\mathcal{G}(K'-K_1). \tag{3.17}$$

Here we used the notation

$$K = (\mathbf{k}, \sigma, i\omega_n),\ Q = (\mathbf{q}, i\Omega_n),\ \sum_K = \sum_{\mathbf{k}\sigma} \frac{1}{\beta} \sum_{i\omega_n} \tag{3.18}$$

Within the first Born approximation we find that $n_i v_0^2 \zeta(0) = 1$. Hence the cooperon (and the contribution to the conductance it generates) diverges for $K \approx -K'$. This has an important consequence: the scattering processes leading to a conductivity correction are not only those where the trajectories form closed loops as at the end of the loop the electrons must also be back-scattered or nearly back-scattered. The scattering processes giving rise to this correction are illustrated, in real space, in Figure 3.6.

The calculation of the corresponding conductivity correction $\Delta\sigma^{\mathrm{WL}}$ leads to the following result for $d = 2$

$$\Delta\sigma^{\mathrm{WL}} = -\frac{e^2}{\pi h} \ln\left(\frac{\tau_i}{\tau}\right). \tag{3.19}$$

There are three remarkable features of this result: the magnitude of the conductivity correction is universal ($e^2/\pi h \simeq 1.2 \cdot 10^{-5}$ S), *negative* and depends on the logarithm of the ratio between the inelastic scattering time τ_i and the elastic scattering time. Because these electrons interference effects tend to decrease the conductance, this quantum correction has been named weak localisation. The ratio between the Drude conductivity σ_0 and the weak localisation correction is given by

$$\frac{\Delta\sigma^{\mathrm{WL}}}{\sigma_0} = \frac{1}{\pi k_{\mathrm{F}} l} \ln\left(\frac{\tau_i}{\tau}\right). \tag{3.20}$$

This formula has the advantage of showing clearly in terms of the product $k_{\mathrm{F}}l$ (therefore the Thouless number g introduced in section 3.1), the relevance of the weak localisation correction. This description breaks down for $k_{\mathrm{F}}l \sim 1$, where an analysis of the effect of the disorder based on perturbation theory ceases to be appropriate. This leads us naturally to the definition of a localisation length

$$\xi_{\mathrm{loc}} = l e^{\pi k_{\mathrm{F}} l} \tag{3.21}$$

which is the phase coherence length required to observe the transition from a weak to a strong localisation regime. Finally we remark that this correction gives a divergent result for $T \to 0$.

3.2.3 Experimental probes

In the preceding section we have seen that the magnitude of the weak localisation correction is proportional to $\ln(\tau_i/\tau)$. Since this ratio grows with decreasing temperature, a logarithmic upturn of the resistivity at low temperatures is predicted. The exact temperature dependence is defined by the physical mechanisms regulating the growth of the inelastic scattering time with decreasing temperature (electron-phonon interactions or electron-electron interactions). A power law $\tau_i \propto T^{-p}$ is generally observed with $p = 3$ for electron-phonon interactions and $p = 1$ for electron-electron interactions in $d = 2$. Therefore, at the lowest temperatures, where the loss of phase coherence is related to electron-electron interactions we expect the following temperature dependence of the conductivity

$$\sigma = \sigma_0 - \frac{e^2}{\pi h} \ln T \tag{3.22}$$

Another elegant way to probe the weak localisation correction is to observe the variation of conductance induced by a magnetic field. Since weak localisation gives a negative contribution to the conductivity, its suppression by a magnetic field leads to an increase in conductivity. The typical scale of magnetic fields is set by $\hbar/eD\tau_i$ which corresponds to a field that couples a flux quantum $h/2e$ through an area $\pi D\tau_i$ over which phase coherence is established. This scale is non-universal since the diffusion coefficient depends on the electrons effective mass and on the carrier concentration.

3.3 Spin-orbit interaction

In the preceding section we have discussed quantum corrections to the conductance arising from the electrons interference. To enter deeper into this subject we need to consider the role that the spin plays in this context. In this section we will consider the spin-orbit interaction and its peculiarities when applied to condensed-matter physics. The spin-orbit interaction emerges naturally when one considers relativistic effects in quantum mechanics. Let us consider an electron moving with velocity $\mathbf{v}$ in an electric field $-\mathbf{E} = -\nabla V/e$. According to special relativity the electron "sees" in its rest frame a magnetic field $\mathbf{B}$ given by

$$\mathbf{B} = -\frac{\mathbf{v}}{c^2} \times \mathbf{E} = -\frac{\mathbf{p}}{mc^2} \times \mathbf{E} \tag{3.23}$$

The coupling of the spin magnetic moment $\mu_{\mathbf{s}} = -(ge/2m)\mathbf{s}$ to this field gives rise to the energy term

$$-\mu_{\mathbf{s}} \cdot \mathbf{B} = \mu_{\mathbf{s}} \cdot \frac{\mathbf{p}}{mc^2} \times \mathbf{E} = -\frac{g}{2m^2c^2}\mathbf{s} \cdot \mathbf{p} \times \nabla \mathbf{V} \tag{3.24}$$

where $\mathbf{s} = (\hbar/2)\sigma$, and $\sigma = (\sigma_x, \sigma_y, \sigma_z)$ are the Pauli matrices

$$\sigma_x = \begin{pmatrix} 0 & 1 \\ 1 & 0 \end{pmatrix},\ \sigma_y = \begin{pmatrix} 0 & -i \\ i & 0 \end{pmatrix},\ \sigma_z = \begin{pmatrix} 1 & 0 \\ 0 & -1 \end{pmatrix}$$

This derivation is not very rigorous, but has the advantage of keeping a transparent physical picture. Unfortunately, our calculation of the Lorentz transformation is not completely correct, since we did not account for the acceleration of the electron under the electric field. A more formal approach, based on the Dirac equation, leads to the following result for the spin-orbit interaction V_{so}, which differ from our heuristic argument by a factor 1/2:

$$V_{\text{so}} = -\frac{g\hbar}{8m^2c^2}\sigma \cdot \mathbf{p} \times \nabla V \tag{3.25}$$

If we consider the example of an electron moving in a potential characterised by central symmetry $V = V(r)$

$$\nabla V(r) = \frac{1}{r}\frac{\mathrm{d}V}{\mathrm{d}r}\mathbf{r} \tag{3.26}$$

we can write the interaction as

$$V_{\text{so}} = \frac{g\hbar}{8m^2c^2}\frac{1}{r}\frac{\mathrm{d}V}{\mathrm{d}r}\sigma \cdot \mathbf{L} \tag{3.27}$$

where $\mathbf{L} = \mathbf{r} \times \mathbf{p}$ is the electrons orbital momentum. This form highlights the reason for the name "spin-orbit interaction", since this potential describes the coupling of the spin with an orbital momentum.

3.3.1 Rashba hamiltonian

Let us now consider an ideal model of free electrons confined in a two-dimensional x, y plane with an homogeneous electric field directed along z. In this condition the spin-orbit interaction acquires the so-called Rashba form [99, 100]

$$H_{\text{R}} = \frac{\alpha}{\hbar}\sigma \cdot \mathbf{p} \times \hat{\mathbf{z}} \tag{3.28}$$

where α is a coupling constant and $\hat{\mathbf{z}}$ a unit vector in the z direction. The full hamiltonian is therefore

$$H = \frac{p^2}{2m} + \frac{\alpha}{\hbar}(p_y\sigma_x - p_x\sigma_y) \tag{3.29}$$

Since momentum is a good quantum number we can look for solutions of the kind $|\Psi\rangle = |\mathbf{k}\rangle|\psi\rangle$, where $\langle \mathbf{x}|\mathbf{k}\rangle \propto e^{i\mathbf{k}\cdot\mathbf{x}}$ is a plane wave and $|\psi\rangle$ is a spin state. Using explicitly the Pauli operators previously defined and expressing the wave-vector as $\mathbf{k} = k(\cos\phi, \sin\phi, 0)$, we can write down the hamiltonian in the form

$$H = \frac{\hbar^2k^2}{2m}\begin{pmatrix} 1 & i\eta e^{-i\phi} \\ -i\eta e^{i\phi} & 1 \end{pmatrix}$$

where $\eta = 2m\alpha/(\hbar^2 k)$. We can find its eigenvalues by solving the quadratic equation

$$\det \begin{pmatrix} 1-\lambda & i\eta e^{-i\phi} \\ -i\eta e^{i\phi} & 1-\lambda \end{pmatrix} = (1-\lambda)^2 - \eta^2 = 0$$

which has the ϕ-independent solutions $\lambda^{\pm} = 1 \pm \eta$. Therefore the energy eigenstates are given by

$$E^{\pm} = \frac{\hbar^2 k^2}{2m} \pm \alpha k \tag{3.30}$$

It is important to note that the energy depends on the spin state (here indicated as $+$ or $-$). The normalised spin eigenvectors are

$$|\psi^{+}\rangle = \frac{1}{\sqrt{2}}(ie^{-i\phi}, 1) \tag{3.31}$$

$$|\psi^{-}\rangle = \frac{1}{\sqrt{2}}(-ie^{-i\phi}, 1) \tag{3.32}$$

One important result is that the spin direction is tied to the electron momentum, since it depends on the parameter ϕ. We can learn more about the spin direction by applying the Pauli matrices to these states. This allows us to track the spin direction in momentum space. By direct computation we find

$$\vec{S}^{+} = (\langle\psi^{+}|\sigma_x|\psi^{+}\rangle, \langle\psi^{+}|\sigma_y|\psi^{+}\rangle, \langle\psi^{+}|\sigma_z|\psi^{+}\rangle) = \frac{2}{\sqrt{2}}(\sin\phi, -\cos\phi, 0) \tag{3.33}$$

$$\vec{S}^{-} = (\langle\psi^{-}|\sigma_x|\psi^{-}\rangle, \langle\psi^{-}|\sigma_y|\psi^{-}\rangle, \langle\psi^{-}|\sigma_z|\psi^{-}\rangle) = \frac{2}{\sqrt{2}}(-\sin\phi, \cos\phi, 0) \tag{3.34}$$

From these equations we can see that the spin is always perpendicular to the momentum and its direction is given by

$$\widehat{S}^{\pm} = \pm\widehat{\mathbf{k}} \times \widehat{z} \tag{3.35}$$

These calculations lead us to sketch the energy dispersion represented in Figure 3.7. At this point it is important to highlight the following features of this model:

- The Fermi surface splits in two concentric circles with radii $k_{\rm so} + (k_{\rm so}^2 + k_{\rm F}^2)^{1/2}$ and $k_{\rm so} - (k_{\rm so}^2 + k_{\rm F}^2)^{1/2}$, with $k_{\rm so} = \alpha m/\hbar^2$.

- The momentum states of the spin (+) and spin (-) electrons are not degenerate: $E_{\mathbf{k},+} \neq E_{\mathbf{k},-}$. There is an energy difference $\Delta = 2\alpha k_{\rm F}$ between states having the same wave-vector but different spin orientations. This is a typical situation found in the electronic structure of solids whose bulk crystal structure does not possess inversion symmetry. One of the most studied examples is the zinc-blend structure found in the semiconductor GaAs, where the spin-orbit interaction has a specific momentum dependence, known as the Dresselhaus form. In interfaces, the Rashba model is taken as representative of the physics brought about by the absence of structural inversion symmetry. Note that Kramer's degeneracy (time reversal symmetry), which requires $E_{\mathbf{k},+} = E_{-\mathbf{k},-}$, is preserved.

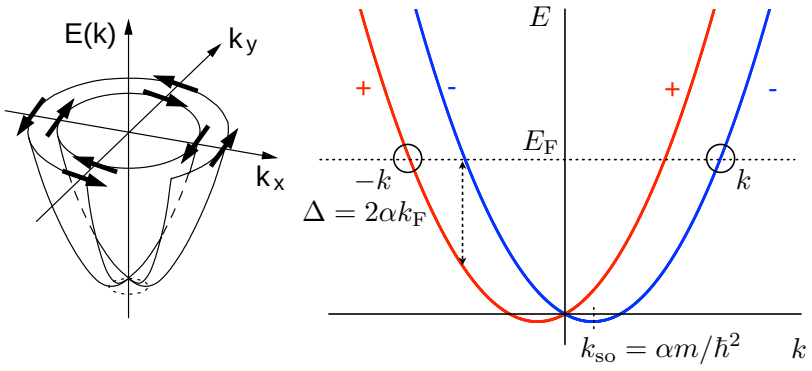

Figure 3.7: Energy-momentum relation for free electrons with Rashba interaction. The three dimensional representation is from [100].

- There is a difference $2k_{so}$ in wavevector between electrons having the same energy and traveling in the same direction but different spin orientations.

Perhaps the most important consequence of the spin-orbit interaction in the light of our discussion is that, in the presence of disorder, the spin is not a conserved quantity. According to the Rashba model, a backscattering ($\mathbf{k} \rightarrow -\mathbf{k}$) requires a spin flip, as illustrated in Figure 3.7. In a diffusive system the wave-vector will rotate at every scattering event causing a reorientation of the spin. In the absence of inversion symmetry these fluctuations will define a spin relaxation time τ_{so} according to the D'yakonov-Perel' (DP) mechanism [101]. In this scenario, the Rashba coupling constant α and the spin relaxation time τ_{so} are related through

$$\tau_{so} = \hbar^4/4\alpha^2 m^2 2D \tag{3.36}$$

where m is the carrier mass and D the diffusion constant. A second class of spin relaxation processes, known as the Elliott-Yafet (EY) mechanism, originates from the spin-orbit interaction of the lattice ions with the conduction electrons [102, 103] and it is present also in centrosymmetric solids. This spin relaxation mechanism can become relevant in the presence of strong spin-orbit scattering impurities or whenever the ionic spin-orbit coupling produces a significant correction to the band structure of the material.

If both mechanisms are at play, one can identify the dominant one by studying the dependence of the spin relaxation time on the elastic scattering time τ [101]. In the case of the EY mechanism (ionic spin-orbit interaction), the Elliott relation

$$\tau_{so} \sim \tau/(\Delta g)^2 \tag{3.37}$$

(Δg is the difference between the electrons g-factor in the solid and the one of free electrons) predicts a direct proportionality between the spin relaxation time and the elastic scattering time. In a DP scenario (Rashba spin-orbit interaction) the spin relaxation time should be inversely proportional to the elastic scattering time.

$$\tau_{so} \sim 1/\tau \tag{3.38}$$

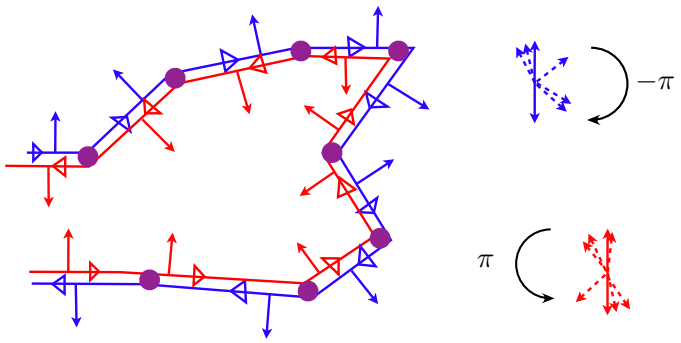

Figure 3.8: Visual representation of the suppression of backscattering brought about by the spin-orbit interaction.

3.4 Weak antilocalisation

The picture of weak localisation that we previously discussed is modified by taking into account spin effects. It has been shown both theoretically and experimentally that in the presence of spin-orbit interaction, electron interference can bring about a positive contribution to the conductance. Therefore, the suppression of this positive contribution by an external magnetic field causes a decrease in conductance. This regime of electron interference has been named weak antilocalisation, since it leads to a behaviour in magnetic field which is essentially the opposite of what we discussed so far in relation with weak localisation. The origin of this behaviour is rooted in a mysterious property of quantum mechanics: a rotation by 2π of spin 1/2 particles does not bring you back to the initial state. Instead the electronic wavefunction, upon full rotation, acquires a minus sign. This principe has profound consequences when applied to closed electronic loops. In Figure 3.8 one possible evolution of a pair of time reversed electrons, in the presence of Rashba spin-orbit interaction, is displayed. We already commented in section 3.3.1 and Figure 3.7 that in this scenario a backscattering event requires a spin flip. Here we can realise once again that by completing the loop, one spin is rotated by π, while its partner is rotated by $-\pi$. Therefore the two paths differ by a $\pi - (-\pi) = 2\pi$ rotation of the electron spin. A quantum mechanical phase factor of -1, associated with this difference of 2π, leads to destructive interference of the two paths, effectively suppressing this channel of backscattering for the electrons and leading to an increase in conductance.

In a famous series of experiments, G. Bergman measured the magnetoconductance of magnesium films with different concentrations of gold impurities [104]. The spin-orbit coupling increases with the gold concentration and the magnetoconductance is tuned from positive to negative (see Figure 3.9). This problem was tackled theoretically first by Hikami, Larkin and Nagaoka who calculated the cooperon in the spin-dependent case, generalizing the results previously discussed [105]. They found the conductivity correction to be

$$\Delta\sigma^{\mathrm{WL,WAL}} = -\alpha\frac{e^2}{\pi^2\hbar}\ln\left(\frac{\tau_i}{\tau}\right) \tag{3.39}$$

with $\alpha = -1/2$ with spin-orbit coupling and $\alpha = +1$ without. As we will discuss fur-

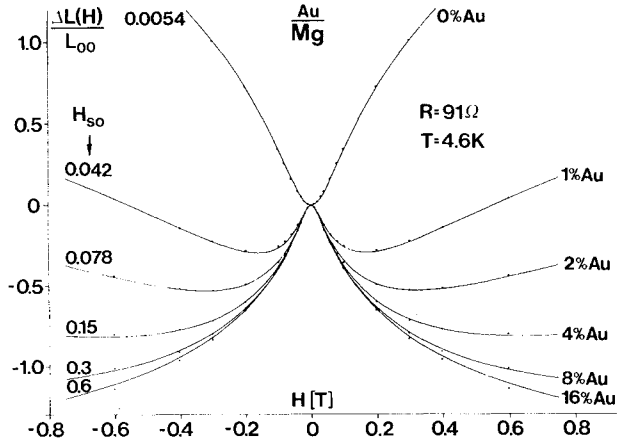

Figure 3.9: Variation of conductance ΔL with respect to $L_{00} = e^2/\pi h$ as a function of magnetic field of a thin Mg film, measured for different coverage of Au (spin-orbit scatterers concentration). From [104]

ther, the sign of the quantum conductivity correction bears important consequences on the electronic properties of the system. The authors also calculated the magnetic field dependence of the conductance. Maekawa and Fukuyama confirmed this result and extended the previous calculation by taking into account the Zeeman splitting [106]. According to their calculation, in a two-dimensional layer with in-plane spin-orbit relaxation, immersed in a perpendicular magnetic field H, the first order correction to the conductance, $\Delta\sigma$, takes the form

$$\begin{aligned}\frac{\Delta\sigma(H)}{e^2/\pi h} &= \Psi\left(\frac{H}{H_{\rm i}+H_{\rm so}}\right)\\ &+\frac{1}{2\sqrt{1-\gamma^2}}\Psi\left(\frac{H}{H_{\rm i}+H_{\rm so}\left(1+\sqrt{1-\gamma^2}\right)}\right)\\ &-\frac{1}{2\sqrt{1-\gamma^2}}\Psi\left(\frac{H}{H_{\rm i}+H_{\rm so}\left(1-\sqrt{1-\gamma^2}\right)}\right)\end{aligned} \tag{3.40}$$

The function Ψ is defined as $\Psi(x) = \ln(x) + \psi\left(\frac{1}{2}+\frac{1}{x}\right)$, where $\psi(x)$ is the digamma function. The parameters of the theory are the inelastic field $H_{\rm i} = \hbar/4eD\tau_{\rm i}$, the spin-orbit field $H_{\rm so} = \hbar/4eD\tau_{\rm so}$ and the electrons g-factor g which enters into the Zeeman correction $\gamma = g\mu_B H/4eDH_{\rm so}$. μ_B is the Bohr magneton.

3.5 Strong localisation and the scaling theory

We have previously discussed that in the limit $k_{\rm F}l \sim 1$ a perturbative analysis of the effects of disorder is no longer appropriate. The regime of strong disorder has been studied by P.W. Anderson [108]. He pointed out that the nature of the electronic states

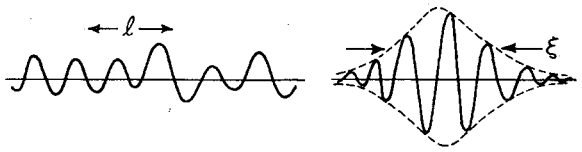

Figure 3.10: Wave function for the extended states with mean free path l (left) and for localised states with localisation length ξ (right). From [107]

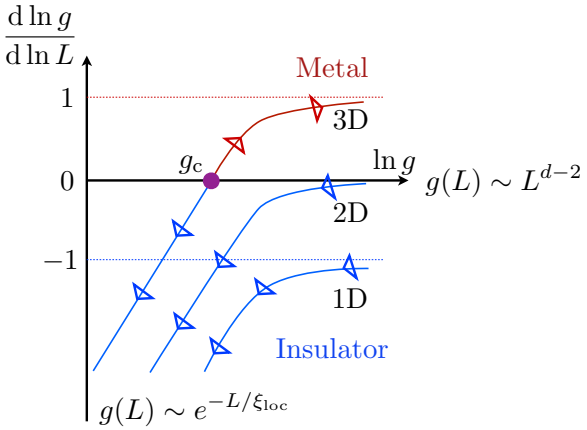

Figure 3.11: Plot of the β function for a non-interacting system in different dimensions.

changes entirely whenever the phase coherence length becomes larger than the localisation length ξ_{loc}, with the envelope of their wave functions decaying exponentially from some point in space $\mathbf{r_0}$

$$|\psi(\mathbf{r})| = \exp[(\mathbf{r} - \mathbf{r_0})/\xi_{\text{loc}}] \tag{3.41}$$

This is illustrated in Figure 3.10. The physical reason behind this behaviour is fairly easy to visualise in the limit of strong disorder: an extended state in a solid is the result of the overlap of localized orbitals that are nearly degenerate in energy. If the local potential fluctuates rapidly over the characteristic distance of an orbital exponential decay, there will be no chance of a matching between energy levels and therefore of delocalisation. The conductance of such a system will behave as

$$g(L) \propto \exp(-L/\xi_{\text{loc}}) \tag{3.42}$$

It is now very timely to consider the following question: can we describe the conductance of a phase coherent system of size L in terms of its smaller constituents? According to the scaling theory of localisation proposed by Abrahams, Anderson, Licciardello and Ramakrishnan [69] the answer is yes: the rate of change of the conductance g in response to a change in size L, can be expressed in terms of a single parameter, g itself. The following considerations are rigorously valid only for finite size systems at $T = 0$, the temperature at which the whole solid is phase coherent. To apply the results of this theory to real experiments performed at finite temperatures,

we will need to reinterpret L as the phase coherence length. We can then characterise the state of a disordered system with the aid of a scaling function β defined as

$$\beta(g) = \frac{\mathrm{d}\ln g}{\mathrm{d}\ln L}. \tag{3.43}$$

This function is *a priori* unknown, but we can make some reasonable assumptions on its form. So far we have considered disordered systems whose phase coherence length was larger or smaller than the localisation length and we found very different limiting behaviours:

- $g \gg 1$ yields an ohmic regime described by the drude conductivity and vertex corrections
$$g(L) = \frac{h}{e^2}\sigma L^{d-2} + \Delta g^{\mathrm{WL,WAL}}(L). \tag{3.44}$$
We remark that quantum corrections to the conductance have a characteristic size dependence in different dimensions. In $d = 2$ we have
$$g^{\mathrm{2D}}(L) = \frac{h}{e^2}\sigma - \alpha\frac{2}{\pi}\ln\left(\frac{L}{l}\right) \tag{3.45}$$
where we have replaced in equation 3.39 the phase coherence length with the system size.

- $g \ll 1$ gives an exponential suppression of the conductance
$$g(L) \propto \exp(-L/\xi_{\mathrm{loc}}). \tag{3.46}$$

Therefore, for large conductivity, neglecting vertex corrections, we expect for $\beta(g)$ the limit

$$\lim_{g\to\infty}\beta(g) = d - 2. \tag{3.47}$$

Considering vertex corrections, in $d = 2$ we have

$$\lim_{g\to\infty}\beta(g) \sim \lim_{g\to\infty}\left(-\frac{2\alpha}{\pi g}\right). \tag{3.48}$$

For small conductivity we expect the limit

$$\lim_{g\to 0}\beta(g) = \ln g. \tag{3.49}$$

Neglecting vertex corrections, and assuming that the function is continuous, we can sketch the form of β illustrated in Figure 3.11. The sign of β is very important since it informs us on the localised or delocalised nature of the electronic states of the system: a positive sign indicated that an increase in system size, or of its phase coherence length (decrease in temperature), produces an increase in conductivity (metallic regime), and a negative sign indicates the opposite behaviour (insulating regime). Therefore the scaling analysis summarised in Figure 3.11 reveals something very important: in a non-interacting system, where we can neglect vertex corrections, a metallic phase is not possible in one and two dimensions. In three dimension this theory predicts a metal to insulator transition at a critical conductivity g_{c}.

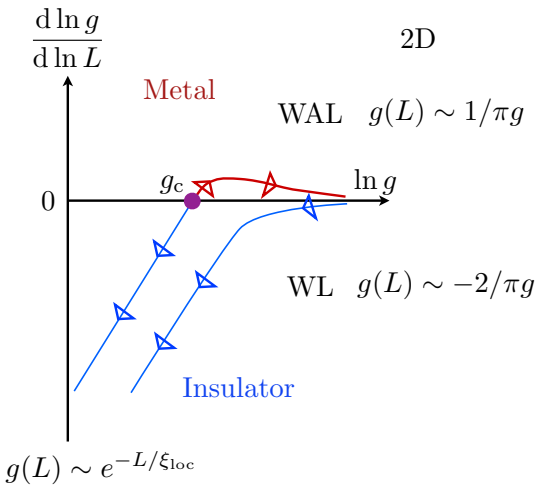

Figure 3.12: Plot of the β function in a two-dimensional system considering the quantum corrections to the conductivity and the spin-orbit interaction.

This picture is modified by taking into account the effect of vertex corrections such as weak (anti)localisation. In the two-dimensional case, the limit of β for $g \to \infty$ is still zero, like in the non-interacting picture, but the way this asymptote is approached depends on the sign of the quantum correction. In the case of weak localisation (disordered system without spin-orbit interaction) a metallic phase is precluded in $d = 2$ and, at sufficiently large size (low temperatures), a system with an arbitrarily small amount of disorder will flow towards strong localisation. In the case that the vertex correction produces a positive contribution to the conductance (weak antilocalisation, arising from the spin-orbit interaction) the scaling theory predicts a delocalised phase and a metal to insulator transition in $d = 2$, as shown in Figure 3.12.

The analysis we discussed so far does not account for interactions between the electrons. At low temperatures the electronic motion is diffusive between scattering events among electrons. In this regime these interactions bring about a depletion of the density of states at the Fermi energy, known as the Coulomb dip [98]. The resulting quantum correction to the conductivity (the Altshuler-Aronov correction) is logarithmic and negative. Since this correction is not tied to the evolution of the inelastic scattering time but rather depends on the thermal length $\sqrt{\hbar D/k_{\mathrm{B}}T}$ [109], we cannot directly account for its effect in a one-parameter scaling theory as we did for the spin-orbit correction. Recently, theoretical [110] and experimental [111] works have considered the role of electron-electron interactions in the framework of a two-parameter scaling theory of localisation. It was shown that a quantum critical point, that separates a metallic and an insulating phase in two dimensions, is stabilised by electronic interactions.

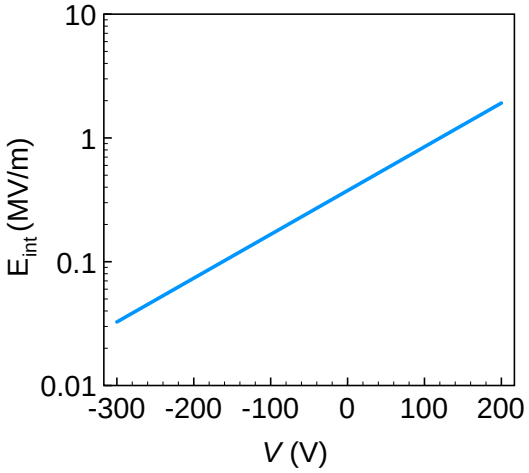

Figure 3.13: Interfacial electric field as a function of the gate voltage, estimated taking into account the electric field dependence of the permittivity of $SrTiO_3$.

3.6 Magnetotransport across the $LaAlO_3$/$SrTiO_3$ interface phase diagram

We are now equipped with the theoretical tools necessary to understand magnetotransport in a disordered system in the diffusive regime, that is $\omega_c\tau = \mu B < 1$.

As discussed in Chapter 1, it has been demonstrated by transport experiments [112] and conductive atomic force microscopy [41, 113] that the electron gas present in $LaAlO_3$/$SrTiO_3$ heterostructures grown using appropriate conditions is confined within a few nanometers from the interface. This structural configuration breaks inversion symmetry and, as a result, the electron gas confined in the vicinity of a polar interface [22] will experience a strong electric field directed perpendicular to the conduction plane. To provide an accurate representation of this internal electric field, the large local polarization of $SrTiO_3$ caused by its massive, electric field dependent, low temperature permittivity ($\epsilon_r > 10^4$) has to be considered [113].

A new class of physical phenomena occurring because of the presence of this effective electric field are captured by the Rashba hamiltonian[99]

$$H_{\mathrm{R}} = \alpha(\hat{n} \times \vec{k}) \cdot \vec{S} \tag{3.50}$$

where $\vec{S}$ are the Pauli matrices, $\vec{k}$ is the electron wave-vector and $\hat{n}$ is a unit vector perpendicular to the interface. This hamiltonian describes the coupling of the electrons spin to an internal magnetic field $\propto \hat{n} \times \vec{k}$, experienced in their rest frame, which is perpendicular to their wave-vector and lies in the plane of the interface. As discussed above, one important consequence of this interaction is that the dispersion relation of the electrons divides into two branches separated at the Fermi surface by a spin splitting $\Delta = 2\alpha k_{\mathrm{F}}$, k_{F} being the Fermi wave-vector and α the strength of the spin-orbit coupling. Perhaps the most appealing feature of this interaction is that its coupling constant is related to the electric field experienced by the electrons and can be therefore tuned by applying an external gate voltage [114, 115]. Aiming to explore this

phenomenon in $LaAlO_3/SrTiO_3$ interfaces, we fabricated field effect devices as discussed in Chapter 1. The interfacial electric field E_{int} is the solution of the integral equation [116, 100]

$$en_{2D} = \int_0^{E_{int}} \epsilon_0 \epsilon_r(E) dE \tag{3.51}$$

The field dependence of the permittivity of $SrTiO_3$ can be approximated as $\epsilon_r(E) = 1/(A + BE)$. In the device considered in this work we measured, in the bulk dielectric response of the single crystal of $SrTiO_3$, $A = 4 \cdot 10^{-5}$ and $B = 6.4 \cdot 10^{-10}$ m/V. Hence the effective electric field is given by

$$E_{\text{int}} = \frac{A}{B}\left(\exp\left(\frac{Ben_{2D}}{\epsilon_0} - 1\right)\right) \tag{3.52}$$

Therefore, we can estimate this quantity for each applied gate voltage by means of Hall effect measurements. In this calculation we are taking the bulk dielectric screening of $SrTiO_3$ as representative of the behaviour of the interface. Since at the interface the dielectric response is probably smaller than in the bulk, the electric field is probably underestimated. The electric field calculated using this approach is shown in Fig. 3.13. In our field effect experiments the exponential modulation of the electric field experienced by the electron gas arises from the special dielectric properties of $SrTiO_3$.

The magnetic field dependence of the conductance underscores the intriguing coupling between spin dynamics and transport. Fig. 3.14a shows the magnetoconductance $[\sigma(H) - \sigma(H = 0)]/\sigma(H = 0)$ (σ being the sheet conductance and H the applied magnetic field), measured in a magnetic field applied perpendicular to the $LaAlO_3/SrTiO_3$ interface at a temperature $T = 1.5$ K for gate voltages V between -300 V and +200 V. Measurements performed in a parallel field configuration are presented and discussed below. The magnetoconductance measurements are carried out using a standard four point DC technique. As shown in Fig. 3.14a, for large negative gate voltages we observe a large positive magnetoconductance that exceeds +25% at 8 T and -300 V. As we increase the voltage ($V > -200$ V), a low field regime characterized by a negative magnetoconductance appears. Increasing the gate voltage further, we observe that the negative magnetoconductance regime widens out. For the largest applied electric field, we observe that the magnetoconductance remains negative up to the largest accessible magnetic field (8 T). This behaviour has been observed in several samples. Similar modulations of the magnetoconductance have already been observed in metallic thin films [117] and semiconductor heterostructures [114, 115]. A comparison of our experimental data with the experiment reported in Ref. [117] is shown in Fig. 3.15 A possible interpretation of this behaviour is based on the presence of a strong spin-orbit interaction which counteracts weak localisation (weak antilocalisation) [105].

The influence of the spin-orbit interaction can be assessed by measuring the magnetoconductivity in the diffusive regime, where we can apply the Maekawa-Fukuyama (MF) theory introduced in section 3.4. Since we perform our experiments at 1.5 K, which is at least 5 times the maximum superconducting critical temperature, we can neglect superconducting fluctuations. In a magnetotransport experiment we can then quantify the two relevant time scales of the problem, namely τ_{so} and τ_{i}. The MF theory has been used to fit the experimental data of Fig. 3.14a in terms of variation of conductance with respect to $e^2/\pi h \simeq 1.2 \cdot 10^{-5}$ S. Since the effective mass (the

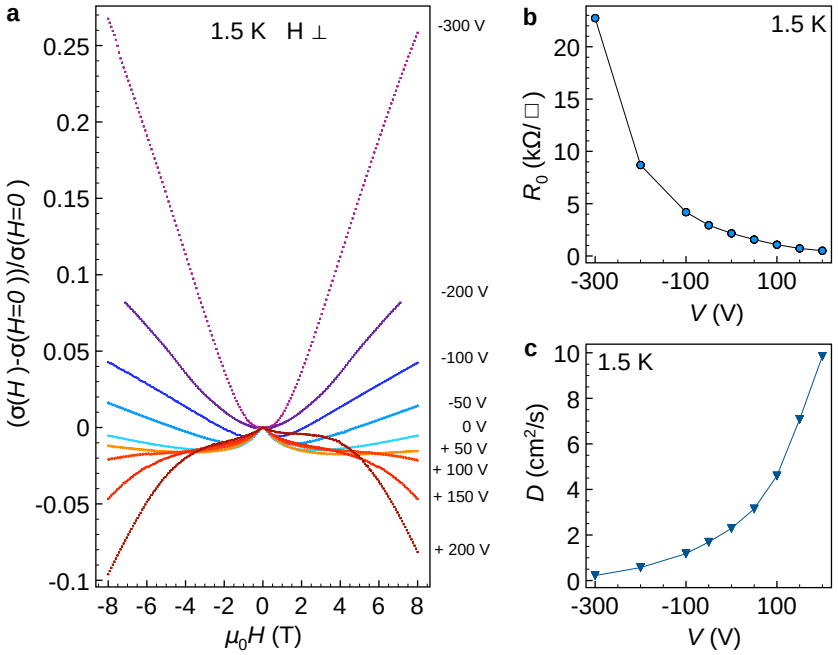

Figure 3.14: Modulation of the transport properties of the $LaAlO_3/SrTiO_3$ interface under electric and magnetic fields. (a) Magnetoconductance $[\sigma(H) - \sigma(H = 0)]/\sigma(H = 0)$ (σ being the sheet conductance, and H the applied magnetic field) measured at 1.5 K in perpendicular magnetic field for different applied gate voltages. (b) Sheet resistance (R_0) modulation resulting from the field effect measured at 1.5 K. (c) Field effect modulation of the diffusion coefficient D estimated at 1.5 K.

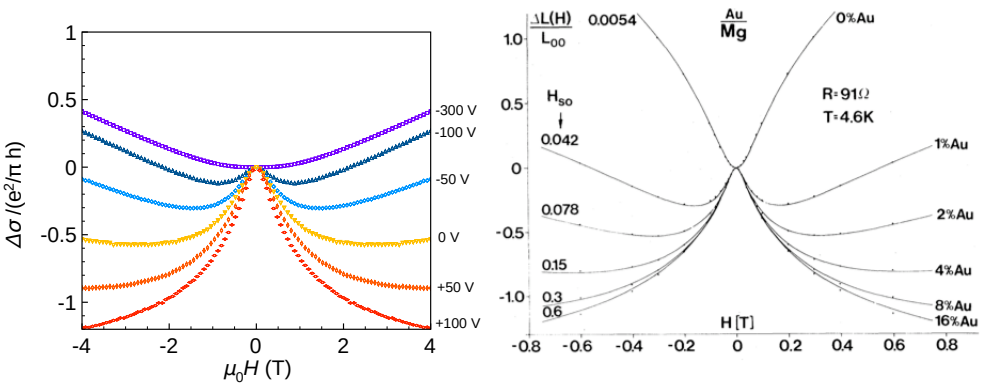

Figure 3.15: Comparison of the modulation of conductance obtained in $LaAlO_3/SrTiO_3$ interfaces by electric field effect (left) and the experiment reported in Ref. [117] (right). The ordinate scale is the same in both graphs.

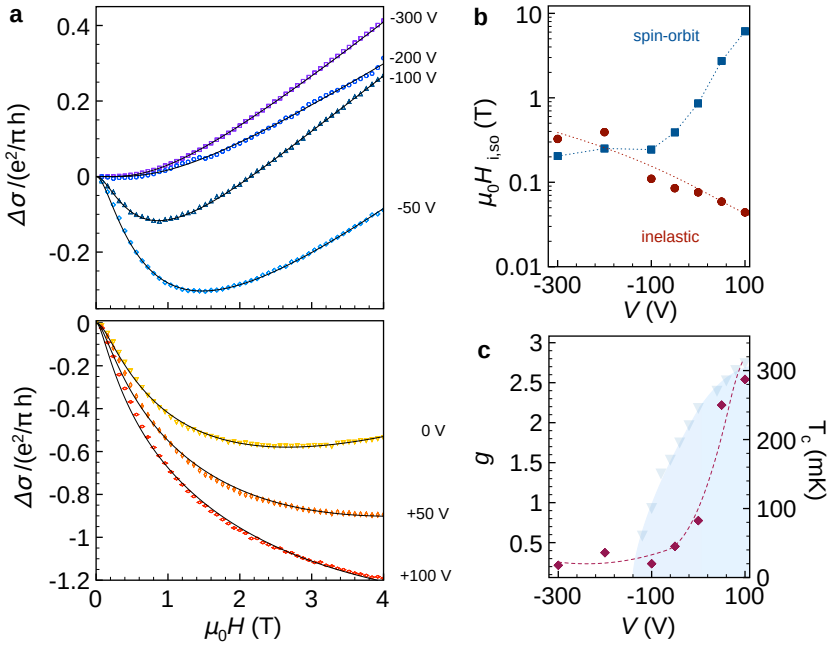

Figure 3.16: Analysis of the magnetoconductivity of the $LaAlO_3/SrTiO_3$ interface. (a) Best fits to Maekawa-Fukuyama theory of the variation of conductance $\Delta\sigma$, normalized with respect to $e^2/\pi h$, for different gate voltages. (b) Gate voltage dependence of the fitting parameters $H_{\rm i}$ (red dots) and $H_{\rm so}$ (blue squares). The lines are a guide to the eye. (c) Left axis, purple diamonds: gate voltage dependence of the electrons g-factor g. The line is a guide to the eye. Right axis, blue triangles: superconducting critical temperature T_c as a function of gate voltage for the same sample.

elastic scattering time) is one to two orders of magnitude larger (smaller) than the corresponding quantities for typical semiconductors, the diffusive regime holds for fields up to 4 T. For the range of fields and gate voltages (up to 100 V [1]) that we analyzed , weak localisation corrections dominate Coulomb interaction contributions. The best fits are presented in Fig. 3.16a, where we observe a remarkable agreement between theory and experiments. This analysis allows us to trace the electric field dependence of the parameters $H_{\mathrm{i,so}}$, presented in Fig. 3.16b, and γ. Analyses of the magnetoconductance performed using expressions derived by A. Punnoose [118] provide the same evolution of the characteristic fields. To extract from these parameters the relaxation times $\tau_{\mathrm{i,so}}$ and the electrons g-factor, we need to determine the electric field dependence of the diffusion coefficient. For this purpose we measured the electric field modulation of the sheet carrier concentration $n_{2\mathrm{D}}$ by means of Hall effect [119]. An estimate of the Fermi velocity v_{F} and of the elastic scattering time using a parabolic dispersion relation with an effective mass $m^* = 3m_e$ [5], (m_e is the bare electron mass) and data collected at the temperature $T = 1.5$ K, allows the diffusion coefficient to be calculated as $D = v_{\mathrm{F}}^2\tau/2$. D as a function of V is plotted in Fig. 3.14c.

The gate voltage dependence of the g-factor is presented in Fig. 3.16c. One observes a large increase from a small value, around 0.5 for negative voltages, towards the typical value of 2 for bare electrons at positive voltages. An electric field control of the g-factor has been previously predicted [120] and experimentally demonstrated [121] in semiconductor heterostructures. We now turn to the issue of the gate voltage dependence of the parameters $H_{\mathrm{i,so}}$ that will allow us to discern the modulation of spin-orbit coupling brought about by the electric field. The relaxation times $\tau_{\mathrm{i,so}}$ are plotted against gate voltage in Fig. 3.17a. For large negative gate voltages we observe that the inelastic scattering time is shorter than the spin relaxation time, indicating that the effect of the spin-orbit interaction is weak compared with the orbital effect of the magnetic field. In this regime, the quantum correction to the conductivity can be ascribed to weak localisation, in agreement with the the observed temperature evolution of the conductivity [119]. Above a critical voltage the spin relaxation time becomes shorter than the inelastic scattering time and decreases sharply, by three orders of magnitude, as the voltage is increased. By contrast, the inelastic scattering time remains fairly constant as we increase the voltage. Here a weak antilocalisation regime appears, characterized by a strong spin-orbit interaction. As previously discussed, the nature of the spin-orbit mechanism can be discerned by examining the dependence of the spin relaxation time on the elastic scattering time. In $SrTiO_3$, band structure calculations show that the Ti 3d conduction bands are notably altered by the bulk spin-orbit correction [5], therefore in principle the EY mechanism could be at play. In Fig. 3.17a we show the gate voltage dependence of the spin relaxation time predicted by the Elliott relation, calculated using the electrons g-factor presented in Fig. 3.16c. Clearly, the EY mechanism fails to estimate the spin relaxation time by 3 orders of magnitude at -300 V and its predicted variation with V is opposite to that observed. In fact, as can be seen in Fig. 3.17b, the spin relaxation time is proportional to the inverse of the elastic scattering time over a wide voltage range, a clear signature of the DP mechanism characteristic of the Rashba spin-orbit interaction. For $V > 50$ V, a deviation from the DP

[1] For $V > 100$ V the MF theory alone is not adequate to fit the data, indicating that additional contributions to the magnetoconductance need to be taken into account.

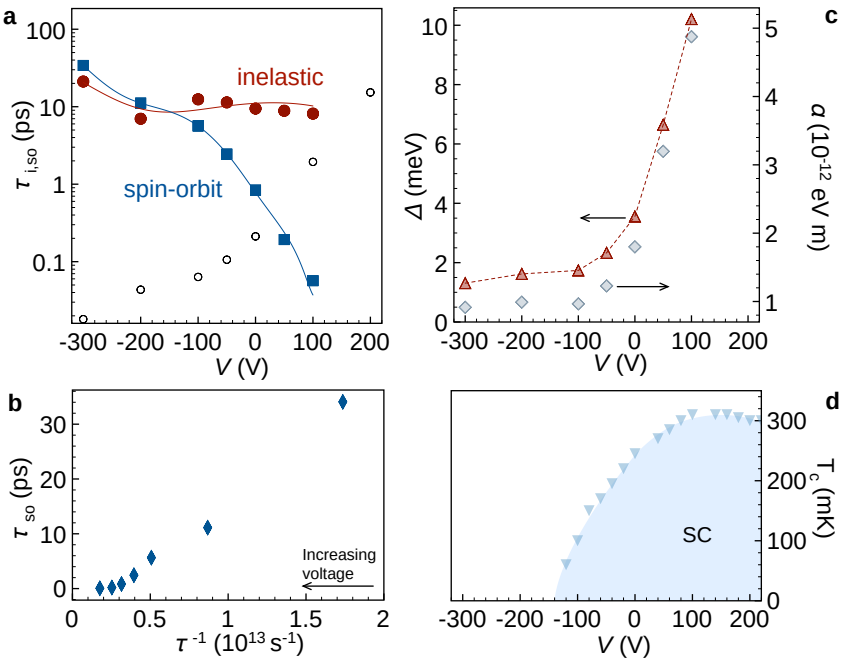

Figure 3.17: Rashba control of the $LaAlO_3/SrTiO_3$ interface electronic phase diagram. (a) Inelastic relaxation time τ_i (red circles) and spin relaxation time τ_{so} (blue squares) as a function of gate voltage plotted on a logarithmic time scale. The lines are a guide to the eye. Prediction of the spin relaxation time as a function of gate voltage based on the Elliott relation (open circles). (b) Spin relaxation time vs elastic scattering rate showing consistency with the D'yakonov-Perel' mechanism. (c) Left axis, red triangles: field effect modulation of the Rashba spin splitting Δ. Right axis, grey diamonds: field effect modulation of the Rashba coupling constant α. (d) Superconducting critical temperature T_c as a function of gate voltage for the same sample. Note that the crossing of the inelastic and spin relaxation times occurs at the quantum critical point.

relation is experimentally observed. This deviation coincides with the departure from the collision-dominated regime which occurs as τ_{so} becomes of order τ. This evolution points towards a strong spin-orbit coupling where an electron spin may precess through several cycles before scattering. These observations indicate that the unusually strong and tunable spin-orbit interaction found in $LaAlO_3/SrTiO_3$ heterostructures arises from the interfacial breaking of inversion symmetry.

A remarkable correlation between the onset of strong spin fluctuations and the emergence of superconductivity is evident by comparing Fig. 3.17a and d, where we notice that the superconducting dome, measured on the same sample, develops as the spin relaxation time becomes significantly smaller than the inelastic scattering time. This finding suggests that the spin-orbit interaction plays an important role in stabilizing a delocalized phase in two dimensions (see preceding section)[122], which condenses into a superconducting state. The gate voltage dependence of the diffusion coefficient previously presented corroborates this interpretation. In Fig. 3.17c we can appreciate the sharp increase of the spin-orbit coupling constant α as we move across the quantum critical point and the corresponding rise of the spin splitting Δ. This remarkable correlation between the critical temperature and the intensity of spin fluctuations is suggestive of an unconventional superconducting order parameter at the $LaAlO_3/SrTiO_3$ interface [123, 124]. The large change in spin relaxation across the phase diagram, which is not yet fully understood, may result from a complex dependence of the spin-orbit coupling on band structure properties and charge profile asymmetry. We note that the spin splitting values can be much higher than the superconducting gap (which is of the order of $40\,\mu$eV at optimal doping) and comparable to the Fermi energy (which is of the order of 20 meV). Hence the spin-orbit coupling turns out to be an essential ingredient to describe the electronic properties of the $LaAlO_3/SrTiO_3$ interface, both in the normal and superconducting state.

As we discussed in Section 3.5, in the diffusive regime both weak localisation and electron-electron interaction effects yield logarithmic corrections to the magnetoconductance. It is thus difficult, analysing only the magnetoconductance in perpendicular field, to sort out the different contributions. However, a magnetic field applied parallel to the conducting 2D layer quenches the orbital motion and, provided the spin-orbit contribution is negligible, leaves only the Coulomb contribution, whose strength depends on the electrons g-factor. In this case, the magnetic field polarizes the spins and leads to a negative contribution to the magnetoconductance. Similarly, if one applies a strong enough perpendicular field, one freezes out the weak localisation correction revealing the Coulomb contribution. In this field orientation, it is generally accepted that the orbital and spin-orbit corrections dominate for fields that satisfy $g\mu_B H/k_B T \ll 1$.

Fig. 3.18 displays magnetoconductance measurements for the parallel and perpendicular field orientations. For gate voltages smaller than 0 V, the Zeeman contribution is small up to 4 T. One has to recall (see Fig.3.16) that g is small so that, in this concentration range, weak localisation effects dominate for both field orientations. In this regard, we remark that the MF theory predicts in the presence of spin-orbit scattering a weak (compared to the perpendicular case) negative parallel magnetoconductance [106]. This is precisely what we observe for this range of gate voltages as shown in Fig.3.18. This observation, together with the absence of hysteresis, suggests that the positive magnetoconductance observed in the perpendicular orientation does not arise from magnetic effects [36].

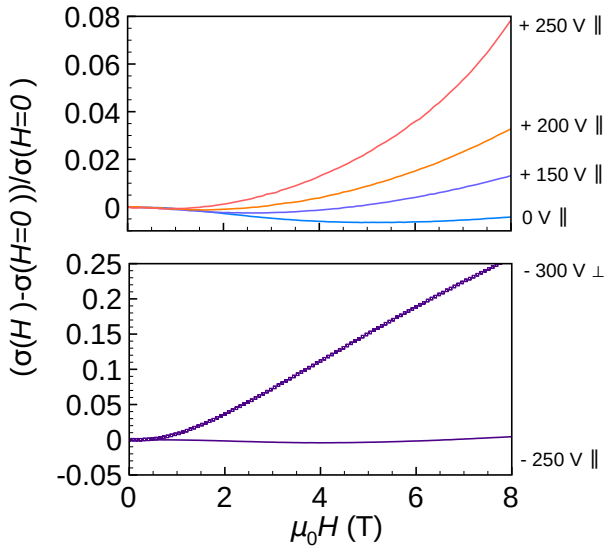

Figure 3.18: Magnetoconductance under electric field at 1.5 K. with magnetic field applied perpendicular and parallel to the $LaAlO_3/SrTiO_3$ interface.

Since the parameters that are extracted using Eq. 3.40 give excellent fits to the experimental data both at low and high perpendicular fields, this indicates that for gate voltages up to 100 V, Coulomb interactions yield small contributions compared to weak localisation. We remark (Fig. 3.18) that for high electric fields (150 V, 200 V and 250 V) in small parallel fields (less then 2 T) a negative magnetoconductance is observed as expected from spin-orbit and Coulomb contributions. The behaviour observed at higher parallel fields (positive large magnetoconductance) is not understood at the moment. Similar effects were measured in films of doped $SrTiO_3$ and interpreted as a dimensional crossover [125].

Chapter 4

Two-dimensional quantum oscillations

In the preceding chapter we have considered the modulation of the transport properties of the $LaAlO_3/SrTiO_3$ interface induced by an external magnetic field. We have limited our discussion to the diffusive regime, where the magnetoresponse is dominated by the effects of disorder (weak localisation) and spin-orbit interaction. This regime is characterised by an impurity scattering time τ that is shorter than the period of the orbital motion induced by the magnetic field. This is expressed by the relation $\omega_c\tau < 1$, where $\omega_c = e\mu_0 H/m^*$ is the cyclotron frequency, m^* is the carrier effective mass and $\mu_0 H$ the applied magnetic field. Since $\omega_c\tau = \mu\mu_0 H$, where μ is the sample mobility, we can easily identify which range of magnetic fields and sample mobilities pertains to the diffusive regime. In this Chapter we will discuss a magnetotransport study performed in samples in which the mobility has been boosted attaining the values of several thousands cm^2/Vs. In these samples, the description of magnetotransport that we discussed in Chapter 3 breaks down and new phenomena arise.

4.1 Onsager relation

The motion of an electron in a solid in an eigenstate of momentum $\vec{k}$ and energy $\epsilon(\vec{k})$, in the presence of a uniform magnetic field, can be described by the semiclassical equations

$$\frac{d}{dt}\vec{r} = \vec{v}(\vec{k}) = \frac{1}{\hbar}\nabla_{\vec{k}}\epsilon(\vec{k}) \tag{4.1}$$

$$\frac{d}{dt}\hbar\vec{k} = -e\vec{v}(\vec{k}) \times \vec{H} \tag{4.2}$$

These equations describe an orbital motion in momentum space along a constant-energy surface $A(\epsilon, k_z)$ (z is the magnetic field direction). The period of the orbit is given by

$$T(\epsilon, k_z) = \frac{\hbar^2}{e\mu_0 H}\partial_\epsilon A(\epsilon, k_z) \tag{4.3}$$

If $T < \tau$ we need to consider the quantization of the energy in closed orbits. In the case of free electrons, the energy levels are determined by the quantum numbers ν and k_z according to the relation

$$\epsilon_\nu(k_z) = \frac{\hbar^2 k_z^2}{2m} + \left(\nu + \frac{1}{2}\right)\hbar\omega_c \tag{4.4}$$

The energy states introduced by the quantized orbital motion are called Landau levels. Onsager generalised this result to electrons in solids, by considering the period of their orbits in momentum space and applying the Bohr quantization rules. He found that the density of states becomes singular at regularly spaced intervals in $1/H$. Since the conductance is a probe of the density of states at the Fermi energy, this will exhibit an oscillatory behaviour periodic in $1/H$. The Onsager relation establishes a direct proportionality between the cross-sectional extremal area of the Fermi surface normal to the magnetic field A, and the frequency of the oscillation ω (ϕ_0 is the magnetic flux quantum):

$$\omega = \frac{\phi_0}{2\pi^2} A \tag{4.5}$$

These oscillations of the electrical resistance as a function of magnetic field are known as Shubnikov-de Haas oscillations and are a useful tool for the characterisation of the Fermi surface of a material.

4.2 Shubnikov-de Haas oscillations in $LaAlO_3$/$SrTiO_3$ interfaces

In this thesis we have highlighted the remarkable electronic properties of the interface between the complex oxides $LaAlO_3$ and $SrTiO_3$ [22, 30, 126, 119, 127]. In this Chapter we will discuss the issue of the dimensionality of the conducting layer [113]. While it is clear that, using appropriate growth and annealing conditions, a confined metallic and superconducting electron gas can be formed at such interfaces [41, 112], no conclusive demonstration of two-dimensional character in the normal state has been presented in literature so far.

X-Ray absorption spectroscopy experiments [35], as well as density functional theory calculations [40], indicate that an orbital reconstruction occurs at this interface. These studies reveal that, even at room temperature, the degeneracy of the Ti $3d$ t_{2g} levels is lifted and the first available states for the conducting electrons are generated from $3d_{xy}$ orbitals, which give rise to strongly two-dimensional bands and present a negligible inter-plane coupling. Moreover, the momentum quantization in the quantum well brings about a sub-bands fine structure which was calculated [40, 39] but not yet confirmed experimentally. The presence of a very strong spin-orbit coupling, discussed in Chapter 3 adds further complexity to the low-energy electronic structure.

The Fermi surface of two-dimensional electronic states generates clear experimental signatures in the Shubnikov-de Haas (SdH) effect: for a two-dimensional electron gas (2DEG) the quantum oscillations depend only on the perpendicular component of the magnetic field. Previous studies reported quantum oscillations in $LaAlO_3$/$SrTiO_{3-\delta}$ heterostructures characterized by a large carrier density (of the order of 10^{16} cm^{-2}) delocalised in the $SrTiO_3$ substrate [22, 31]. The lack of dependence of the oscillations

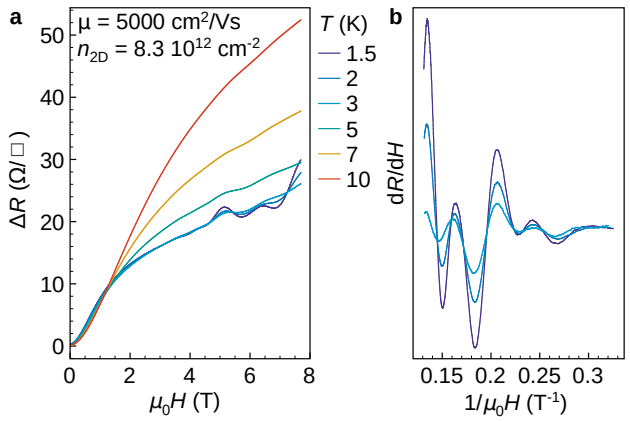

Figure 4.1: Shubnikov-de Haas oscillations of the $LaAlO_3/SrTiO_3$ interface. (a) Variation of resistance $\Delta R = R(H) - R(0)$ in response to the application of a magnetic field H oriented perpendicular to the $LaAlO_3/SrTiO_3$ interface, recorded at different temperatures T. (b) Numerical derivative $\mathrm{d}R/\mathrm{d}H$ as a function of the inverse of the magnetic field.

on the field orientation points to a three-dimensional Fermi surface consistently with previous studies in Nb-doped $SrTiO_3$ single crystals [128]. Very recently, quantum oscillations with two-dimensional character have been reported for Nb-doped thin films of $SrTiO_3$ [129].

The requirements for observing quantum conductance oscillations are [130]

$$\omega_c \tau > 1 \tag{4.6}$$

$$\hbar\omega_c > k_B T \tag{4.7}$$

To fulfill these conditions with temperatures of the order of 1 K and magnetic fields of a few Tesla, mobilities of 10^3 cm^2/Vs or more are required. Existing strategies to reach this value rely on the use of the electrostatic field effect [119, 131] or defect control [129, 132] to improve the quality of the devices.

Here we discuss a magnetotransport study performed in $LaAlO_3/SrTiO_3$ interfaces in which the mobility has been boosted by an optimization of the growth conditions, reaching the value of 6600 cm^2/Vs. In these samples we observe quantum oscillations in the electrical resistance as a function of magnetic field that depend only on the perpendicular component of the magnetic field. An electric field applied to the back-gate modulates the oscillation frequency. These results demonstrate the presence of two-dimensional electronic states originating from quantum confinement at the $LaAlO_3/SrTiO_3$ interface.

The samples were grown as discussed in Chapter 1 using a deposition temperature of $\sim 650\,^{\circ}$C in $\sim 1 \times 10^{-4}$ mbar of O_2. This lower growth temperature significantly improves the crystalline quality of the films, as observed by X-Ray diffraction and RHEED. The samples are metallic and superconducting. A total of 10 heterostructures have been measured with a thickness of the $LaAlO_3$ top layer between 5 and 10

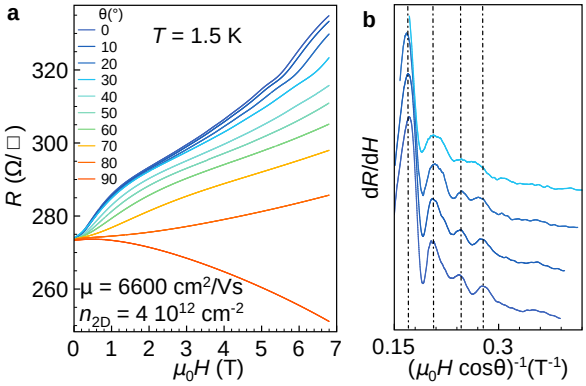

Figure 4.2: Angular dependence of the quantum oscillations. (a) Sheet resistance R as a function of magnetic field H recorded at different orientations (measured by the angle θ) with respect to the direction normal to the substrate. (b) Numerical derivative $\mathrm{d}R/\mathrm{d}H$ as a function of the inverse of the component of the magnetic field perpendicular to the plane of the interface. An offset has been introduced in each curve for clarity. The lines are a guide to the eye.

unit cells, all of which exhibited clear quantum conductance oscillations. Some differences are present in the behavior of the oscillations observed in different samples. In particular the amplitude (and precise shape) of the oscillations varies from sample to sample. In a few samples oscillations are visible directly in the raw magneto-resistance data; in most other samples it is useful to take the derivative of the resistance with respect to the magnetic field –or to remove a background– to make the oscillations fully apparent. Nevertheless, the overall phenomenology that we discuss here is common to the whole set of devices.

Figure 4.1a shows the variation of sheet resistance $\Delta R = R(H) - R(0)$ in response to the application of a magnetic field oriented perpendicular to the interface, recorded at different temperatures. The resistance measurements have been performed using a 4 point AC technique, with a current between 10 and 100 nA, along a transport channel 100 μm wide and 200 μm long, defined by photolithography. Below $T = 7$ K, oscillations superimposed on a positive background are observed for fields larger than 3 T, where the regime $\omega_c\tau > 1$ is attained (with $\mu = 5000\,\mathrm{cm}^2/\mathrm{Vs}$, $\omega_c\tau > 1$ for $\mu_0 H > 2$ T). The numerical derivative of the resistance with respect to magnetic field, presented in Figure 4.1b, reveals that the oscillations are periodic in $1/H$.

The dimensionality of the electronic states can be assessed by examining the angular dependence of the quantum oscillations. Figure 4.2a displays $R(H)$ measured at $T = 1.5$ K on a different sample, for different angles θ. The angle θ measures the inclination of the magnetic field with respect to the normal to the interface at a fixed azimuthal angle. At $\theta = 0°$ the magnetic field is applied perpendicular to the interface, while for $\theta = 90°$ the magnetic field vector lies in the plane of the interface, parallel to the current. At $\theta = 90°$ we observe, consistently with the measurements presented in Chapter 3, a fairly large negative magnetoresistance. Figure 4.2b shows the derivative of the data from 0° to 30° as a function of $(H\cos\theta)^{-1}$. It is appar-

ent that the oscillation depends only on the perpendicular component of the magnetic field. This observation directly indicates that the oscillations arise from closed orbits in momentum space along a two-dimensional Fermi surface.

SdH oscillations represent a direct measurement of the area of the Fermi surface. Indeed, the Onsager relation $\omega = (\phi_0/2\pi^2)A$ establishes a direct proportionality between the cross-sectional area of the Fermi surface normal to the magnetic field, A, and the frequency of the oscillation ω (ϕ_0 is the magnetic flux quantum). Figure 4.3b displays the Fourier transform of the oscillatory component of the magnetoresistance of a sample characterized by a mobility of the order of 3000 cm^2/Vs and a Hall carrier density $n_{2D} = 1.05 \cdot 10^{13}\,cm^{-2}$. A main broad peak is clearly visible in the Fourier transform at 35 T with a shoulder at 50 T. In other samples the shoulder appears as a small secondary peak. The main peak leads to an area of $0.33\,nm^{-2}$, which is only 0.1% of the Brillouin zone. Assuming a circular section of the Fermi surface, we can estimate the carrier density as $n_{2D} = \omega\nu_v\nu_s e/h$, where ν_v and ν_s indicate the valley and spin degeneracy respectively. By taking $\nu_s = 2$ and a single valley we find $n_{2D} = 1.69 \cdot 10^{12}\,cm^{-2}$ (the feature at 50 T would give an additional contribution of $2.4 \cdot 10^{12}\,cm^{-2}$). The corresponding Fermi wavelength is $\lambda_F = 2\pi/k_F = 19\,nm$. This value is larger than the thickness of the electron gas at low temperatures ($\simeq 10\,nm$) estimated in low-mobility samples using the anisotropy of the superconducting critical fields [112], infrared ellipsometry [42] and atomic force microscopy [41, 113]. Apart from the apparent discrepancy between the density values extracted from the Hall effect measurements and the SdH oscillations (which will be discussed later), these findings are consistent with a picture of a two-dimensional electron gas formed by quantum confinement at the $LaAlO_3/SrTiO_3$ interface.

We now turn our attention to the temperature dependence of the oscillations amplitude, which contains important information regarding the carrier effective mass and the level of disorder. For this analysis we performed magnetoresistance measurements up to 15 T and down to 250 mK. The amplitude of the quantum oscillation, extracted from these measurements by subtracting a polynomial background (see Figure 4.3a), decreases with increasing temperature.

The oscillations amplitude ΔR as a function of temperature T can be described by the relation [130]

$$\Delta R(T) = 4R_0 e^{-\alpha T_D}\alpha T/\sinh(\alpha T) \tag{4.8}$$

where $\alpha = 2\pi^2 k_B/\hbar\omega_c$, R_0 is the non-oscillatory component of the square resistance and T_D is the Dingle temperature. The best fit to equation 4.8 of our experimental data, is shown in Figure 4.3c, for the largest maximum of the oscillations (the second largest gives the same result). The fitting parameters are the carrier effective mass (which enters the cyclotron frequency) and the Dingle temperature. We observe a good agreement between theory and experiment with $m^* = 1.45 \pm 0.02\ m_e$ and $T_D = 6\,K$. Our estimation of the effective mass is similar to what has been observed in doped $SrTiO_3$ by quantum oscillations in thin films [129] and by optical conductivity in crystals [13]. We note also that in samples with an order of magnitude larger carrier density, infrared ellipsometry gives an effective mass that is a factor of 2 larger than what we find [42]. Finally, the broadening of the Landau levels, determined by $k_B T_D \sim 0.5\,meV$, is not much smaller than the their energy separation ($\hbar\omega_c \sim 1\,meV$ at 10 T). This explains the small amplitude of the oscillations that we observe.

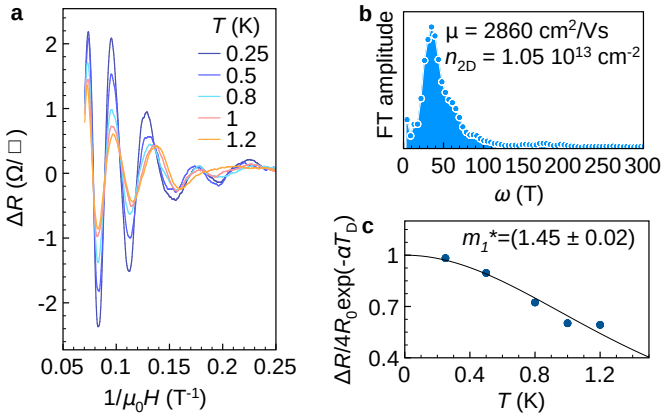

Figure 4.3: Temperature dependence of the Shubnikov-de Haas oscillations. (a) Oscillatory component of the sheet resistance ΔR as a function of the inverse of the magnetic field oriented perpendicular to the $LaAlO_3/SrTiO_3$ interface, recorded at different temperatures T. (b) Fourier spectrum of the resistance oscillation measured at 250 mK. (c) Blue dots: temperature dependence of the amplitude of the oscillation at 13.5 T. Solid line: best fit to equation 4.8 of the experimental data

On some of our samples we have also looked at the evolution of the quantum oscillations in devices equipped with a gate electrode, which consists of a metal layer deposited on the back side of the substrate (0.5 mm thick). Figure 4.4a,b displays $R(H)$ measurements and $\mathrm{d}R/\mathrm{d}H(H^{-1})$ recorded at $T = 250$ mK and different gate voltages V. In conventional two-dimensional electron gases, the main effect of tuning the gate voltage is to modulate the carrier density, leading to a change in the Fermi surface, and thereby in the SdH oscillation frequency. Indeed, as expected, we observe a clear shift of the main peak of the oscillations (see Fig. 4.4c), whose frequency increases linearly with carrier density [1]. In performing these experiments, we also noted that in most devices the oscillations become more apparent at larger gate voltages. This is a consequence of the fact that the mobility increases with V [131] (in the device whose data are shown in Fig. 4.4 the mobility increases from 2400 cm^2/Vs at 10 V to 3600 cm^2/Vs at 120 V).

We conclude that the realization of high-quality $LaAlO_3/SrTiO_3$ interfaces enables us to reveal the presence of discrete two-dimensional sub-bands that manifests themselves in SdH conductance oscillations. One issue that remains to be solved is the apparent mismatch between the values of the carrier density estimated from the Hall effect and from the SdH oscillations (approximately a factor of 4-5 if we consider only the main peak, a factor of 2 if we consider also the peak at 50 T). Apart from the possibility that the limited number of periods observed experimentally may not be sufficient to resolve all peaks in the spectrum of the SdH oscillations, several physical scenarios are also possible. First, even though band-structure calculations predict the presence of only one valley [40] in the conduction band of $LaAlO_3/SrTiO_3$ interfaces, it can-

[1] Interestingly, the smaller secondary peak at $\simeq$ 50 T does not seem to shift significantly with gate voltage

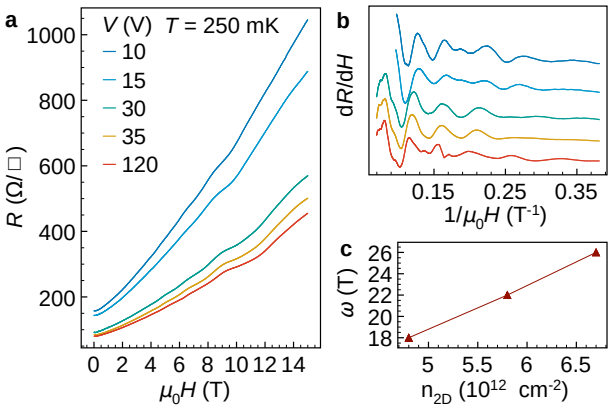

Figure 4.4: Field effect modulation of the Shubnikov-de Haas oscillations. (a) Sheet resistance R as a function of magnetic field H recorded at different gate voltages V at $T = 250$ mK. (b) Numerical derivative $\mathrm{d}R/\mathrm{d}H$ as a function of the inverse of the magnetic field showing the effect of the gate voltage on the resistance oscillations. (c) Main frequency of the oscillation ω as a function of carrier density n_{2D}.

not be excluded that in reality multiple valleys are present. Second, effects associated to the spin of the electrons may be important. On the one hand, a strong spin-orbit interaction is known to affect SdH oscillations [133, 114]. On the other hand, since the effective mass is larger than the free electron mass, the Zeeman splitting is larger than the Landau level spacing even when the gyromagnetic factor is $g = 2$, which brings the system in an unconventional regime. Finally, the different sub-bands occupied by electrons in the 2DEG may originate from different d orbitals, leading to different effective masses, mobility values, and scattering times (which would not fulfill the condition to observe the oscillations) [39]. Additional studies are required to elucidate this point, which most likely will require samples of even higher quality and higher magnetic fields.

The observation of two dimensional sub-bands in $LaAlO_3/SrTiO_3$ interfaces establishes a connection between this system and more conventional semiconducting heterostructures based on III-V compounds. In contrast to these more conventional systems 2DEGs at $LaAlO_3/SrTiO_3$ interfaces are characterized by very strong spin-orbit interaction, much lower Fermi energy, higher effective mass, not to mention the occurrence of superconductivity. The availability of high-quality $LaAlO_3/SrTiO_3$ interfaces give access to two-dimensional electron physics in an entirely unexplored parameter regime, which is likely to disclose new phenomena not yet observed in the diffusive transport limit that has been investigated so far.

Chapter 5

Nanostructuring oxide interfaces

The response of the conductivity to external stimuli is one of the foremost experimental probes available in condensed-matter physics. To perform accurately these measurements a geometric pattern reproducing a transport channel must be defined on the sample. In this Chapter we will discuss the patterning techniques used to fabricate the samples studied in this work. In the first Section a conventional approach borrowed from the microelectronics industry, photolithography, is presented. In the second Section we discuss an innovative approach, based on electron-beam lithography, to fabricate devices whose lateral dimensions are on the scale of the electronic relaxation lengths.

5.1 Photolithography

Photolithography is a process used to transfer a pattern from a mask to a substrate using light. In a nutshell, the procedure is the following. The substrate is covered with a layer of a light-sensitive chemical, called photoresist, using spin coating. A mask reproducing a geometric pattern is interposed between the photoresist and a light source. The exposed area is selectively preserved or removed after a chemical treatment (development). The pattern is then engraved on the substrate typically using chemical etching. The whole process is performed in a clean room.

The resolution of the pattern is limited by the wavelength of the light. The source used in our laboratory is a Hg lamp which delivers UV radiation (intensity $18\,\mathrm{mW/cm^2}$) which allows a resolution of the order of $1\,\mu$m. The resist we used (negative S1813 spin-coated at 4000 RPM for 30 s, thickness $1\,\mu$m) requires $\sim 150\,\mathrm{mJ/cm^2}$ to be transformed, therefore the exposure time is 9 s. The development time is 45 s.

In our experiments the transfer of the pattern from the photoresist to the substrate is based on a lift-off process rather than chemical etching. This approach has the advantage to prevent the creation of defects in the substrate that is often associated with an etching process. After development, a 30 nm thick layer of amorphous $SrTiO_3$ is deposited by room temperature pulsed laser deposition (PLD). The resist is then lifted off using chemical solvents (usually acetone). The last step of the process consists in depositing at high temperature a thin film of $LaAlO_3$ by PLD as discussed in Chapter 1. This thin film grows epitaxially only on the regions of the substrate where the amor-

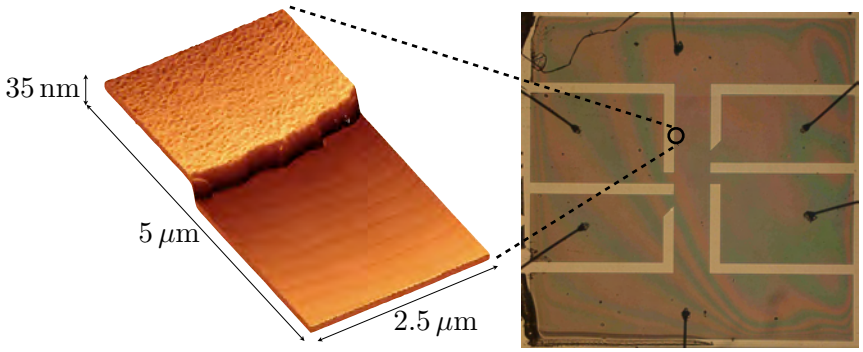

Figure 5.1: Left-hand side: topography of the edge of a pattern created by photolithography measured by atomic force microscopy. The thick and rough region is amorphous $SrTiO_3$. The region where epitaxial $LaAlO_3$ covers the substrate is atomically flat with a step and terrace structure. Right-hand side: optical microscopy image of a pattern used for transport experiments. The image was taken after development of the photoresist.

phous $SrTiO_3$ layer is absent, which are the areas that were covered by the photoresist. In these regions the electron gas is laterally confined.

The edge of a pattern created using this technique is shown in Figure 5.1 where we can distinguish a region where the amorphous $SrTiO_3$ is present (thick and relatively rough) from a region where epitaxial $LaAlO_3$ covers the substrate (atomically flat with a step and terrace structure). A pattern regularly used for transport experiments is depicted in Figure 5.1. The interface is contacted by ultrasonic welding using Al-wires. When performing field effect experiments the metallic gate is a gold film sputtered opposite to the channel area onto the back of the substrate.

5.2 Electron-beam lithography

In devices characterised by a lateral size on the scale of the electronic relaxation lengths mesoscopic phenomena, related to the wave nature of the electrons, become apparent. This field has been extensively studied in III-V semiconductors but remains largely unexplored in oxides. In these materials interfaces give access to low-dimensional electron physics in a new parameter regime (for example in the electron gas present in $LaAlO_3/SrTiO_3$ interfaces we find a large effective mass and dielectric constant, and the occurrence of superconductivity).

In $LaAlO_3/SrTiO_3$ interfaces the electron mean free path and the superconducting coherence length are of the order of 100 nm. Unfortunately photolithography performed with conventional UV lamps does not provide the necessary resolution to reach this limit. There is therefore a strong need to develop a more refined lithographic technique. An interesting innovative approach based on atomic force microscopy was proposed recently [134, 135]. In this work we will discuss a more established lithographic technique that allows us to explore the nanoscale: electron-beam lithography. The working principle is very similar to conventional photolithography, only an elec-

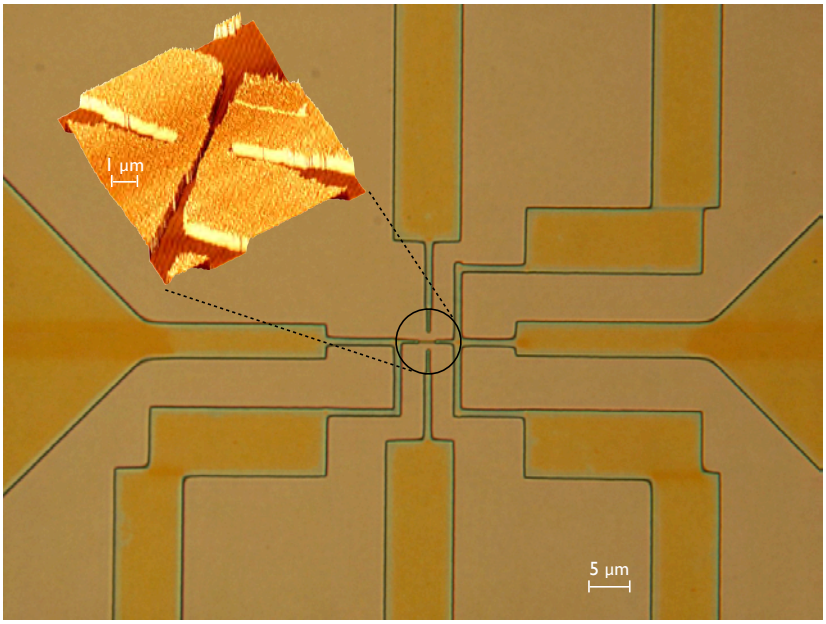

Figure 5.2: Optical microscopy image of a device fabricated by electron-beam lithography. The image was taken after development of the resist. Inset: detail of the highlighted region measured by atomic force microscopy after the deposition of $LaAlO_3$.

tron beam replaces light. At a technical level this requires a number of refinements, such as the use of vacuum technology, electrostatic optics, nanoscale positioning and the replacement of the photoresist with an electron-beam sensitive resist. Moreover, when dealing with insulating substrates, electron-beam lithography faces the challenge of avoiding electrostatic charging of the surface. In this work we solved this problem using a negative resist, mr-EBL 6000 (produced by Micro Resist Technology), that requires a very small electron dose - exposure time ($\sim 10\,\mu$C/cm^2) with respect to more common resists such as PMMA.

A resist layer 100 nm thick is deposited on the surface of a TiO_2-terminated $SrTiO_3$ single crystal by spin coating (3000 RPM during 30 s, thickness 100 nm) and baked in a hot plate for 3 minutes at 110 °C. The exposure is performed using a Raith 50 system (27 kV, LaB_6 filament, dose $10\,\mu$C/cm^2). The sample is then baked on a hot plate (5 minutes at 110 °C) and developed for 30 s. Once the pattern is transferred to the resist, we proceed as discussed for photolithography.

Figure 5.2 shows optical and atomic force microscopy images of the pattern we fabricated. It consists of a thin channel ($\sim$100 nm wide and 2 μm long) connected to 3 voltage probes and equipped with 2 side-gate electrodes. The separation between the side-gates electrodes and the channel is $< 1\,\mu$m. In Figure 5.3 the nanoscale region measured in two different devices is shown. The orientation of the step and terrace structure of the epitaxial $LaAlO_3$ layer is different in the two devices. In one device the channel is perpendicular to the steps while in the other one the channel is parallel to the steps.

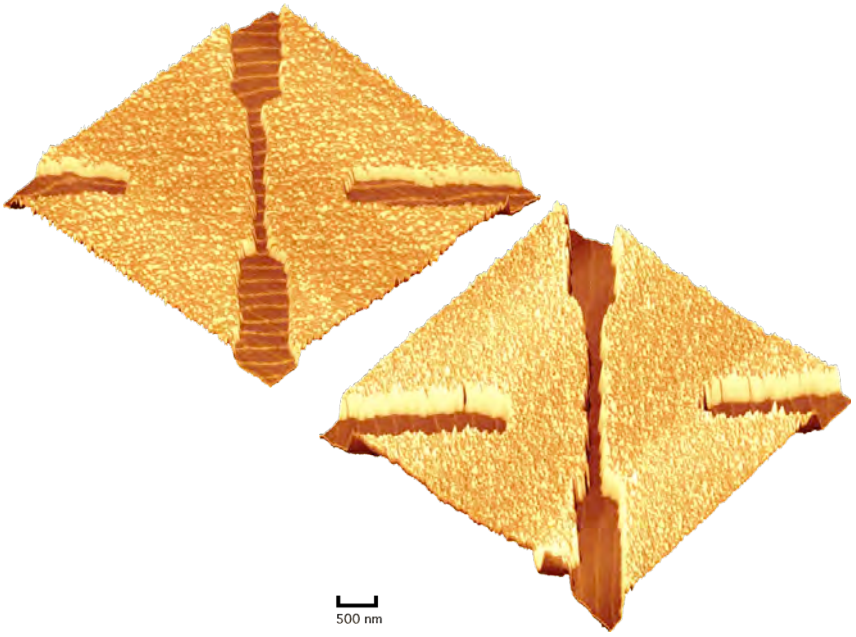

Figure 5.3: Topography of a transport channel in its nanoscale region measured by atomic force microscopy. Left-hand side: channel perpendicular to the steps. Right-hand side: channel parallel to the steps. The height of the amorphous $SrTiO_3$ layer is 20 nm.

5.3 Field-effect devices

We will now turn our attention to some preliminary results regarding transport experiments in nanoscale devices. Unfortunately, none of the devices studied so far have had a functioning non-shorted side-gate electrode. Therefore the devices were equipped with a back-gate electrode. Interestingly, the devices exhibit a very large response to the application of a gate voltage. In Figure 5.4 the sheet resistance of the nanoscale channel as a function of back gate voltage measured at $T = 1.5\,\mathrm{K}$ is compared to the same measurement performed on a large channel ($300 \times 200\ \mu\mathrm{m}^2$). The resistance was measured using both 4 point AC and DC technique with a current of 10 nA. Although the general shape of the curve is similar, the nanoscale device exhibits a large enhancement of the field effect. No dependence on the orientation of the channel with respect to the steps was observed.

We are now in the position to study the modulation of the superconducting state brought about by the electric field effect, discussed in the context of large samples in Chapter 2, in devices where the lateral confinement is comparable to the superconducting coherence length. Fig. 5.5 shows the sheet resistance versus temperature for applied gate voltages between -100 V and 100 V measured on the sample whose topography is shown on the left-hand side of Figure 5.3. In the same Figure the critical temperature, defined as the temperature at which the sheet resistance is 50% of $R(T = 400\,\mathrm{mK})$ as a function of gate voltage is shown, together with $R(T = 400\,\mathrm{mK}, V)$. We observe a large modulation of the superconducting state with a number of key differences with respect to the large samples. First of all, a complete

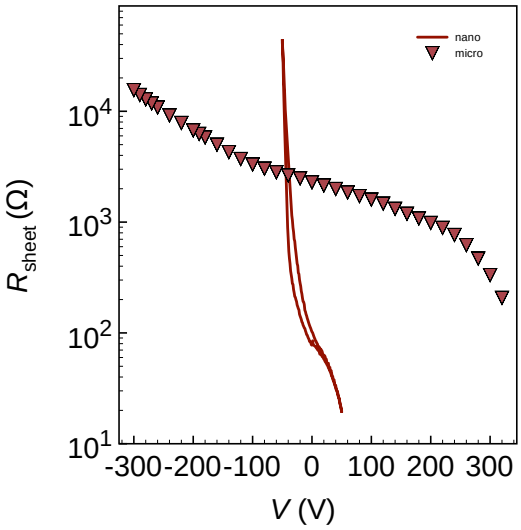

Figure 5.4: Sheet resistance as a function of back-gate voltage measured in a nanoscale device (100 nm×2 μm, continuous line) and in a large device (300 μm)×200 μm, triangles).

transition towards a state characterised by a resistance smaller than the measurement limit is observed only for one gate voltage, which corresponds to the highest critical temperature ($T_{c\,50\%} = 148$ mK, $V = 40$ V). Second, an abrupt suppression of the superconducting state is observed as the gate voltage is reduced from the value corresponding to optimal doping. By comparing the (T, V) phase diagram depicted in Figure 5.5 with the one mapped in the large samples, we remark the absence of an underdoped regime in nanoscale devices and a low critical temperature. Third, the gate voltage dependence of the resistance measured at $T = 400$ mK is markedly different, being very rapid above the superconducting ground state and much slower in the non-superconducting region of the phase diagram. This behaviour is the opposite to the one observed in large samples [1]. A theoretical interpretation of this phenomenology is lacking at the moment. The absence of a complete superconducting transition points to a different fluctuation regime which could be related to the presence of thermally activated [136, 137] and quantum [138] phase slips. A systematic study of the superconducting transitions in wires of different width is necessary to clarify this point.

[1] The fact that we observe a weaker dependence of the resistance on gate voltage at 400 mK with respect to the measurement at 1.5 K shown in Figure 5.4 could be an extrinsic effect caused by the dielectric aging of the substrate.

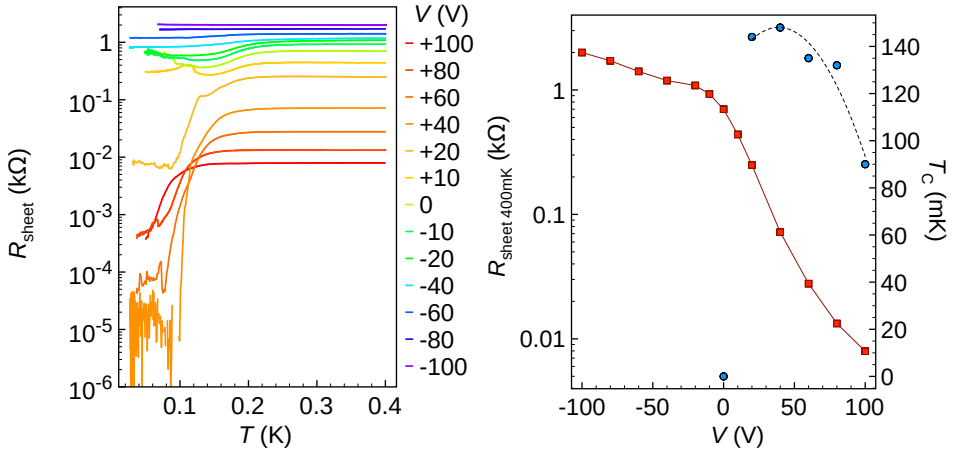

Figure 5.5: Left-hand side: sheet resistance R_{sheet} as a function of temperature T measured for different gate voltages V. Right-hand side: critical temperature T_{c}, defined as the temperature at which the sheet resistance is 50% of $R(T = 400\,\text{mK})$ as a function of gate voltage (blue circles). $R(T = 400\,\text{mK})$ as a function of gate voltage (red squares).

Conclusions

Summary

In this thesis we have studied the electronic properties of a novel two-dimensional electron gas. We have considered the interface between the semiconductor $SrTiO_3$ and the band insulator $LaAlO_3$, where metallic conduction is observed. The vast majority of the samples used in this study were fabricated in our laboratory. We have carefully analysed the role of fabrication conditions in determining the electronic properties of the interface. These studies resulted in an optimisation of the growth parameters and helped us to avoid pitfalls such as the delocalisation of carriers in the substrate.

Since this electron gas is hosted in a material endowed with rich electronic properties, new interesting phenomena are expected to occur. In this thesis we have shown that this interface becomes superconducting at temperatures lower than 300 mK. The temperature dependence of the critical magnetic fields indicates that the superconducting sheet is two-dimensional with a thickness of about 10 nm. We have highlighted that the superconducting transition can be interpreted in terms of thermal generation of free vortices, as expected in the two-dimensional limit. Another landmark of two-dimensional superconductivity is a quantum phase transition towards an insulating state traditionally tuned either by increasing the level of disorder or by applying magnetic fields. We have explored this phenomenon using either magnetic and electric fields. Indeed, the application of the field-effect transistor principle to novel electronic systems provides a fascinating opportunity to control their properties and ultimately their ground state. Using this approach we have uncovered a phase diagram characterised by a quantum critical point separating a superconducting pocket from a localised phase. The quantum phase transition occurs at a critical sheet resistance close to the quantum of resistance for Cooper pairs. The superconducting critical temperature is tuned by the gate voltage from an underdoped to an overdoped regime.

Of particular relevance for the understanding of the nature of this electronic system is the insulating region of the phase diagram. We have highlighted a quantum correction to the conductivity, known as weak localisation, that emerges from electron interference effects and drives a non-interacting two-dimensional system with an arbitrarily small concentration of impurities towards an insulating ground state. We have observed a characteristic dependence of the conductivity on temperature and magnetic field pointing to this localisation mechanism.

We have also emphasised that in this context the spin-orbit interaction, an outstanding manifestation of special relativity in quantum mechanics, plays a pivotal role. At an interface a breaking of inversion symmetry naturally occurs which brings about the

presence of strong electric fields. Indeed, the large local polar distorsion that $SrTiO_3$ exhibits at this interface attests to the relevance of this phenomenon. We have shown that the quantum conductivity correction arising from electron interference can promote carrier delocalisation rather than localisation if a sufficiently strong spin-orbit interaction is present. The effect is decisive in two-dimensional systems, where a metal to insulator transition can be driven. We have assessed the influence of the spin-orbit interaction on the electronic properties of this system by measuring the magnetoconductance in the diffusive regime. We have shown that the spin-orbit interaction can be tuned by applying an external gate voltage. We also discussed a remarkable correlation between the onset of a strong spin-orbit interaction and the emergence of superconductivity. The spin relaxation time displays a characteristic behaviour associated with the breaking of inversion symmetry.

We have also studied samples characterised by mobilities sufficiently large to observe well defined Landau levels in magnetic fields of the order of a few Tesla. We have presented quantum oscillations in the electrical resistance as a function of magnetic field that depend only on the perpendicular component of the magnetic field. These results demonstrate the presence of two-dimensional electronic states originating from quantum confinement. A positive gate voltage increases the mobility, the carrier density and the oscillation frequency. The frequency of the oscillations signals a multiple sub-bands occupation in the quantum well or a multiple valley configuration. Since the carrier effective mass, as extracted from the temperature dependence of the oscillation amplitude, is larger than the free electron mass, the Zeeman splitting is larger than the Landau level spacing. This is an unconventional regime that was not explored in semiconducting heterostructures based on III-V compounds.

Finally we have discussed an innovative approach, based on electron-beam lithography, to fabricate devices whose lateral dimensions are on the scale of the electron mean free path and the superconducting coherence length, both of the order of 100 nm. In these preliminary studies we have observed a large modulation of the superconducting state.

Perspectives

The experimental results we have discussed stimulate several interesting questions concerning the rich phase diagram we began to unveil. Does the quantum critical point separating the superconducting from the insulating phase coincide with the one pertaining to the metal to insulator transition? Some experimental evidence seem to indicate that in the underdoped regime close to the critical point a magnetic field drives the system in an insulating phase while deep in the overdoped region of the phase diagram a magnetic field leads to a superconductor to metal phase transition. Once the existence of two distinct critical points is firmly established it would be interesting to track their position in samples characterised by different levels of disorder. Can we drive a transition towards strong localisation using the electrostatic field effect? If the answer is positive, does the system exhibit the colossal magnetoresponse observed in highly disordered two-dimensional superconductors? What is the driving force behind the decrease in critical temperature observed in the overdoped regime? Can we observe a field effect modulation of superconductivity in samples exhibiting

quantum oscillations of the conductance? We have shown that the energy scale associated with the spin-orbit interaction is of the order of the Fermi energy. How does this affect the superconducting state? Is it described by an unconventional order parameter as some theorerical studies suggest? To answer this question it would be very useful to fabricate tunnel junctions and to measure the density of states. One interesting approach is to push further the development of nanoscale devices, either using electron beam lithography as described here or with other techniques. A quantum point contact realised in this system could serve as a tunable Josephson junction and shed light on these issues. More generally speaking using the electrostatic control of superconductivity, new quantum electronic devices can be envisaged. We also discussed presence of two-dimensional electronic states originating from quantum confinement by measuring conductance oscillations. Access to higher magnetic fields and lower temperatures will be useful to resolve the apparent mismatch between the values of the carrier density estimated from the Hall effect and from the frequency of the oscillations and to fully characterise the Fermi surface of this system.

Acknowledgements

First of all I wish to express my gratitude to Prof. Triscone for giving me the opportunity of working in his group. I have found his support to be invaluable and his optimism and enthusiasm have contributed to a positive and creative working environment.

I owe thanks to Prof. Harold Y. Hwang, Prof. Christian Bernhard and Prof. Øystein Fischer for playing a vital role in the examination of this work.

I would like to take this opportunity to thank everyone in the group Triscone for their encouragement and constant support during the last four years, with a special mention to Stefano Gariglio, Claudia Cancellieri, Nicolas Reyren and Alexandre Fête, who were fundamental in the production of my thesis.

During these years I have also had the pleasure of collaborating with Prof. Didier Jaccard, Prof. Jochen Mannhart, Prof. Marc Gabay, Prof. Toni Schneider, Prof. Alberto Morpurgo, Stefan Thiel, Benjamin Sacépé, Nuno Couto Guimaraes. These are acknowledged as having given a valued contribution to this work.

My research has benefited from several scientific discussions and collaborations over the years and for this I must thank Prof. Thierry Giamarchi, Prof. Dirk van der Marel, Prof. Patrycja Paruch, Prof. Markus Muller, Prof. Matthew Dawber, Prof. Rolf Lortz, Manuel Bibes, Pavlo Zubko, Marta Gibert, Celine Lichtensteiger, Almudena Torres, Jill Guyonnet, Alessia Sambri, Raoul Scherwiztl, Daniel Matthey, Gijsbert Rispens, Hajo Molegraaf, Pablo Pedrazzini, Anna-Sabina Ruetschi, Nicolas Stucki, Christoph Berthod, Lara Benfatto, Gabriel Seyfarth, Daniele Marré, Ilaria Pallecchi, Luca Pellegrino and Emilio Bellingeri.

I would not have have come this far without the technical assistance of Spiros Zanos, Renald Cartoni, Marco Lopes and Patrick Magnin.

I would like to thank the administration team, Esther Schwarz, Nicole Nguyen and Liliane Dujourdil for their hard work.

Vorrei ringraziare i miei genitori, Gino e Laura, per il sostegno che non mi hanno mai fatto mancare durante i miei studi, e mia sorella Silvia. E soprattutto vorrei ringraziare la mia sposa, Roya, senza la quale sarei perduto.

References

[1] Dagotto, E. *Science* **318**(5853), 1076–1077 (2007).

[2] Cardona, M. *Phys. Rev.* **140**(2A), A651–A655 Oct (1965).

[3] Spinelli, A., Torija, M. A., Liu, C., Jan, C., and Leighton, C. *Phys. Rev. B* **81**(15), 155110 Apr (2010).

[4] Koonce, C. S., Cohen, M. L., Schooley, J. F., Hosler, W. R., and Pfeiffer, E. R. *Phys. Rev.* **163**(2), 380–390 Nov (1967).

[5] Mattheiss, L. F. *Phys. Rev. B* **6**(12), 4740–4753 Dec (1972).

[6] Meevasana, W., Zhou, X. J., Moritz, B., Chen, C.-C., He, R. H., Fujimori, S.-I., Lu, D. H., Mo, S.-K., Moore, R. G., Baumberger, F., Devereaux, T. P., van der Marel, D., Nagaosa, N., Zaanen, J., and Shen, Z.-X. *New Journal of Physics* **12**(2), 023004 (2010).

[7] Lytle, F. W. *Journal of Applied Physics* **35**(7), 2212–2215 (1964).

[8] Kityk, A. V., Schranz, W., Sondergeld, P., Havlik, D., Salje, E. K. H., and Scott, J. F. *Phys. Rev. B* **61**(2), 946–956 Jan (2000).

[9] Müller, K. A. and Burkard, H. *Phys. Rev. B* **19**(7), 3593–3602 Apr (1979).

[10] Zhong, W. and Vanderbilt, D. *Phys. Rev. B* **53**(9), 5047–5050 Mar (1996).

[11] Barrett, J. H. *Phys. Rev.* **86**(1), 118–120 Apr (1952).

[12] Hemberger, J., Lunkenheimer, P., Viana, R., Böhmer, R., and Loidl, A. *Phys. Rev. B* **52**(18), 13159–13162 Nov (1995).

[13] van Mechelen, J. L. M., van der Marel, D., Grimaldi, C., Kuzmenko, A. B., Armitage, N. P., Reyren, N., Hagemann, H., and Mazin, I. I. *Physical Review Letters* **100**(22), 226403 (2008).

[14] Mitsui, T. and Westphal, W. B. *Phys. Rev.* **124**(5), 1354–1359 Dec (1961).

[15] Jang, H. W., Kumar, A., Denev, S., Biegalski, M. D., Maksymovych, P., Bark, C. W., Nelson, C. T., Folkman, C. M., Baek, S. H., Balke, N., Brooks, C. M., Tenne, D. A., Schlom, D. G., Chen, L. Q., Pan, X. Q., Kalinin, S. V., Gopalan, V., and Eom, C. B. *Phys. Rev. Lett.* **104**(19), 197601 May (2010).

[16] Biegalski, M. D., Jia, Y., Schlom, D. G., Trolier-McKinstry, S., Streiffer, S. K., Sherman, V., Uecker, R., and Reiche, P. *Applied Physics Letters* **88**(19), 192907 (2006).

[17] Kim, Y. S., Kim, D. J., Kim, T. H., Noh, T. W., Choi, J. S., Park, B. H., and Yoon, J.-G. *Applied Physics Letters* **91**(4), 042908 (2007).

[18] Itoh, M., Wang, R., Inaguma, Y., Yamaguchi, T., Shan, Y.-J., and Nakamura, T. *Phys. Rev. Lett.* **82**(17), 3540–3543 Apr (1999).

[19] Fleury, P. A. and Worlock, J. M. *Phys. Rev.* **174**(2), 613–623 Oct (1968).

[20] Haeni, J. H., Irvin, P., Chang, W., Uecker, R., Reiche, P., Li, Y. L., Choudhury, S., Tian, W., Hawley, M. E., Craigo, B., Tagantsev, A. K., Pan, X. Q., Streiffer, S. K., Chen, L. Q., Kirchoefer, S. W., Levy, J., and Schlom, D. G. *Nature* **430**(7001), 758–761 08 (2004).

[21] Warusawithana, M. P., Cen, C., Sleasman, C. R., Woicik, J. C., Li, Y., Kourkoutis, L. F., Klug, J. A., Li, H., Ryan, P., Wang, L.-P., Bedzyk, M., Muller, D. A., Chen, L.-Q., Levy, J., and Schlom, D. G. *Science* **324**(5925), 367–370 4 (2009).

[22] Ohtomo, A. and Hwang, H. Y. *Nature* **427**(6973), 423–426 (2004).

[23] Kawasaki, M., Takahashi, K., Maeda, T., Tsuchiya, R., Shinohara, M., Ishiyama, O., Yonezawa, T., Yoshimoto, M., and Koinuma, H. *Science* **266**(5190), 1540–1542 (1994).

[24] Nakagawa, N., Hwang, H. Y., and Muller, D. A. *Nat Mater* **5**(3), 204–209 (2006).

[25] Chen, H., Kolpak, A. M., and Ismail-Beigi, S. *Phys. Rev. B* **79**(16), 161402 Apr (2009).

[26] Hesper, R., Tjeng, L. H., Heeres, A., and Sawatzky, G. A. *Phys. Rev. B* **62**(23), 16046–16055 Dec (2000).

[27] Cappus, D., Haflel, M., Neuhaus, E., Heber, M., Rohr, F., and Freund, H. J. *Surface Science* **337**(3), 268 – 277 (1995). Surface Reconstruction: Structure and Dynamics.

[28] Harrison, W. A., Kraut, E. A., Waldrop, J. R., and Grant, R. W. *Phys. Rev. B* **18**(8), 4402–4410 Oct (1978).

[29] Nishimura, J., Ohtomo, A., Ohkubo, A., Murakami, Y., and Kawasaki, M. *Japanese Journal of Applied Physics* **43**(8A), L1032–L1034 (2004).

[30] Thiel, S., Hammerl, G., Schmehl, A., Schneider, C. W., and Mannhart, J. *Science* **313**(5795), 1942–1945 (2006).

[31] Herranz, G., Basletic, M., Bibes, M., Carretero, C., Tafra, E., Jacquet, E., Bouzehouane, K., Deranlot, C., Hamzic, A., Broto, J.-M., Barthelemy, A., and Fert, A. *Physical Review Letters* **98**(21), 216803 (2007).

[32] Kalabukhov, A., Gunnarsson, R., Borjesson, J., Olsson, E., Claeson, T., and Winkler, D. *Physical Review B (Condensed Matter and Materials Physics)* **75**(12), 121404 (2007).

[33] Siemons, W., Koster, G., Yamamoto, H., Harrison, W. A., Lucovsky, G., Geballe, T. H., Blank, D. H. A., and Beasley, M. R. *Physical Review Letters* **98**(19), 196802 (2007).

[34] Willmott, P. R., Pauli, S. A., Herger, R., Schleputz, C. M., Martoccia, D., Patterson, B. D., Delley, B., Clarke, R., Kumah, D., Cionca, C., and Yacoby, Y. *Physical Review Letters* **99**(15), 155502 (2007).

[35] Salluzzo, M., Cezar, J. C., Brookes, N. B., Bisogni, V., De Luca, G. M., Richter, C., Thiel, S., Mannhart, J., Huijben, M., Brinkman, A., Rijnders, G., and Ghiringhelli, G. *Phys. Rev. Lett.* **102**(16), 166804 Apr (2009).

[36] Brinkman, A., Huijben, M., van Zalk, M., Huijben, J., Zeitler, U., Maan, J. C., van der Wiel, W. G., Rijnders, G., Blank, D. H. A., and Hilgenkamp, H. *Nat Mater* **6**(7), 493–496 (2007).

[37] Jia, C. L., Lentzen, M., and Urban, K. *Science* **299**(5608), 870–873 2 (2003).

[38] Jia, C. L., Mi, S. B., Faley, M., Poppe, U., Schubert, J., and Urban, K. *Phys. Rev. B* **79**(8), 081405 Feb (2009).

[39] Son, W.-j., Cho, E., Lee, B., Lee, J., and Han, S. *Phys. Rev. B* **79**(24), 245411 Jun (2009).

[40] Popović, Z. S., Satpathy, S., and Martin, R. M. *Phys. Rev. Lett.* **101**(25), 256801 Dec (2008).

[41] Basletic, M., Maurice, J. L., Carretero, C., Herranz, G., Copie, O., Bibes, M., Jacquet, E., Bouzehouane, K., Fusil, S., and Barthelemy, A. *Nat Mater* **7**(8), 621–625 (2008).

[42] Dubroka, A., Rössle, M., Kim, K. W., Malik, V. K., Schultz, L., Thiel, S., Schneider, C. W., Mannhart, J., Herranz, G., Copie, O., Bibes, M., Barthélémy, A., and Bernhard, C. *Phys. Rev. Lett.* **104**(15), 156807 Apr (2010).

[43] Sing, M., Berner, G., Goß, K., Müller, A., Ruff, A., Wetscherek, A., Thiel, S., Mannhart, J., Pauli, S. A., Schneider, C. W., Willmott, P. R., Gorgoi, M., Schäfers, F., and Claessen, R. *Phys. Rev. Lett.* **102**(17), 176805 Apr (2009).

[44] Bell, C., Harashima, S., Hikita, Y., and Hwang, H. Y. *Applied Physics Letters* **94**(22), 222111 (2009).

[45] Yamada, H. and Miller, G. R. *Journal of Solid State Chemistry* **6**(1), 169 – 177 (1973).

[46] Chan, N. H., Sharma, R. K., and Smyth, D. M. *Journal of The Electrochemical Society* **128**(8), 1762–1769 (1981).

[47] Landau, L. and Lifshitz, E. M. *Course of Theoretical Physics*, volume 5. Pergamon Press, (1980).

[48] Wilson, K. G. *Rev. Mod. Phys.* **47**(4), 773–840 Oct (1975).

[49] Sachdev, S. *Quantum Phase Transitions*. Cambridge University Press, (1999).

[50] Sondhi, S. L., Girvin, S. M., Carini, J. P., and Shahar, D. *Rev. Mod. Phys.* **69**(1), 315–333 Jan (1997).

[51] Vojta, M. *Reports on Progress in Physics* **66**(12), 2069 (2003).

[52] Schneider, T. and Singer, J. M. *Phase Transition Approach to High Temperature Superconductivity*. Imperial College Press, London, (2000).

[53] Feynman, R. P. *Rev. Mod. Phys.* **20**(2), 367–387 Apr (1948).

[54] Chaikin, P. and Lubensky, T. *Principles of condensed matter physics*. Cambridge University Press, (1995).

[55] Mermin, N. D. and Wagner, H. *Phys. Rev. Lett.* **17**(22), 1133–1136 Nov (1966).

[56] Coleman, S. *Communications in Mathematical Physics* **31**(4), 259–264 12 (1973).

[57] Berezinskii, V. *Zh. Eksp. Teor. Fiz.* **61**, 1144 (1971).

[58] Berezinskii, V. *Sov. Phys. JETP* **34**, 610 (1971).

[59] Kosterlitz, J. and Thouless, D. *J. Phys. C* **5**, L124 (1972).

[60] Nelson, D. R. and Kosterlitz, J. M. *Phys. Rev. Lett.* **39**(19), 1201–1205 Nov (1977).

[61] Rudnick, I. *Phys. Rev. Lett.* **40**(22), 1454–1455 May (1978).

[62] Bishop, D. J. and Reppy, J. D. *Phys. Rev. Lett.* **40**(26), 1727–1730 Jun (1978).

[63] Pearl, J. In *Low Temperature Physics-LT9,* Daunt, J. G., Edwards, D. O., Milford, F. J., and Yaqub, M., editors, 566. Plenum, New York, (1965).

[64] Beasley, M. R., Mooij, J. E., and Orlando, T. P. *Phys. Rev. Lett.* **42**(17), 1165–1168 Apr (1979).

[65] Finkel'stein, A. *JETP Letters* **45**, 46 (1987).

[66] Finkel'stein, A. *Physica B* **197**, 636 (1994).

[67] Fisher, M. P. A., Grinstein, G., and Girvin, S. M. *Phys. Rev. Lett.* **64**(5), 587–590 Jan (1990).

[68] Fisher, M. P. A. *Phys. Rev. Lett.* **65**(7), 923–926 Aug (1990).

[69] Abrahams, E., Anderson, P. W., Licciardello, D. C., and Ramakrishnan, T. V. *Phys. Rev. Lett.* **42**(10), 673–676 Mar (1979).

[70] Haviland, D. B., Liu, Y., and Goldman, A. M. *Phys. Rev. Lett.* **62**(18), 2180–2183 May (1989).

[71] Markovic, N., Christiansen, C., Mack, A., and Goldman, A. *Phys. stat. sol. (b)* **218**, 221 (2000).

[72] Gabay, M. and Kapitulnik, A. *Phys. Rev. Lett.* **71**(13), 2138–2141 Sep (1993).

[73] Schneider, T., Caviglia, A. D., Gariglio, S., Reyren, N., and Triscone, J.-M. *Phys. Rev. B* **79**(18), 184502 May (2009).

[74] Benfatto, L., Castellani, C., and Giamarchi, T. *Phys. Rev. B* **80**(21), 214506 Dec (2009).

[75] Ahn, C. H., Triscone, J. M., and Mannhart, J. *Nature* **424**(6952), 1015–1018 (2003).

[76] Ahn, C. H., Bhattacharya, A., Ventra, M. D., Eckstein, J. N., Frisbie, C. D., Gershenson, M. E., Goldman, A. M., Inoue, I. H., Mannhart, J., Millis, A. J., Morpurgo, A. F., Natelson, D., and Triscone, J.-M. *Reviews of Modern Physics* **78**(4), 1185 (2006).

[77] Mannhart, J., Bednorz, J. G., MâĹŽÂžller, K. A., and Schlom, D. G. *Zeitschrift fâĹŽÂžr Physik B Condensed Matter* **83**(3), 307–311 10 (1991).

[78] Ahn, C. H., Tybell, T., Antognazza, L., Char, K., Hammond, R. H., Beasley, M. R., Fischer, O., and Triscone, J. M. *Science* **276**(5315), 1100–1103 5 (1997).

[79] Salluzzo, M., Cassinese, A., De Luca, G. M., Gambardella, A., Prigiobbo, A., and Vaglio, R. *Phys. Rev. B* **70**(21), 214528 Dec (2004).

[80] Cassinese, A., Luca, G. M. D., Prigiobbo, A., Salluzzo, M., and Vaglio, R. *Applied Physics Letters* **84**(19), 3933–3935 (2004).

[81] Parendo, K. A., Tan, K. H. S. B., Bhattacharya, A., Eblen-Zayas, M., Staley, N. E., and Goldman, A. M. *Physical Review Letters* **94**(19), 197004 (2005).

[82] Tanaka, H., Zhang, J., and Kawai, T. *Phys. Rev. Lett.* **88**(2), 027204 Dec (2001).

[83] Hong, X., Posadas, A., Lin, A., and Ahn, C. H. *Phys. Rev. B* **68**(13), 134415 Oct (2003).

[84] Sundar, V. C., Zaumseil, J., Podzorov, V., Menard, E., Willett, R. L., Someya, T., Gershenson, M. E., and Rogers, J. A. *Science* **303**(5664), 1644–1646 3 (2004).

[85] Matthey, D., Gariglio, S., and Triscone, J.-M. *Applied Physics Letters* **83**(18), 3758–3760 (2003).

[86] Christen, H.-M., Mannhart, J., Williams, E. J., and Gerber, C. *Phys. Rev. B* **49**(17), 12095–12104 May (1994).

[87] Schneider, T. *The Physics of Superconductors*, volume 2, 111. Springer, Berlin, (2004).

[88] Schneider, T. *Acta Physica Polonica A* **91**, 203 (1997).

[89] Aubin, H., Marrache-Kikuchi, C. A., Pourret, A., Behnia, K., Berge, L., Dumoulin, L., and Lesueur, J. *Physical Review B (Condensed Matter and Materials Physics)* **73**(9), 094521 (2006).

[90] Hebard, A. F. and Paalanen, M. A. *Phys. Rev. Lett.* **65**(7), 927–930 Aug (1990).

[91] Yazdani, A., White, W. R., Hahn, M. R., Gabay, M., Beasley, M. R., and Kapitulnik, A. *Phys. Rev. Lett.* **70**(4), 505–508 Jan (1993).

[92] Yazdani, A. and Kapitulnik, A. *Phys. Rev. Lett.* **74**(15), 3037–3040 Apr (1995).

[93] Sacépé, B., Chapelier, C., Baturina, T. I., Vinokur, V. M., Baklanov, M. R., and Sanquer, M. *Phys. Rev. Lett.* **101**(15), 157006 Oct (2008).

[94] Das, D. and Doniach, S. *Phys. Rev. B* **57**(22), 14440–14443 Jun (1998).

[95] Gantmakher, V. F. and Dolgopolov, V. T. *Physics-Uspekhi* **53**(1), 1 (2010).

[96] Berthod, C. *Applications of the Many-Body Formalism in Condensed-Matter Physics*. Lecture Notes, University of Geneva, (2009).

[97] Bruus, H. and Flensberg, K. *Many-Body Quantum Theory in Condensed Matter Physics*. Oxford University Press, (2004).

[98] Akkermans, E. and Montambaux, G. *Mesoscopic Physics of Electrons and Photons*. Cambridge University Press, (2007).

[99] Bychkov, Y. A. and Rashba, E. I. *Journal of Physics C: Solid State Physics* **17**(33), 6039–6045 (1984).

[100] Winkler, R. *Spin–Orbit Coupling Effects in Two-Dimensional Electron and Hole Systems* , 69–130 (2003).

[101] Zutic, I., Fabian, J., and Sarma, S. D. *Reviews of Modern Physics* **76**(2), 323 (2004).

[102] Elliott, R. J. *Phys. Rev.* **96**(2), 266–279 Oct (1954).

[103] Yafet, Y. *Solid State Phys.* **14**, 1 (1963).

[104] Bergman, G. *Phys. Rev. Lett.* **48**(15), 1046–1049 Apr (1982).

[105] Hikami, S., Larkin, A. I., and Nagaoka, Y. *Progress of Theoretical Physics* **63**(2), 707–710 (1980).

[106] Maekawa, S. and Fukuyama, H. *Journal of the Physical Society of Japan* **50**(8), 2516–2524 (1981).

[107] Lee, P. A. and Ramakrishnan, T. V. *Rev. Mod. Phys.* **57**(2), 287–337 Apr (1985).

[108] Anderson, P. W. *Phys. Rev.* **109**(5), 1492–1505 Mar (1958).

[109] Al'tshuler, B. L. and Aronov, A. G. *Sov. Phys. JETP* **50**, 968 (1979).

[110] Punnoose, A. and Finkel'stein, A. M. *Science* **310**(5746), 289–291 (2005).

[111] Anissimova, S., Kravchenko, S. V., Punnoose, A., Finkel/'stein, A. M., and Klapwijk, T. M. *Nat Phys* **3**(10), 707–710 10 (2007).

[112] Reyren, N., Gariglio, S., Caviglia, A. D., Jaccard, D., Schneider, T., and Triscone, J.-M. *Applied Physics Letters* **94**(11), 112506 (2009).

[113] Copie, O., Garcia, V., Bodefeld, C., Carretero, C., Bibes, M., Herranz, G., Jacquet, E., Maurice, J.-L., Vinter, B., Fusil, S., Bouzehouane, K., Jaffres, H., and Barthelemy, A. *Physical Review Letters* **102**(21), 216804 (2009).

[114] Nitta, J., Akazaki, T., Takayanagi, H., and Enoki, T. *Phys. Rev. Lett.* **78**(7), 1335–1338 Feb (1997).

[115] Miller, J. B., Zumbühl, D. M., Marcus, C. M., Lyanda-Geller, Y. B., Goldhaber-Gordon, D., Campman, K., and Gossard, A. C. *Phys. Rev. Lett.* **90**(7), 076807 Feb (2003).

[116] Ueno, K., Nakamura, S., Shimotani, H., Ohtomo, A., Kimura, N., Nojima, T., Aoki, H., Iwasa, Y., and Kawasaki, M. *Nat Mater* **7**(11), 855–858 11 (2008).

[117] Bergmann, G. *Physics Reports* **107**(1), 1–58 (1984).

[118] Punnoose, A. *Applied Physics Letters* **88**(25), 252113 (2006).

[119] Caviglia, A. D., Gariglio, S., Reyren, N., Jaccard, D., Schneider, T., Gabay, M., Thiel, S., Hammerl, G., Mannhart, J., and Triscone, J. M. *Nature* **456**(7222), 624–627 12 (2008).

[120] Ivchenko, E. L., Kiselev, A. A., and Willander, M. *Solid State Communications* **102**(5), 375 – 378 (1997).

[121] Salis, G., Kato, Y., Ensslin, K., Driscoll, D. C., Gossard, A. C., and Awschalom, D. D. *Nature* **414**(6864), 619–622 12 (2001).

[122] Papadakis, S. J., De Poortere, E. P., Manoharan, H. C., Shayegan, M., and Winkler, R. *Science* **283**(5410), 2056–2058 3 (1999).

[123] Gor'kov, L. P. and Rashba, E. I. *Phys. Rev. Lett.* **87**(3), 037004 Jul (2001).

[124] Edelstein, V. M. *Phys. Rev. Lett.* **75**(10), 2004–2007 Sep (1995).

[125] Ngai, J. H., Segal, Y., Su, D., Zhu, Y., Walker, F. J., Ismail-Beigi, S., Le Hur, K., and Ahn, C. H. *Phys. Rev. B* **81**(24), 241307 Jun (2010).

[126] Reyren, N., Thiel, S., Caviglia, A. D., Kourkoutis, L. F., Hammerl, G., Richter, C., Schneider, C. W., Kopp, T., Ruetschi, A.-S., Jaccard, D., Gabay, M., Muller, D. A., Triscone, J.-M., and Mannhart, J. *Science* **317**(5842), 1196–1199 (2007).

[127] Breitschaft, M., Tinkl, V., Pavlenko, N., Paetel, S., Richter, C., Kirtley, J. R., Liao, Y. C., Hammerl, G., Eyert, V., Kopp, T., and Mannhart, J. *Phys. Rev. B* **81**(15), 153414 Apr (2010).

[128] Frederikse, H. P. R., Hosler, W. R., Thurber, W. R., Babiskin, J., and Siebenmann, P. G. *Phys. Rev.* **158**(3), 775–778 Jun (1967).

[129] Kozuka, Y., Kim, M., Bell, C., Kim, B. G., Hikita, Y., and Hwang, H. Y. *Nature* **462**(7272), 487–490 11 (2009).

[130] Ando, T., Fowler, A. B., and Stern, F. *Rev. Mod. Phys.* **54**(2), 437–672 Apr (1982).

[131] Bell, C., Harashima, S., Kozuka, Y., Kim, M., Kim, B. G., Hikita, Y., and Hwang, H. Y. *Phys. Rev. Lett.* **103**(22), 226802 Nov (2009).

[132] Son, J., Moetakef, P., Jalan, B., Bierwagen, O., Wright, N. J., Engel-Herbert, R., and Stemmer, S. *Nat Mater* **9**(6), 482–484 06 (2010).

[133] Caviglia, A. D., Gabay, M., Gariglio, S., Reyren, N., Cancellieri, C., and Triscone, J.-M. *Phys. Rev. Lett.* **104**(12), 126803 Mar (2010).

[134] Cen, C., Thiel, S., Hammerl, G., Schneider, C. W., Andersen, K. E., Hellberg, C. S., Mannhart, J., and Levy, J. *Nat Mater* **7**(4), 298–302 04 (2008).

[135] Cen, C., Thiel, S., Mannhart, J., and Levy, J. *Science* **323**(5917), 1026–1030 (2009).

[136] Langer, J. S. and Ambegaokar, V. *Phys. Rev.* **164**(2), 498–510 Dec (1967).

[137] McCumber, D. E. and Halperin, B. I. *Phys. Rev. B* **1**(3), 1054–1070 Feb (1970).

[138] Lau, C. N., Markovic, N., Bockrath, M., Bezryadin, A., and Tinkham, M. *Phys. Rev. Lett.* **87**(21), 217003 Nov (2001).